

1 A search for sparticles in zero lepton final states

2 Russell W. Smith

3 Submitted in partial fulfillment of the

4 requirements for the degree of

5 Doctor of Philosophy

6 in the Graduate School of Arts and Sciences

7 COLUMBIA UNIVERSITY

8 2016

9

© 2016

10

Russell W. Smith

11

All rights reserved

12

ABSTRACT

13

A search for sparticles in zero lepton final states

14

Russell W. Smith

15 TODO : Here's where your abstract will eventually go. The above text is all in the
16 center, but the abstract itself should be written as a regular paragraph on the page,
17 and it should not have indentation. Just replace this text.

Contents

19	Contents	i
20	1 Introduction	1
21	2 The Standard Model	5
22	2.1 Overview	5
23	2.2 Field Content	5
24	2.3 Deficiencies of the Standard Model	15
25	3 Supersymmetry	21
26	3.1 Supersymmetric theories : from space to superspace	21
27	3.2 Minimally Supersymmetric Standard Model	24
28	3.3 Phenomenology	30
29	3.4 How SUSY solves the problems with the SM	33
30	3.5 Conclusions	35
31	4 The Large Hadron Collider	37
32	4.1 Basics of Accelerator Physics	37
33	4.2 Accelerator Complex	39
34	4.3 Large Hadron Collider	41
35	4.4 Dataset Delivered by the LHC	43
36	5 The ATLAS detector	49

37	5.1	Magnets	50
38	5.2	Inner Detector	52
39	5.3	Calorimetry	56
40	5.4	Muon Spectrometer	61
41	5.5	Trigger System	66
42	6	Object Reconstruction	73
43	6.1	Primitive Object Reconstruction	73
44	6.2	Physics Object Reconstruction and Quality Identification	79
45	7	Recursive Jigsaw Reconstruction	105
46	7.1	Razor variables	105
47	7.2	Recursive Jigsaw Reconstruction	110
48	7.3	Variables used in the search for zero lepton SUSY	116
49	8	A search for supersymmetric particles in zero lepton final states with the Recursive Jigsaw Technique	123
50	8.1	Collision data and simulation samples	123
51	8.2	Event selection	127
52	8.3	Background estimation	133
54	9	Results	135
55	9.1	Statistical Analysis	135
56	9.2	Signal Region distributions	135
57	9.3	Pull Plots	135
58	9.4	Exclusion plots	135
59	Conclusion		137
60	9.5	New Section	137

61	Bibliography	139
62	Quantum Field Theory and Symmetries	151
63	Quantum Field Theory	151
64	Symmetries	152
65	Local symmetries	154

Acknowledgements

Dedication

Introduction

70 Particle physics is a remarkably successful field of scientific inquiry. The ability to
 71 precisely predict the properties of a exceedingly wide range of physical phenomena,
 72 such as the description of the cosmic microwave background [1, 2], the understanding
 73 of the anomalous magnetic dipole moment of the electron [3, 4], and the measurement
 74 of the number of weakly-interacting neutrino flavors [5] is truly amazing.

75 The theory that has allowed this range of predictions is the *Standard Model*
 76 of particle physics (SM). The Standard Model combines the electroweak theory of
 77 Glashow, Weinberg, and Salam [6–8] with the theory of the strong interactions, as
 78 first envisioned by Gell-Mann and Zweig [9, 10]. This quantum field theory (QFT)
 79 contains a tiny number of particles, whose interactions describe phenomena up to at
 80 least the TeV scale. These particles are manifestations of the fields of the Standard
 81 Model, after application of the Higgs Mechanism. The particle content of the SM
 82 consists only of the six quarks, the six leptons, the four gauge bosons, and the scalar
 83 Higgs boson.

84 Despite its impressive range of described phenomena, the Standard Model has
 85 some theoretical and experimental deficiencies. The SM contains 26 free parameters
 86 ¹. It would be more theoretically pleasing to understand these free parameters in
 87 terms of a more fundamental theory. The major theoretical concern of the Standard
 88 Model, as it pertains to this thesis, is the *hierarchy problem*[11–15]. The light mass

¹This is the Standard Model corrected to include neutrino masses. These parameters are the fermion masses (6 leptons, 6 quarks), CKM and PMNS mixing angles (8 angles, 2 CP-violating phases), W/Z/Higgs masses (3), the Higgs field expectation value, and the couplings of the strong, weak, and electromagnetic forces (3 α_{force}).

89 of the Higgs boson (125 GeV) should be quadratically dependent on the scale of UV
90 physics, due to the quantum corrections from high-energy physics processes. The
91 most perplexing experimental issue is the existence of *dark matter*, as demonstrated
92 by galactic rotation curves [16–22]. This data has shown that there exists additional
93 matter which has not yet been seen interacting with the particles of the Standard
94 Model. There is no particle in the SM which can act as a candidate for dark matter.

95 Both of these major issues, as well as numerous others, can be solved by the
96 introduction of *supersymmetry* (SUSY) [15, 23–35]. In supersymmetric theories, each
97 SM particles has a so-called *superpartner*, or sparticle partner, differing from given SM
98 particle by 1/2 in spin. These theories solve the hierarchy problem, since the quantum
99 corrections induced from the superpartners exactly cancel those induced by the SM
100 particles. In addition, these theories are usually constructed assuming *R*–parity,
101 which can be thought of as the “charge” of supersymmetry, with SM particles having
102 $R = 1$ and sparticles having $R = -1$. In collider experiments, since the incoming
103 SM particles have total $R = 1$, the resulting sparticles are produced in pairs. This
104 produces a rich phenomenology, which is characterized by significant hadronic activity
105 and large missing transverse energy (E_T^{miss}), which provide significant discrimination
106 against SM backgrounds [36].

107 Despite the power of searches for supersymmetry where E_T^{miss} is a primary
108 discriminating variable, there has been significant interest in the use of other variables
109 to discriminate against SM backgrounds. These include searches employing variables
110 such as αT , $M_{T,2}$, and the razor variables (M_R, R^2) [37–47]. In this thesis, we
111 will present the first search for supersymmetry using the novel Recursive Jigsaw
112 Reconstruction (RJR) technique. RJR can be considered the conceptual successor
113 of the razor variables. We impose a particular final state “decay tree” on an events,
114 which roughly corresponds to a simplified Feynmann diagram in decays containing
115 weakly-interacting particles. We account for the missing degrees of freedom associated

116 to the weakly-interacting particles by a series of simplifying assumptions, which allow
117 us to calculate our variables of interest at each step in the decay tree. This allows an
118 unprecedented understanding of the internal structure of the decay and the ability to
119 construct additional variables to reject Standard Model backgrounds.

120 This thesis details a search for the superpartners of the gluon and quarks, the
121 gluino and squarks, in final states with zero leptons, with 13.3 fb^{-1} of data using the
122 ATLAS detector. We organize the thesis as follows. The theoretical foundations of
123 the Standard Model and supersymmetry are described in Chapters 2 and 3. The
124 Large Hadron Collider and the ATLAS detector are presented in Chapters 4 and 5.
125 Chapter 5 provides a detailed description of Recursive Jigsaw Reconstruction and a
126 description of the variables used for the particular search presented in this thesis.
127 Chapter 6 presents the details of the analysis, including details of the dataset, object
128 reconstruction, and selections used. In Chapter 7, the final results are presented;
129 since there is no evidence of a supersymmetric signal in the analysis, we present the
130 final exclusion curves in simplified supersymmetric models.

133 2.1 Overview

134 A Standard Model is another name for a theory of the internal symmetry group
 135 $SU(3)_C \otimes SU(2)_L \otimes U(1)_Y$, with its associated set of parameters. *The Standard*
 136 Model refers specifically to a Standard Model with the proper parameters to describe
 137 the universe. The SM is the culmination of years of work in both theoretical
 138 and experimental particle physics. In this thesis, we take the view that theorists cite

139 construct a model with the field content and symmetries as inputs, and write down the
 140 most general Lagrangian consistent with those symmetries. Assuming this model is
 141 compatible with nature (in particular, the predictions of the model are consistent with
 142 previous experiments), experimentalists are responsible measuring the parameters of
 143 this model. This will be applicable for this chapter and the following one.

144 Additional theoretical background is in 9.5. The philosophy and notations are
 145 inspired by [48, 49].

146 2.2 Field Content

The Standard Model field content is

$$\begin{aligned} \text{Fermions} &: Q_L(3, 2)_{+1/3}, U_R(3, 1)_{+4/3}, D_R(3, 1)_{-2/3}, L_L(1, 2)_{-1}, E_R(1, 1)_{-2} \\ \text{Scalar (Higgs)} &: \phi(1, 2)_{+1} \\ \text{Vector Fields} &: G^\mu(8, 1)_0, W^\mu(1, 3)_0, B^\mu(1, 1)_0 \end{aligned} \tag{2.1}$$

147 where the $(A, B)_Y$ notation represents the irreducible representation under $SU(3)$
148 and $SU(2)$, with Y being the electroweak hypercharge. Each of these fermion fields
149 has an additional index, representing the three generation of fermions.

150 We observed that Q_L, U_R , and D_R are triplets under $SU(3)_C$; these are the *quark*
151 fields. The *color* group, $SU(3)_C$ is mediated by the *gluon* field $G^\mu(8, 1)_0$, which has
152 8 degrees of freedom. The fermion fields $L_L(1, 2)_{-1}$ and $E_R(1, 1)_{-2}$ are singlets under
153 $SU(3)_C$; we call them the *lepton* fields.

154 Next, we note the “left-handed” (“right-handed”) fermion fields, denoted by L (R)
155 subscript, The left-handed fields form doublets under $SU(2)_L$. These are mediated
156 by the three degrees of freedom of the “W” fields $W^\mu(1, 3)_0$. These fields only act
157 on the left-handed particles of the Standard Model. This is the reflection of the
158 “chirality” of the Standard Model; the left-handed and right-handed particles are
159 treated differently by the electroweak forces. The right-handed fields, U_R, D_R , and
160 E_R , are singlets under $SU(2)_L$.

161 The $U(1)_Y$ symmetry is associated to the $B^\mu(1, 1)_0$ boson with one degree of
162 freedom. The charge Y is known as the electroweak hypercharge.

163 To better understand the phenomenology of the Standard Model, let us investigate
164 each of the *sectors* of the Standard Model separately.

165 Electroweak sector

The electroweak sector refers to the $SU(2)_L \otimes U(1)_Y$ portion of the Standard
Model gauge group. Following our philosophy of writing all gauge-invariant and
renormalizable terms, the electroweak Lagrangian can be written as

$$\mathcal{L} = W_a^{\mu\nu} W_{\mu\nu}^a + B^{\mu\nu} B_{\mu\nu} + (D^\mu \phi)^\dagger D_\mu \phi - \mu^2 \phi^\dagger \phi - \lambda (\phi^\dagger \phi)^2. \quad (2.2)$$

where $W_a^{\mu\nu}$ are the three ($a = 1, 2, 3$) gauge bosons associated to the $SU(2)_L$ gauge
group, $B^{\mu\nu}$ is the one gauge boson of the $U(1)_Y$ gauge group, and ϕ is the complex

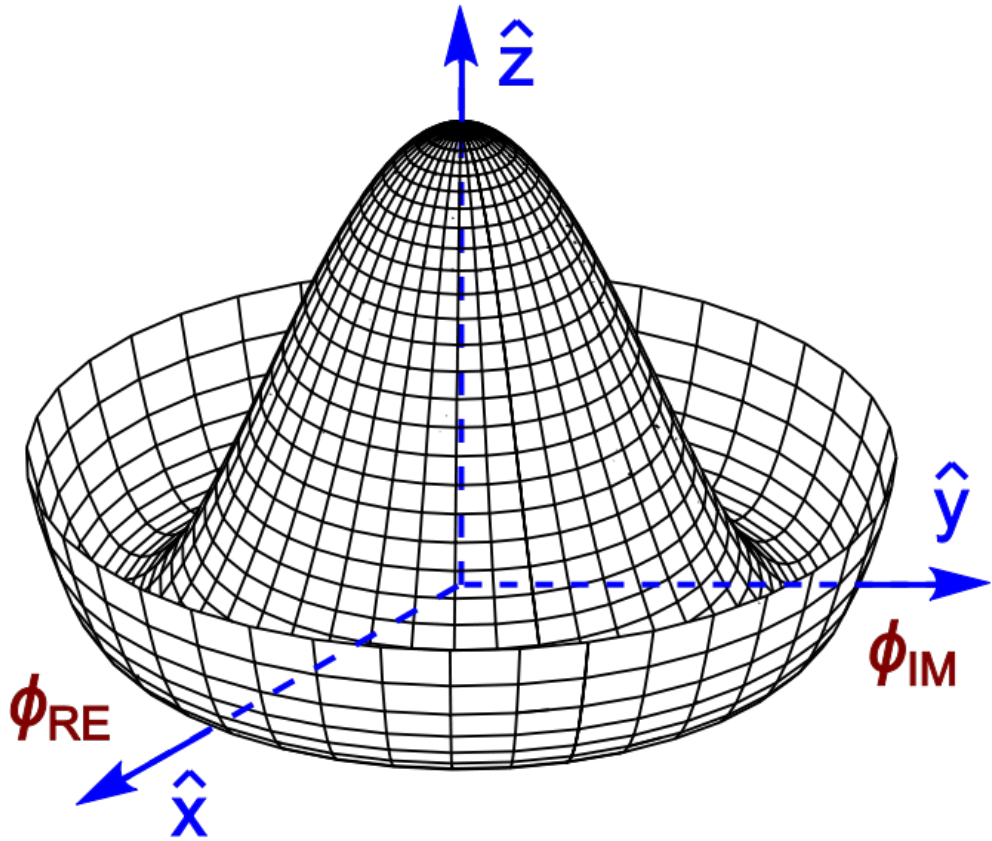


Figure 2.1: Sombrero potential

Higgs multiplet. The covariant derivative D^μ is given by

$$D^\mu = \partial^\mu + \frac{ig}{2}W_a^\mu\sigma_a + \frac{ig'}{2}B^\mu \quad (2.3)$$

where $i\sigma_a$ are the Pauli matrices times the imaginary constant, which are the generators for $SU(2)_L$, and g and g' are the $SU(2)_L$ and $U(1)_Y$ coupling constants, respectively. The field strength tensors $W_a^{\mu\nu}$ and $B^{\mu\nu}$ are given by the commutator of the covariant derivative associated to each field

$$B^{\mu\nu} = \partial^\mu B^\nu - \partial^\nu B^\mu \quad (2.4)$$

$$W_a^{\mu\nu} = \partial^\mu W_a^\nu - \partial^\nu W_a^\mu - g\epsilon_{abc}W_a^\mu W_b^\nu, \quad i = 1, 2, 3$$

167 The terms in the Lagrangian 2.2 proportional to μ^2 and λ make up the “Higgs
 168 potential” [50]. As normal (see Appendix 9.5), we restrict $\lambda > 0$ to guarantee our
 169 potential is bounded from below, and we also require $\mu^2 < 0$, which gives us the
 170 standard “sombrero” potential shown in 2.1.

This potential has infinitely many minima at $\langle \phi \rangle = \sqrt{2m/\lambda}$; the ground state is *spontaneously* broken by the choice of ground state, which induces a vacuum expectation value (VEV). Without loss of generality, we can choose the Higgs field ϕ to point in the real direction, and write the Higgs field ϕ in the following form :

$$\phi = \frac{1}{\sqrt{2}} \exp\left(\frac{i}{v} \sigma_a \theta_a\right) \begin{pmatrix} 0 \\ v + h(x) \end{pmatrix}. \quad (2.5)$$

We choose a gauge to rotate away the dependence on θ_a , such that we can write simply

$$\phi = \frac{1}{\sqrt{2}} \begin{pmatrix} 0 \\ v + h(x) \end{pmatrix}. \quad (2.6)$$

Now, we can see how the masses of the vector bosons are generated from the application of the Higgs mechanism. We plug Eq.2.6 back into the electroweak Lagrangian, and only showing the relevant mass terms in the vacuum state where $h(x) = 0$ see that (dropping the Lorentz indices) :

$$\begin{aligned} \mathcal{L}_M &= \frac{1}{8} \left| \begin{pmatrix} gW_3 + g'B & g(W_1 - iW_2) \\ g(W_1 + iW_2) & -gW_3 + g'B \end{pmatrix} \begin{pmatrix} 0 \\ v \end{pmatrix} \right|^2 \\ &= \frac{g^2 v^2}{8} \left[W_1^2 + W_2^2 + \left(\frac{g'}{g} B - W_3 \right)^2 \right] \end{aligned} \quad (2.7)$$

Defining the Weinberg angle $\tan(\theta_W) = g'/g$ and the following *physical* fields :

$$W^\pm = \frac{1}{\sqrt{2}} (W_1 \mp iW_2) \quad (2.8)$$

$$Z^0 = \cos \theta_W W_3 - \sin \theta_W B$$

$$A^0 = \sin \theta_W W_3 + \cos \theta_W B$$

we can write the piece of the Lagrangian associated to the vector boson masses as

$$\mathcal{L}_{MV} = \frac{1}{4}g^2 v^2 W^+ W^- + \frac{1}{8}(g^2 + g'^2)v^2 Z^0 Z^0. \quad (2.9)$$

and we have the following values of the masses for the vector bosons :

$$\begin{aligned} m_W^2 &= \frac{1}{4}v^2 g^2 \\ m_Z^2 &= \frac{1}{4}v^2(g^2 + g'^2) \\ m_A^2 &= 0 \end{aligned} \quad (2.10)$$

We thus see how the Higgs mechanism gives rise to the masses of the W^\pm and Z boson in the Standard Model; the mass of the photon is zero, as expected. The $SU(2)_L \otimes U(1)_Y$ symmetry of the initially massless $W_{1,2,3}$ and B fields is broken to the $U(1)_{EM}$. Of the four degrees of freedom in the complex Higgs doublet, three are “eaten” when we give mass to the W^\pm and Z_0 , while the other degree of freedom is the Higgs particle, as found in 2012 by the ATLAS and CMS collaborations [51, 52].

177 Quantum Chromodynamics

Quantum chromodynamics (or the theory of the *strong* force) characterizes the behavior of *colored* particles, collectively known as *partons*. The partons of the Standard Model are the (fermionic) quarks, and the (bosonic) gluons. The strong force is governed by $SU(3)_C$, an unbroken symmetry in the Standard Model, which implies the gluon remains massless. Defining the covariant derivative for QCD as

$$D^\mu = \partial^\mu + ig_s G_a^\mu L_a, a = 1, \dots, 8 \quad (2.11)$$

where L_a are the generators of $SU(3)_C$, and g_s is the coupling constant of the strong force. The QCD Lagrangian then is given by

$$\mathcal{L}_{QCD} = i\bar{\psi}_f D_\mu \gamma^\mu \psi_f - \frac{1}{4}G_{a,\mu\nu} G_a^{\mu\nu} \quad (2.12)$$

where the summation over f is for quarks *families*, and $G_a^{\mu\nu}$ is the gluon field strength tensor, given by

$$G_a^{\mu\nu} = \partial^\mu G_a^\nu - \partial^\nu G_a^\mu - g_s f^{abc} G_b^\mu G_c^\nu, a, b, c = 1, \dots, 8 \quad (2.13)$$

178 where f^{abc} are the structure constants of $SU(3)_C$, which are analogous to ϵ_{abc} for
 179 $SU(2)_L$. The kinetic term for the quarks is contained in the standard ∂_μ term, while
 180 the field strength term contains the interactions between the quarks and gluons, as
 181 well as the gluon self-interactions.

182 Written down in this simple form, the QCD Lagrangian does not seem much
 183 different from the QED Lagrangian, with the proper adjustments for the different
 184 group structures. The gluon is massless, like the photon, so one could naïvely expect
 185 an infinite range force, and it pays to understand why this is not the case. The
 186 reason for this fundamental difference is the gluon self-interactions arising in the
 187 field strength tensor term of the Lagrangian. This leads to the phenomena of *color*
 188 *confinement*, which describes how one only observes color-neutral particles alone in
 189 nature. In contrast to the electromagnetic force, particles which interact via the
 190 strong force experience a *greater* force as the distance between the particles increases.
 191 At long distances, the potential is given by $V(r) = -kr$. At some point, it is more
 192 energetically favorable to create additional partons out of the vacuum than continue
 193 pulling apart the existing partons, and the colored particles undergo *fragmentation*.
 194 This leads to *hadronization*. Bare quarks and gluons are actually observed as sprays
 195 of hadrons (primarily kaons and pions); these sprays are known as *jets*, which are
 196 what are observed by experiments.

197 It is important to recognize the importance of understanding these QCD inter-
 198 actions in high-energy hadron colliders such as the LHC. Since protons are hadrons,
 199 proton-proton collisions such as those produced by the LHC are primarily governed by
 200 the processes of QCD. In particular, by far the most frequent process observed in LHC
 201 experiments is dijet production from gluon-gluon interactions (see Fig.2.2). These

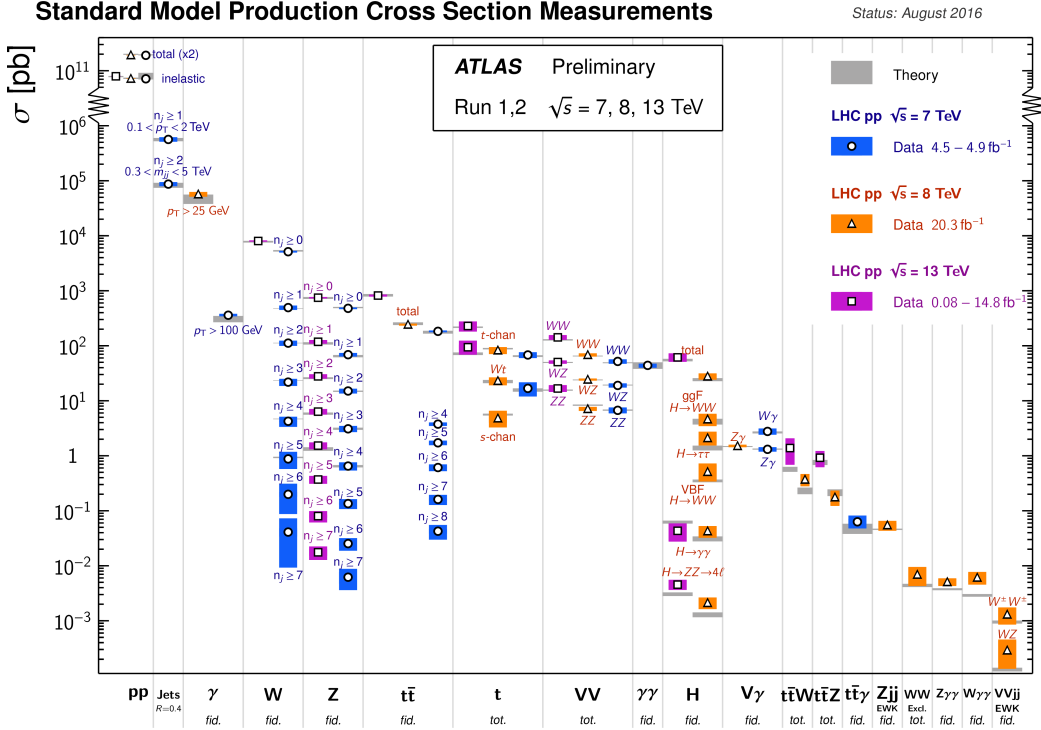


Figure 2.2: Cross-sections of various Standard Model processes

202 gluons that interact are part of the *sea* particles inside the proton; the simple $p = uud$
 203 model does not apply. The main *valence* uud quarks are constantly interacting via
 204 gluons, which can themselves radiate gluons or split into quarks, and so on. A more
 205 useful understanding is given by the colloquially-known *bag* model [53, 54], where the
 206 proton is seen as a “bag” of (in principle) infinitely many partons, each with energy
 207 $E < \sqrt{s} = 6.5$ TeV. One then collides this (proton) bag with another, and views the
 208 products of this very complicated collision, where calculations include many loops in
 209 nonperturbative QCD calculations.

210 Fortunately, we are generally saved by the QCD factorization theorems [55]. This
 211 allows one to understand the hard (i.e. short distance or high energy) $2 \rightarrow 2$ parton
 212 process using the tools of perturbative QCD, while making series of approximations
 213 known as a *parton shower* model to understand the additional corrections from
 214 nonperturbative QCD. We will discuss the reconstruction of jets by experiments in
 215 Ch.5.

216 **Fermions**

217 We will now look more closely at the fermions in the Standard Model [56].

218 As noted earlier in Sec.2.2, the fermions of the Standard Model can be first
 219 distinguished between those that interact via the strong force (quarks) and those
 220 which do not (leptons).

There are six leptons in the Standard Model, which can be placed into three
generations.

$$\begin{pmatrix} e \\ \nu_e \end{pmatrix}, \begin{pmatrix} \mu \\ \nu_\mu \end{pmatrix}, \begin{pmatrix} \tau \\ \nu_\tau \end{pmatrix} \quad (2.14)$$

221 There is the electron (e), muon (μ), and tau (τ), each of which has an associated
 222 neutrino (ν_e, ν_μ, ν_τ). Each of the so-called charged (“electron-like”) leptons has
 223 electromagnetic charge -1 , while the neutrinos all have $q_{EM} = 0$.

224 Often in an experimental context, lepton is used to denote the stable electron
 225 and metastable muon, due to their striking experimental signatures. Taus are often
 226 treated separately, due to their much shorter lifetime of $\tau_\tau \sim 10^{-13}s$; these decay
 227 through hadrons or the other leptons, so often physics analyses at the LHC treat
 228 them as jets or leptons, as will be done in this thesis.

229 As the neutrinos are electrically neutral, nearly massless, and only interact via the
 230 weak force, it is quite difficult to observe them directly. Since LHC experiments rely
 231 overwhelmingly on electromagnetic interactions to observe particles, the presence of
 232 neutrinos is not observed directly. Neutrinos are instead observed by the conservation
 233 of four-momentum in the plane transverse to the proton-proton collisions, known as
 234 *missing transverse energy*.

There are six quarks in the Standard Model : up, down, charm, strange, top, and
 bottom. Quarks are similar organized into three generations :

$$\begin{pmatrix} u \\ d \end{pmatrix}, \begin{pmatrix} c \\ s \end{pmatrix}, \begin{pmatrix} t \\ b \end{pmatrix} \quad (2.15)$$

235 where we speak of “up-like” quarks and “down-like” quarks.

236 Each up-like quark has charge $q_{up} = 2/3$, while the down-like quarks have $q_{down} =$
237 $-1/3$. At the high energies of the LHC, one often makes the distinction between
238 the light quarks (u, d, c, s), the bottom quark, and top quark. In general, due to
239 the hadronization process described above, the light quarks, with masses $m_q < \sim$
240 1.5GeV are indistinguishable by LHC experiments. Their hadronic decay products
241 generally have long lifetimes and they are reconstructed as jets.¹. The bottom quark
242 hadronizes primarily through the B -mesons, which generally travels a short distance
243 before decaying to other hadrons. This allows one to distinguish decays via b -quarks
244 from other jets; this procedure is known as *b-tagging* and will be discussed more in
245 Ch.5. Due to its large mass, the top quark decays before it can hadronize; there
246 are no bound states associated to the top quark. The top is of particular interest at
247 the LHC; it has a striking signature through its most common decay mode $t \rightarrow Wb$.
248 Decays via tops, especially $t\bar{t}$ are frequently an important signal decay mode, or an
249 important background process.

250 **Interactions in the Standard Model**

251 We briefly overview the entirety of the fundamental interactions of the Standard
252 Model; these can also be found in 2.3.

253 The electromagnetic force, mediated by the photon, interacts with via a three-
254 point coupling all charged particles in the Standard Model. The photon thus interacts
255 with all the quarks, the charged leptons, and the charged W^\pm bosons.

256 The weak force is mediated by three particles : the W^\pm and the Z^0 . The Z^0 can
257 interact with all fermions via a three-point coupling. A real Z_0 can thus decay to
258 a fermion-antifermion pair of all SM fermions except the top quark, due to its large

¹In some contexts, charm quarks are also treated as a separate category, although it is quite difficult to distinguish charm quarks from the other light quarks.

Standard Model Interactions (Forces Mediated by Gauge Bosons)

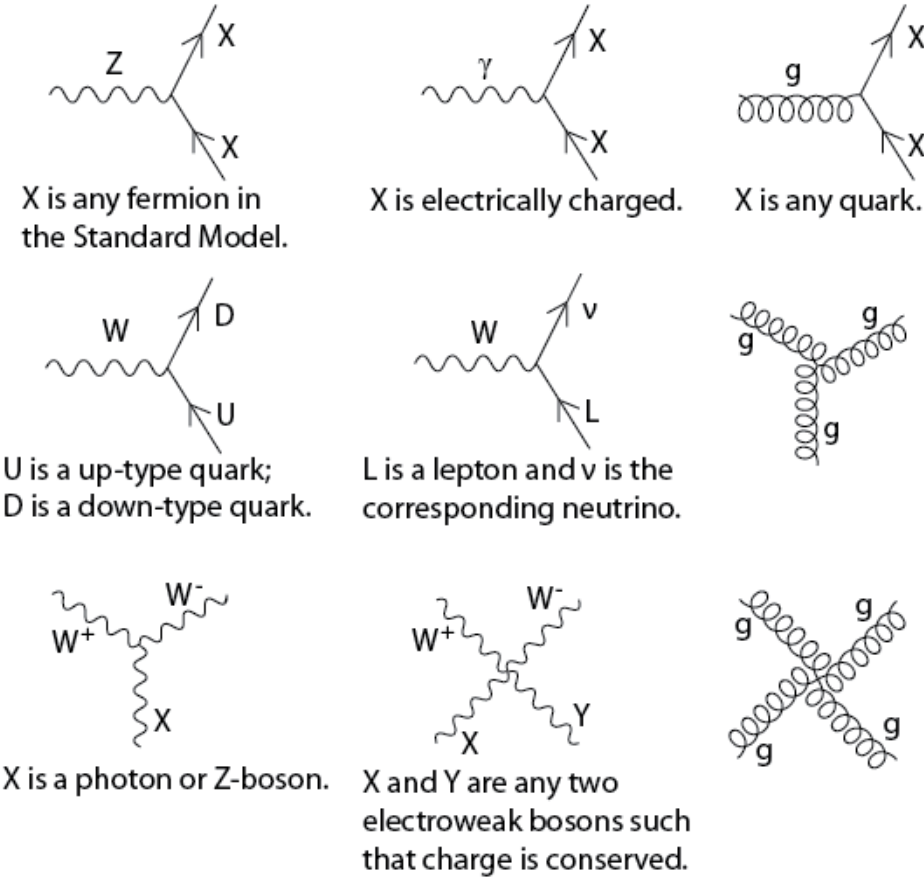


Figure 2.3: The interactions of the Standard Model

mass. The W^\pm has two important three-point interactions with fermions. First, the W^\pm can interact with an up-like quark and a down-like quark; an important example in LHC experiments is $t \rightarrow Wb$. The coupling constants for these interactions are encoded in the unitary matrix known as the Cabibbo–Kobayashi–Maskawa (CKM) matrix [57, 58], and are generally known as flavor-changing interactions. Secondly, the W^\pm interacts with a charged lepton and its corresponding neutrino. In this case, the unitary matrix that corresponds to CKM matrix for quarks is the identity matrix, which forbids (fundamental) vertices such as $\mu \rightarrow We$. For leptons, instead this is a two-step process : $\mu \rightarrow \nu_m u W \rightarrow \nu_m u \bar{\nu}_e e$. Finally, there are the self-interactions

268 of the weak gauge bosons. There is a three-point and four-point interaction; all
269 combinations are allowed which conserve electric charge.

270 The strong force is mediated by the gluon, which as discussed above also carries
271 the strong color charge. There is the fundamental three-point interaction, where a
272 quark radiates a gluon. Additionally, there are the three-point and four-point gluon-
273 only interactions.

274 2.3 Deficiencies of the Standard Model

275 At this point, it is quite easy to simply rest on our laurels. This relatively simple
276 theory is capable of explaining a very wide range of phenomena, which ultimately
277 break down only to combinations of nine diagrams shown in Fig.2.3. Unfortunately,
278 there are some unexplained problems with the Standard Model. We cannot go
279 through all of the potential issues in this thesis, but we will motivate the primary
280 issues which naturally lead one to *supersymmetry*, as we will see in Ch.3.

The Standard Model has many free parameters; see Table 2.1 In general, we prefer models with less free parameters. A great example of this fact, and the primary experimental evidence for EWSB, is the relationship between the couplings of the weak force and the masses of the gauge bosons of the weak force :

$$\rho \equiv \frac{m_W^2}{m_Z^2 \cos^2 \theta_W} \stackrel{?}{=} 1 \quad (2.16)$$

281 where ? indicates that this is a testable prediction of the Standard Model (in
282 particular, that the gauge bosons gain mass through EWSB). This relationship has
283 been measured within experimental and theoretical predictions. We would like to
284 produce additional such relationships, which would exist if the Standard Model is a
285 low-energy approximation of some other theory.

286 An additional issue is the lack of *gauge coupling unification*. The couplings of
287 any quantum field theory “run” as a function of the distance scales (or inversely,

m_e	Electron mass	511 keV
m_μ	Muon mass	105.7 MeV
m_τ	Tau mass	1.78 GeV
m_u	Up quark mass	1.9 MeV ($m_{\bar{MS}} = 2\text{GeV}$)
m_d	Down quark mass	4.4 MeV ($m_{\bar{MS}} = 2\text{GeV}$)
m_s	Strange quark mass	87 MeV ($m_{\bar{MS}} = 2\text{GeV}$)
m_c	Charm quark mass	1.32 GeV ($m_{\bar{MS}} = m_c$)
m_b	Bottom quark mass	4.24 GeV ($m_{\bar{MS}} = m_b$)
m_t	Top quark mass	172.7 GeV (on-shell renormalization)
θ_{12} CKM	12-mixing angle	13.1°
θ_{23} CKM	23-mixing angle	2.4°
θ_{13} CKM	13-mixing angle	0.2°
δ CKM	CP-violating Phase	0.995
g'	U(1) gauge coupling	0.357 ($m_{\bar{MS}} = m_Z$)
g	SU(2) gauge coupling	0.652 ($m_{\bar{MS}} = m_Z$)
g_s	SU(3) gauge coupling	1.221 ($m_{\bar{MS}} = m_Z$)
θ_{QCD}	QCD vacuum angle	~0
VEV	Higgs vacuum expectation value	246 GeV
m_H	Higgs mass	125 GeV

Table 2.1: Parameters of the Standard Model. For values dependent on the renormalization scheme, we use a combination of the on-shell normalization scheme [59–62] and modified minimal subtraction scheme with $m_{\bar{MS}}$ as indicated in the table[63]

288 energy scales) of the theory. The idea is closely related to the unification of the
 289 electromagnetic and weak forces at the so-called *electroweak scale* of $O(100 \text{ GeV})$.
 290 One would hope this behavior was repeated between the electroweak forces and the
 291 strong force at some suitable energy scale. The Standard Model does automatically
 292 not exhibit this behavior, as we can see in Fig.2.4.

The most significant problem with the Standard Model is the *hierarchy problem*. In its most straightforward incarnation, the Higgs scalar field is subject to quantum corrections through loop diagrams, as shown in Fig.2.5. For demonstration, we use the contributions from the top quark, since the top quark has the largest Higgs Yukawa coupling due to its large mass. In general, we should expect these corrections to quadratically depend on the scale of the ultraviolet physics, Λ . Briefly assume there is no new physics before the Planck scale of gravity, $\Lambda_{\text{Planck}} = 10^{19} \text{ GeV}$. In this

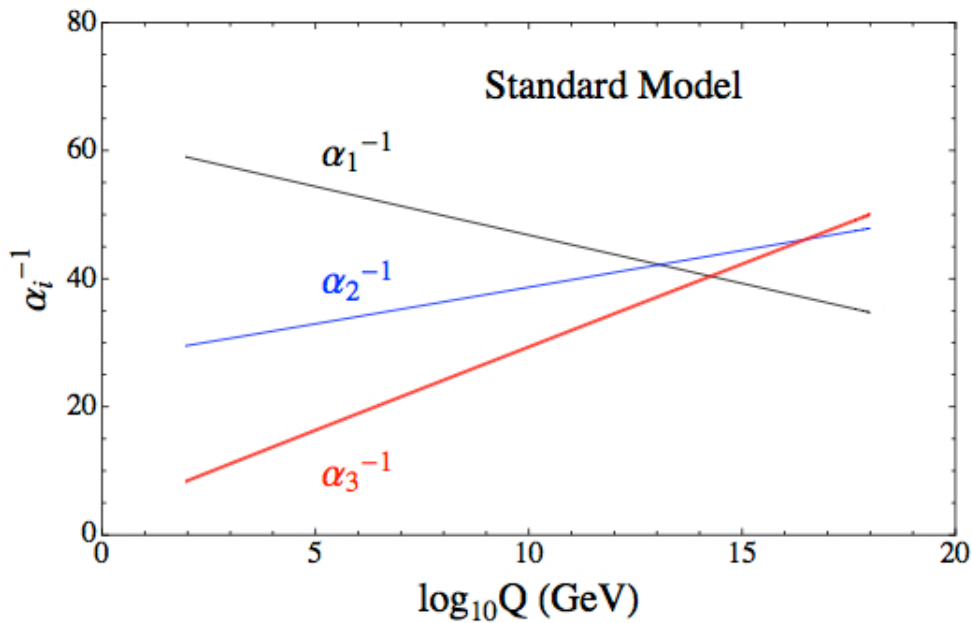


Figure 2.4: The running of Standard Model gauge couplings. The Standard Model couplings do not unify at high energies, which indicates it cannot completely describe nature through the Planck scale.

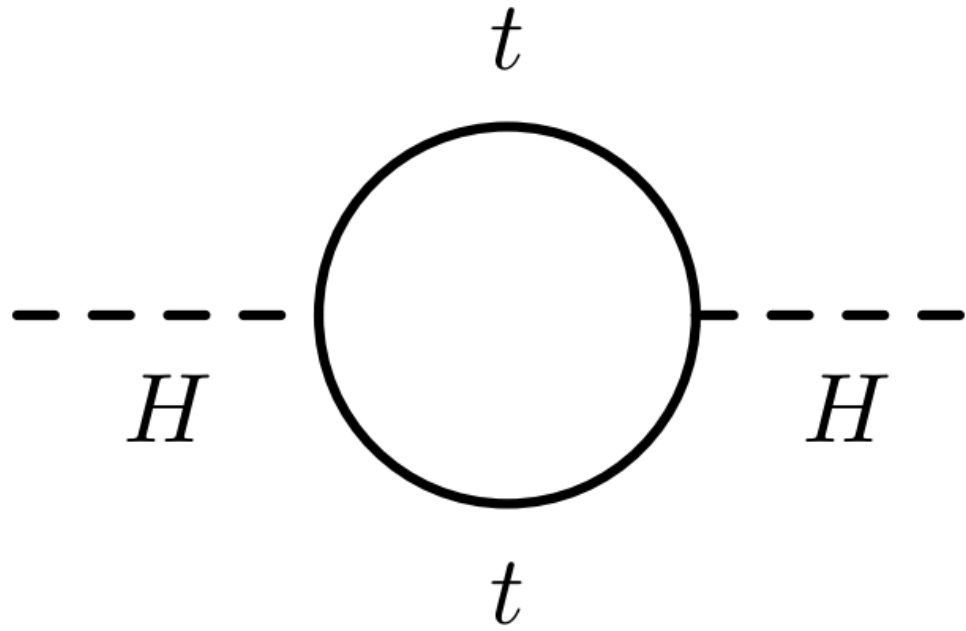


Figure 2.5: The dominant quantum loop correction to the Higgs mass in the Standard Model.

case, we expect the corrections to the Higgs mass like

$$\delta m_H^2 \approx \left(\frac{m_t}{8\pi^2 \langle \phi \rangle_{VEV}} \right)^2 \Lambda_{Planck}^2. \quad (2.17)$$

293 To achieve the miraculous cancellation required to get the observed Higgs mass of
294 125 GeV, one needs to then set the bare Higgs mass m_0 , our input to the Standard
295 Model Lagrangian, itself to a *precise* value $\sim 10^{19}$ GeV. This extraordinary level of
296 parameter finetuning is quite undesirable, and within the framework of the Standard
297 Model, there is little that can be done to alleviate this issue.

298 An additional concern, of a different nature, is the lack of a *dark matter* candidate
299 in the Standard Model. Dark matter was discovered by observing galactic rotation
300 curves, which showed that much of the matter that interacted gravitationally was
301 invisible to our (electromagnetic) telescopes [16–22]. The postulation of the existence
302 of dark matter, which interacts at least through gravity, allows one to understand
303 these galactic rotation curves. Unfortunately, no particle in the Standard Model could
304 possibly be the dark matter particle. The only candidate truly worth another look is
305 the neutrino, but it has been shown that the neutrino content of the universe is simply
306 too small to explain the galactic rotation curves [22, 64]. The experimental evidence
307 from the galactic rotations curves thus show there *must* be additional physics beyond
308 the Standard Model, which is yet to be understood.

309 In the next chapter, we will see how these problems can be alleviated by the theory
310 of supersymmetry.

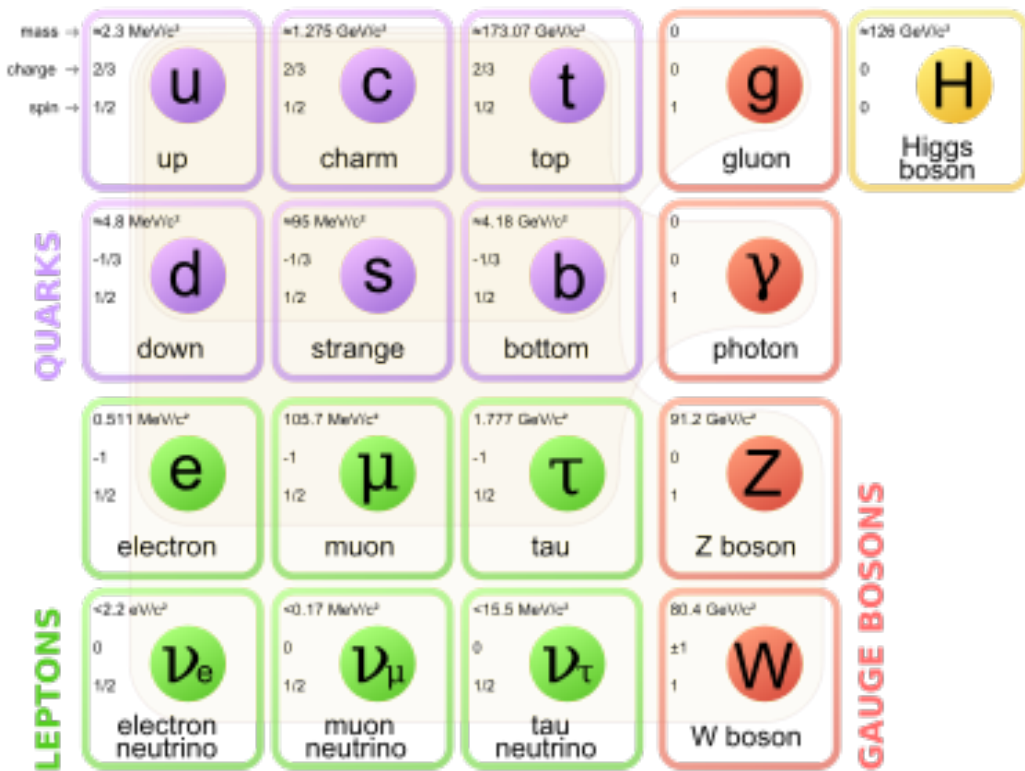


Figure 2.6: Particles of the Standard Model

311

Chapter 3

312

Supersymmetry

313 This chapter will introduce supersymmetry (SUSY) [15, 23–35]. We will begin by
314 introducing the concept of a *superspace*, and discuss some general ingredients of
315 supersymmetric theories. This will include a discussion of how the problems with the
316 Standard Model described in Ch.2 are naturally fixed by these theories.

317 The next step is to discuss the particle content of the *Minimally Supersymmetric*
318 *Standard Model* (MSSM). As its name implies, this theory contains the minimal
319 additional particle content to make Standard Model supersymmetric. We then discuss
320 the important phenomenological consequences of this theory, especially as it would
321 be observed in experiments at the LHC.

322 **3.1 Supersymmetric theories : from space to
323 superspace**

324 **Coleman-Mandula “no-go” theorem**

325 We begin the theoretical motivation for supersymmetry by citing the “no-go” theorem
326 of Coleman and Mandula [65]. This theorem forbids *spin-charge unification*; it
327 states that all quantum field theories which contain nontrivial interactions must be
328 a direct product of the Poincarégroup of Lorentz symmetries, the internal product
329 from of gauge symmetries, and the discrete symmetries of parity, charge conjugation,
330 and time reversal. The assumptions which go into building the Coleman-Mandula

theorem are quite restrictive, but there is one unique way out, which has become known as *supersymmetry* [26, 66]. In particular, we must introduce a *spinorial* group generator Q . Alternatively, and equivalently, this can be viewed as the addition of anti-commuting coordinates; space plus these new anti-commuting coordinates is then called *superspace* [67]. We will not investiage this view in detail, but it is also a quite intuitive and beautiful way to construct supersymmetry[15].

337 Supersymmetry transformations

A *supersymmetric* transformation Q transforms a bosonic state into a fermionic state, and vice versa :

$$Q |\text{Fermion}\rangle = |\text{Boson}\rangle \quad (3.1)$$

$$Q |\text{Boson}\rangle = |\text{Fermion}\rangle \quad (3.2)$$

To ensure this relation holds, Q must be an anticommuting spinor. Additionally, since spinors are inherently complex, Q^\dagger must also be a generator of the supersymmetry transformation. Since Q and Q^\dagger are spinor objects (with $s = 1/2$), we can see that supersymmetry must be a spacetime symmetry. The Haag-Lopuszanski-Sohnius extension [66] of the Coleman-Mandula theorem [65] is quite restrictive about the forms of such a symmetry. Here, we simply write the (anti-) commutation relations [15] :

$$Q_\alpha, Q_{\dot{\alpha}}^\dagger = -2\sigma_{\alpha\dot{\alpha}\mu} P_\mu \quad (3.3)$$

$$Q_\alpha, Q_{\dot{\beta}} = Q_{\dot{\alpha}}^\dagger, Q_{\dot{\beta}}^\dagger = 0 \quad (3.4)$$

$$[P^\mu, Q_\alpha] = [P^\mu, Q_{\dot{\alpha}}^\dagger] = 0 \quad (3.5)$$

340 **Supermultiplets**

341 In a supersymmetric theory, we organize single-particle states into irreducible
342 representations of the supersymmetric algebra which are known as *supermultiplets*.
343 Each supermultiplet contains a fermion state $|F\rangle$ and a boson state $|B\rangle$; these two
344 states are the known as *superpartners*. These are related by some combination of
345 Q and Q^\dagger , up to a spacetime transformation. Q and Q^\dagger commute with the mass-
346 squared operator $-P^2$ and the operators corresponding to the gauge transformations
347 [15]; in particular, the gauge interactions of the Standard Model. In an unbroken
348 supersymmetric theory, this means the states $|F\rangle$ and $|B\rangle$ have exactly the same mass,
349 electromagnetic charge, electroweak isospin, and color charges. One can also prove
350 [15] that each supermultiplet contains the exact same number of bosonic (n_B) and
351 fermion (n_F) degrees of freedom. We now explore the possible types of supermultiples
352 one can find in a renormalizable supersymmetric theory.

353 Since each supermultiplet must contain a fermion state, the simplest type of
354 supermultiplet contains a single Weyl fermion state ($n_F = 2$) which is paired with
355 $n_B = 2$ scalar bosonic degrees of freedom. This is most conveniently constructed as
356 single complex scalar field. We call this construction a *scalar supermultiplet* or *chiral*
357 *supermultiplet*. The second name is indicative; only chiral supermultiplets can contain
358 fermions whose right-handed and left-handed components transform differently under
359 the gauge interactions (as of course happens in the Standard Model).

360 The second type of supermultiplet we construct is known as a *gauge* supermul-
361 tiplet. We take a spin-1 gauge boson (which must be massless due to the gauge
362 symmetry, so $n_B = 2$) and pair this with a single massless Weyl spinor¹. The gauge
363 bosons transform as the adjoint representation of the their respective gauge groups;
364 their fermionic partners, which are known as gauginos, must also. In particular,
365 the left-handed and right-handed components of the gaugino fermions have the same

¹Choosing an $s = 3/2$ massless fermion leads to nonrenormalizable interactions.

366 gauge transformation properties.

367 Excluding gravity, this is the entire list of supermultiplets which can participate
368 in renormalizable interactions in what is known as $N = 1$ supersymmetry. This
369 means there is only one copy of the supersymmetry generators Q and Q^\dagger . This is
370 essentially the only “easy” phenomenological choice, since it is the only choice in four
371 dimensions which allows for the chiral fermions and parity violations built into the
372 Standard Model, and we will not look further into $N > 1$ supersymmetry in this thesis.

373 The primary goal, after understanding the possible structures of the multiplets
374 above, is to fit the Standard Model particles into a multiplet, and therefore make
375 predictions about their supersymmetric partners. We explore this in the next section.

376 **3.2 Minimally Supersymmetric Standard Model**

377 To construct what is known as the MSSM [15, 68–71], we need a few ingredients and
378 assumptions. First, we match the Standard Model particles with their corresponding
379 superpartners of the MSSM. We will also introduce the naming of the superpartners
380 (also known as *sparticles*). We discuss a very common additional restraint imposed on
381 the MSSM, known as *R*–parity. We also discuss the concept of soft supersymmetry
382 breaking and how it manifests itself in the MSSM.

383 **Chiral supermultiplets**

384 The first thing we deduce is directly from Sec.???. The bosonic superpartners
385 associated to the quarks and leptons *must* be spin 0, since the quarks and leptons must
386 be arranged in a chiral supermultiplet. This is essentially the note above, since the
387 chiral supermultiplet is the only one which can distinguish between the left-handed
388 and right-handed components of the Standard Model particles. The superpartners of
389 the quarks and leptons are known as *squarks* and *sleptons*, or *sfermions* in aggregate.

390 (for “scalar quarks”, “scalar leptons”, and “scalar fermion”²). The “s-” prefix
 391 can also be added to the individual quarks i.e. *selectron*, *sneutrino*, and *stop*. The
 392 notation is to add a \sim over the corresponding Standard Model particle i.e. \tilde{e} , the
 393 selectron is the superpartner of the electron. The two-component Weyl spinors of the
 394 Standard Model must each have their own (complex scalar) partner i.e. e_L, e_R have
 395 two distinct partners : \tilde{e}_L, \tilde{e}_R . As noted above, the gauge interactions of any of the
 396 sfermions are identical to those of their Standard Model partners.

Due to the scalar nature of the Higgs, it must obviously lie in a chiral supermultiplet. To avoid gauge anomalies and ensure the correct Yukawa couplings to the quarks and leptons[15], we must add additional Higgs bosons to any supersymmetric theory. In the MSSM, we have two chiral supermultiplets. The SM (SUSY) parts of the multiplets are denoted $H_u(\tilde{H}_u)$ and $H_d(\tilde{H}_d)$. Writing out H_u and H_d explicitly:

$$H_u = \begin{pmatrix} H_u^+ \\ H_u^0 \end{pmatrix} \quad (3.6)$$

$$H_d = \begin{pmatrix} H_d^0 \\ H_d^- \end{pmatrix} \quad (3.7)$$

(3.8)

397 we see that H_u looks very similar to the SM Higgs with $Y = 1$, and H_d is symmetric
 398 to this with $+ \rightarrow -$, with $Y = -1$. The SM Higgs boson, h_0 , is a linear superposition
 399 of the neutral components of these two doublets. The SUSY parts of the Higgs
 400 multiplets, \tilde{H}_u and \tilde{H}_d , are each left-handed Weyl spinors. For generic spin-1/2
 401 sparticles, we add the “-ino” suffix. We then call the partners of the two Higgs
 402 collectively the *Higgsinos*.

²The last one should probably have bigger scare quotes.

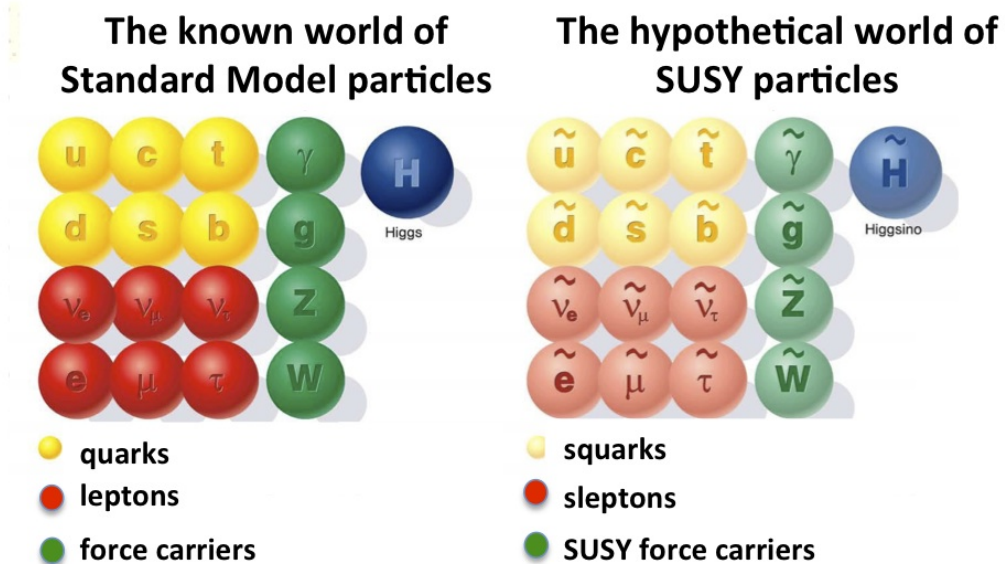


Figure 3.1: Particles of the MSSM

403 Gauge supermultiplets

404 The superpartners of the gauge bosons must all be in gauge supermultiplets since
 405 they contain a spin-1 particle. Collectively, we refer to the superpartners of the
 406 gauge bosons as the gauginos.

407 The first gauge supermultiplet contains the gluon, and its superpartner, which is
 408 known as the *gluino*, denoted \tilde{g} . The gluon is of course the SM mediator of $SU(3)_C$;
 409 the gluino is also a colored particle, subject to $SU(3)_C$. From the SM before EWSB,
 410 we have the four gauge bosons of the electroweak symmetry group $SU(2)_L \otimes U(1)_Y$:
 411 $W^{1,2,3}$ and B^0 . The superpartners of these particles are thus the *winos* $W^{\tilde{1},\tilde{2},\tilde{3}}$ and
 412 *bino* \tilde{B}^0 , where each is placed in another gauge supermultiplet with its corresponding
 413 SM particle. After EWSB, without breaking supersymmetry, we would also have the
 414 zino \tilde{Z}^0 and photino $\tilde{\gamma}$.

415 The entire particle content of the MSSM can be seen in Fig.3.1.

416 At this point, it's important to take a step back. Where are these particles?
 417 As stated above, supersymmetric theories require that the masses and all quantum



Figure 3.2: This Feynmann diagram shows how proton decay is induced in the MSSM, if one does not impose R -parity.

418 numbers of the SM particle and its corresponding sparticle are the same. Of course,
 419 we have not observed a selectron, squark, or wino. The answer, as it often is, is that
 420 supersymmetry is *broken* by the vacuum state of nature [15].

421 **R -parity**

This section is a quick aside to the general story. R – parity refers to an additional discrete symmetry which is often imposed on supersymmetric models. For a given particle state, we define

$$R = (-1)^{3(B-L)+2s} \quad (3.9)$$

422 where B, L is the baryon (lepton) number and s is the spin. The imposition of
 423 this symmetry forbids certain terms from the MSSM Lagrangian that would violate
 424 baryon and/or lepton number. This is required in order to prevent proton decay, as
 425 shown in Fig.3.2³. .

426 In supersymmetric models, this is a \mathbb{Z}_2 symmetry, where SM particles have $R = 1$
 427 and sparticles have $R = -1$. We will take R – parity as part of the definition of
 428 the MSSM. We will discuss later the *drastic* consequences of this symmetry on SUSY
 429 phenomenology

³Proton decay can actually be prevented by allowing only one of the four potential R-parity violating terms to survive.

430 **Soft supersymmetry breaking**

The fundamental idea of *soft* supersymmetry breaking[15, 34, 35, 72, 73] is that we would like to break supersymmetry without reintroducing the quadratic divergences we discussed at the end of Chapter 2. We write the Lagrangian in a form :

$$\mathcal{L}_{\text{MSSM}} = \mathcal{L}_{\text{SUSY}} + \mathcal{L}_{\text{soft}} \quad (3.10)$$

431 In this sense, the symmetry breaking is “soft”, since we have separated out the
 432 completely symmetric terms from those soft terms which will not allow the quadratic
 433 divergences to the Higgs mass.

434 The explicitly allowed terms in the soft-breaking Lagrangian are [35].

- 435 • Mass terms for the scalar components of the chiral supermultipletss
 436 • Mass terms for the Weyl spinor components of the gauge supermultipletss
 437 • Trilinear couplings of scalar components of chiral supermultiplets

In particular, using the field content described above for the MSSM, the softly-broken portion of the MSSM Lagrangian can be written

$$\mathcal{L}_{\text{soft}} = -\frac{1}{2} \left(M_3 \tilde{g} \tilde{g} + M_2 \tilde{W} \tilde{W} + M_1 \tilde{B} \tilde{B} + c.c. \right) \quad (3.11)$$

$$- \left(\tilde{u} a_u \tilde{Q} H_u - \tilde{d} a_d \tilde{Q} H_d - \tilde{e} a_e \tilde{L} H_d + c.c. \right) \quad (3.12)$$

$$- \tilde{Q}^\dagger m_Q^2 \tilde{Q} - \tilde{L}^\dagger m_L^2 \tilde{L} - \tilde{u} m_u^2 \tilde{u}^\dagger - \tilde{d} m_d^2 \tilde{d}^\dagger - \tilde{e} m_e^2 \tilde{e}^\dagger \quad (3.13)$$

$$- m_{H_u}^2 H_u^* H_u - m_{H_d}^2 H_d^* H_d - (b H_u H_d + cc). \quad (3.14)$$

438 where we have introduced the following notations :

439 1. M_3, M_2, M_1 are the gluino, wino, and bino masses.

440 2. a_u, a_d, a_e are complex 3×3 matrices in family space.

441 3. $m_Q^2, m_u^2, m_d^2, m_L^2, m_e^2$ are hermitian 3×3 matrices in family space.

442 4. $m_{H_u}^2, m_{H_d}^2, b$ are the SUSY-breaking contributions to the Higgs potential.

443 We have written matrix terms without any sort of additional notational decoration
 444 to indicate their matrix nature, and we now show why. The first term 1 are
 445 straightforward; these are just the straightforward mass terms for these fields. There
 446 are strong constraints on the off-diagonal terms for the matrices of 2 [74, 75]; for
 447 simplicity, we will assume that each $a_i, i = u, d, e$ is proportional to the Yukawa
 448 coupling matrix : $a_i = A_{i0}y_i$. The matrices in ?? can be similarly constrained by
 449 experiments [68, 75–82] Finally, we assume that the elements 4 contributing to the
 450 Higgs potential as well as all of the 1 terms must be real, which limits the possible
 451 CP-violating interactions to those of the Standard Model. We thus only consider
 452 flavor-blind, CP-conserving interactions within the MSSM.

The important mixing for mass and gauge interaction eigenstates in the MSSM occurs within electroweak sector, in a process akin to EWSB in the Standard Model. The neutral portions of the Higgsinos doublets and the neutral gauginos $(\tilde{H}_u^0, \tilde{H}_d^0, \tilde{B}^0, \tilde{W}^0)$ of the gauge interaction basis mix to form what are known as the *neutralinos* of mass basis :

$$M_{\tilde{\chi}} = \begin{pmatrix} M_1 & 0 & -c_\beta s_W m_Z & s_\beta s_W m_Z \\ 0 & M_2 & c_\beta c_W m_Z & -s_\beta c_W m_Z \\ -c_\beta s_W m_Z & c_\beta c_W m_Z & 0 & -\mu \\ s_\beta s_W m_Z & -s_\beta c_W m_Z & -\mu & 0 \end{pmatrix} \quad (3.15)$$

453 where $s(c)$ are the sine and cosine of angles related to EWSB, which introduced
 454 masses to the gauginos and higgsinos. Diagonalization of this matrix gives the four
 455 neutralino mass states, listed without loss of generality in order of increasing mass :
 456 $\tilde{\chi}_{1,2,3,4}^0$.

457 The neutralinos, especially the lightest neutralino $\tilde{\chi}_1^0$, are important ingredients
 458 in SUSY phenomenology.

459 The same process can be done for the electrically charged gauginos with
460 the charged portions of the Higgsino doublets along with the charged winos
461 ($\tilde{H}_u^+, \tilde{H}_d^+, \tilde{W}^+, \tilde{W}^-$). This leads to the *charginos*, again in order of increasing mass
462 : $\tilde{\chi}_{1,2}^\pm$.

463

3.3 Phenomenology

464 We are finally at the point where we can discuss the phenomenology of the MSSM,
465 in particular as it manifests itself at the energy scales of the LHC.

466 As noted above in Sec.3.2, the assumption of *R*–parity has important conse-
467 quences for MSSM phenomenology. The SM particles have $R = 1$, while the sparticles
468 all have $R = -1$. Simply, this is the “charge” of supersymmetry. Since the particles of
469 LHC collisions (pp) have total incoming $R = 1$, we must expect that all sparticles will
470 be produced in *pairs*. An additional consequence of this symmetry is the fact that the
471 lightest supersymmetric particle (LSP) is *stable*. Off each branch of the Feynmann
472 diagram shown in Fig., we have $R = -1$, and this can only decay to another sparticle
473 and a SM particle. Once we reach the lightest sparticle in the decay, it is absolutely
474 stable. This leads to the common signature E_T^{miss} for a generic SUSY signal.

475 For this thesis, we will be presenting an inclusive search for squarks and gluinos
476 with zero leptons in the final state. This is a very interesting decay channel⁴, due
477 to the high cross-sections of $\tilde{g}\tilde{g}$ and $\tilde{q}\tilde{q}$ decays, as can be seen in Fig.?? [83]. This
478 is a direct consequence of the fact that these are the colored particles of the MSSM.
479 Since the sparticles interact with the gauge groups of the SM in the same way as their
480 SM partners, the colored sparticles, the squarks and gluinos, are produced and decay
481 as governed by the color group $SU(3)_C$ with the strong coupling g_S . The digluino
482 production is particularly copious, due to color factor corresponding to the color octet

⁴Prior to Run1, probably the most *most* interesting SUSY decay channel.

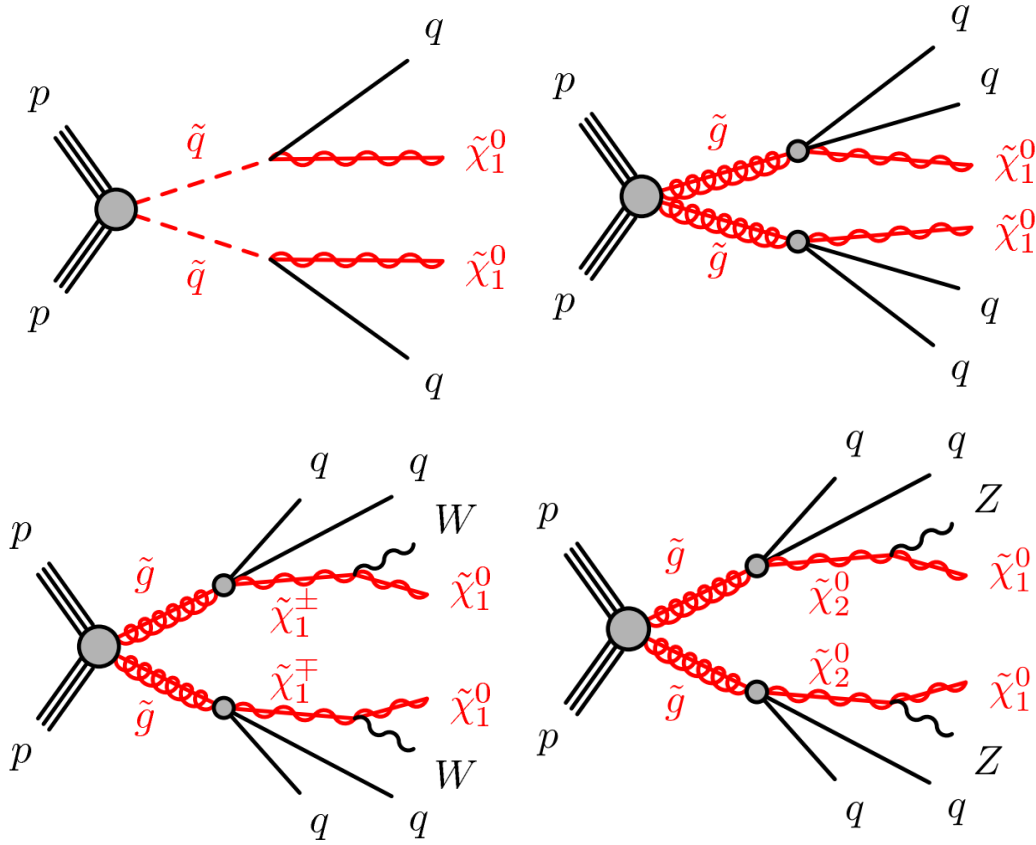


Figure 3.3: SUSY signals considered in this thesis

483 of $SU(3)C$.

484 In the case of disquark production, the most common decay mode of the squark in
 485 the MSSM is a decay directly to the LSP plus a single SM quark [15]. This means the
 486 basic search strategy of disquark production is two jets from the final state quarks,
 487 plus missing transverse energy for the LSPs. There are also cascade decays, the most
 488 common of which, and the only one considered in this thesis, is $\tilde{q} \rightarrow q\chi_1^\pm \rightarrow qW^\pm\chi_1^0$.

489 For digluino production, the most common decay is $\tilde{g} \rightarrow g\tilde{q}$, due to the large
 490 g_S coupling. The squark then decays as listed above. In this case, we generically
 491 search for four jets and missing transverse energy from the LSPs. We can also have
 492 the squark decay in association with a W^\pm or Z^0 ; in this thesis, we are interested in
 493 those cases where this vector boson goes hadronically.

494 In the context of experimental searches for SUSY, we often consider *simplified*

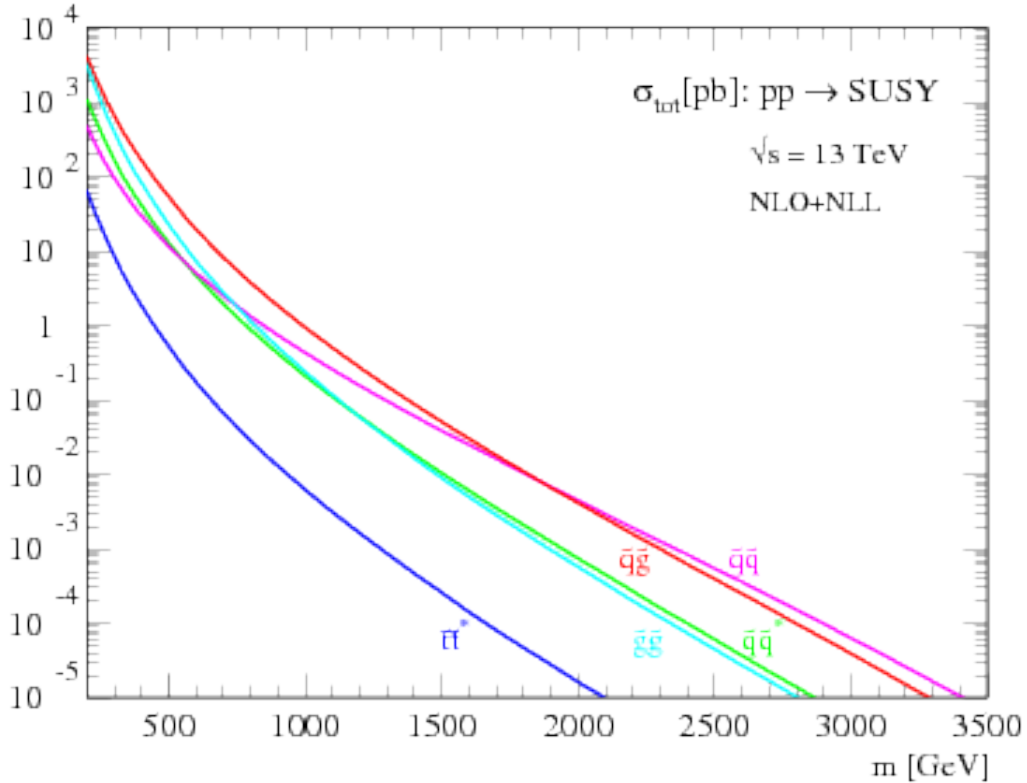


Figure 3.4: SUSY production cross-sections as a function of sparticle mass at $\sqrt{s} = 13$ TeV.

models. These models make certain assumptions which allow easy comparisons of results by theorists and rival experimentalists. In the context of this thesis, the simplified models will make assumptions about the branching ratios described in the preceding paragraphs. In particular, we will often choose a model where the decay of interest occurs with 100% branching ratio. This is entirely for ease of interpretation by other physicists⁵, but it is important to recognize that these are more a useful comparison tool, especially with limits, than a strict statement about the potential masses of sought-after beyond the Standard Model particle.

⁵In the author's opinion, this often leads to more confusion than comprehension. We will revisit the shortcomings of simplified models in the Conclusion to this thesis.

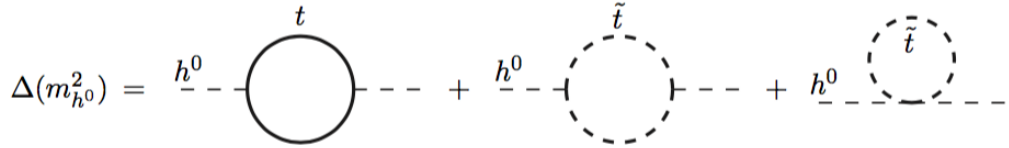


Figure 3.5: Loop diagrams correct the Higgs mass in the MSSM

503 3.4 How SUSY solves the problems with the SM

504 We now return to the issues with the Standard Model as described in Ch.2 to see
 505 how these issues are solved by supersymmetry.

506 Quadratic divergences to the Higgs mass

The quadratic divergences induced by the loop corrections to the Higgs mass, for example from the top Yukawa coupling, goes as

$$\delta m_H^2 \approx \left(\frac{m_t}{8\pi^2 \langle \phi \rangle_{VEV}} \right)^2 \Lambda_{Planck}^2. \quad (3.16)$$

507 The miraculous thing about SUSY is each of these terms *automatically* comes
 508 with a term which exactly cancels this contribution[15]. The fermions and bosons
 509 have opposite signs in this loop diagram to all orders in perturbation theory, which
 510 completely solves the hierarchy problem. This is the most well-motivated reason for
 511 supersymmetry.

512 Gauge coupling unification

513 An additional motivation for supersymmetry is seen by the gauge coupling unification
 514 high scales. In the Standard Model, as we saw the gauge couplings fail to unify at
 515 high energies. In the MSSM and many other forms of supersymmetry, the gauge
 516 couplings unify at high energy, as can be seen in Fig.???. This provides additional
 517 aesthetic motivation for supersymmetric theories.



Figure 3.6: The running of Standard Model gauge couplings; compare to Fig.2.4. The MSSM gauge couplings nearly intersect at high energies.

518 Dark matter

519 As we discussed previously, the lack of any dark matter candidate in the Standard
 520 Model naturally leads to beyond the Standard Model theories. In the Standard Model,
 521 there is a natural dark matter candidate in the lightest supersymmetric particle[15]
 522 The LSP would in dark matter experiments be called a *weakly-interacting massive*
 523 *particle* (WIMP), which is a type of cold dark matter [22, 84]. These WIMPS would
 524 only interact through the weak force and gravity, which is exactly as a model like the
 525 MSSM predicts for the neutralino. In Fig.3.7, we can see the current WIMP exclusions
 526 for a given mass. The range of allowed masses which have not been excluded for LSPs
 527 and WIMPs have significant overlap. This provides additional motivation outside of
 528 the context of theoretical details.



Figure 3.7: WIMP exclusions from direct dark matter detection experiments.

3.5 Conclusions

Supersymmetry is the most well-motivated theory for physics beyond the Standard Model. It provides a solution to the hierarchy problem, leads to gauge coupling unification, and provides a dark matter candidate consistent with galactic rotation curves. As noted in this chapter, due to the LSPs in the final state, most SUSY searches require a significant amount of missing transverse energy in combination with jets of high transverse momentum. However, there is some opportunity to do better than this, especially in final states where one has two weakly-interacting LSPs on opposite sides of some potentially complicated decay tree. We will see how this is done in Ch.??.

The Large Hadron Collider

541 The Large Hadron Collider (LHC) produces high-energy protons which are collided
 542 at the center of multiple large experiments at CERN on the outskirts of Geneva,
 543 Switzerland [85]. The LHC produces the highest energy collisions in the world,
 544 with design center-of-mass energy of $\sqrt{s} = 14$ TeV, which allows the experiments
 545 to investigate physics far beyond the reach of previous colliders. This chapter will
 546 summarize the basics of accelerator physics, especially with regards to discovering
 547 physics beyond the Standard Model. We will describe the CERN accelerator complex
 548 and the LHC.

549 **4.1 Basics of Accelerator Physics**

550 This section follows closely the presentation of [86].

Simple particle accelerators simply rely on the acceleration of charged particles in a static electric field. Given a field of strength E , charge q , and mass m , this is simply

$$a = \frac{qE}{m}. \quad (4.1)$$

551 For a given particle with a given mass and charge, this is limited by the static electric
 552 field which can be produced, which in turn is limited by electrical breakdown at high
 553 voltages.

554 There are two complementary solutions to this issue. First, we use the *radio*
 555 *frequency acceleration* technique. We call the devices used for this *RF cavities*. The

556 cavities produce a time-varied electric field, which oscillate such that the charged
557 particles passing through it are accelerated towards the design energy of the RF
558 cavity. This oscillation also induces the particles into *bunches*, since particles which
559 are slightly off in energy from that induced by the RF cavity are accelerated towards
560 the design energy.

Second, one bends the particles in a magnetic field, which allows them to pass through the same RF cavity over and over. This second process is often limited by *synchrotron radiation*, which describes the radiation produced when a charged particle is accelerated. The power radiated is

$$P \sim \frac{1}{r^2} \left(E/m \right)^4 \quad (4.2)$$

561 where r is the radius of curvature and E, m is the energy (mass) of the charged
562 particle. Given an energy which can be produced by a given set of RF cavities (which
563 is *not* limited by the mass of the particle), one then has two options to increase the
564 actual collision energy : increase the radius of curvature or use a heavier particle.
565 Practically speaking, the easiest options for particles in a collider are protons and
566 electrons, since they are (obviously) copious in nature and do not decay¹. Given the
567 dependence on mass, we can see why protons are used to reach the highest energies.
568 The tradeoff for this is that protons are not point particles, and we thus we don't
569 know the exact incoming four-vectors of the protons, as discussed in Ch.2.

The particle *beam* refers to the bunches all together An important property of a beam of a particular energy E , moving in uniform magnetic field B , containing particles of momentum p is the *beam rigidity* :

$$R \equiv rB = p/c. \quad (4.3)$$

570 The linear relation between r and p , or alternatively B and p have important
571 consequences for LHC physics. For hadron colliders, this is the limiting factor on

¹Muon colliders are a really cool option at high energies, since the relativistic γ factor gives them a relatively long lifetime in the lab frame.

572 going to higher energy scales; one needs a proportionally larger magnetic field to
573 keep the beam accelerating in a circle.

574 Besides the rigidity of the beam, the most important quantities to characterize
575 a beam are known as the (normalized) *emittance* ϵ_N and the *betatron function* β .
576 These quantities determine the transverse size σ of a relativistic beam $v \gtrsim c$ beam :
577 $\sigma^2 = \beta^* \epsilon_N / \gamma_{\text{rel}}$, where β^* is the value of the betatron function at the collision point
578 and γ_{rel} is the Lorentz factor.

These quantities determine the *instantaneous luminosity* L of a collider, which combined with the cross-section σ of a particular physics process, give the rate of this physics process :

$$R = L\sigma. \quad (4.4)$$

The instantaneous luminosity L is given by :

$$L = \frac{f_{\text{rev}} N_b^2 F}{4\pi\sigma^2} = \frac{f_{\text{rev}} n N_b^2 \gamma_{\text{rel}} F}{4\pi\beta^* \epsilon_N}. \quad (4.5)$$

579 Here we have introduced the frequency of revolutions f_{rev} , the number of bunches n ,
580 the number of protons per bunch N_b^2 , and a geometric factor F related to the crossing
581 angle of the beams.

The *integrated luminosity* $\int L$ gives the total number of a particular physics process P , with cross-section σ_P .

$$N_P = \sigma_P \int L. \quad (4.6)$$

582 Due to this simple relation, one can also quantify the “amount of data delivered” by
583 a collider simply by $\int L$.

584 4.2 Accelerator Complex

585 The Large Hadron Collider is the last accelerator in a chain of accelerators which
586 together form the CERN accelerator complex, which can be seen in 4.1. The protons



Figure 4.1: The CERN accelerator complex.

begin their journey to annihilation in a hydrogen source, where they are subsequently ionized. The first acceleration occurs in the Linac 2, a linear accelerator composed of RF cavities. The protons leave the Linac 2 at an energy of 50 MeV and enter the Proton Synchrotron Booster (PSB). The PSB contains four superimposed rings, which accelerate the protons to 1.4 GeV. The protons are then injected into the Proton Synchrotron (PS). This synchrotron increases the energy up to 25 GeV. After leaving the PS, the protons enter the Super Proton Synchrotron (SPS). This is the last step before entering the LHC ring, and the protons are accelerated to 450 GeV. From the SPS, the protons are injected into the beam pipes of the LHC. The process to fill the LHC rings with proton bunches from start to finish typically takes about four minutes.

598 **4.3 Large Hadron Collider**

The Large Hadron Collider is the final step in the CERN accelerator complex, and produces the collisions analyzed in this thesis. From the point of view of experimentalists on the general-purpose ATLAS and CMS experiments, the main goal of the LHC is to deliver collisions at the highest possible energy, with the highest possible instantaneous luminosity. The LHC was installed in the existing 27 km tunnel used by the Large Electron Positron (LEP) collider [87]. This allowed the existing accelerator complex at CERN, described in the previous section, to be used as the injection system to prepare the protons up to 450 GeV. Many aspects of the LHC design were decided by this very fact, and specified the options allowed to increase the energy or luminosity. In particular, the radius of the tunnel was already specified; from Eq.4.3, this implies the momentum (or energy) of the beam is entirely determined by the magnetic field. Given the 27 km circumference of the LEP tunnel, one can calculate the required magnetic field to reach the 7 TeV per proton design energy of the LHC :

$$r = C/2\pi = 4.3 \text{ km} \quad (4.7)$$

$$\rightarrow B = \frac{p}{rc} = 5 \text{ T} \quad (4.8)$$

599 In fact, the LHC consists of 8 528 m straight portions consisting of RF cavities, used
600 to accelerate the particles, and 8 circular portions which bend the protons around the
601 LHC ring. These circular portions actually have a slightly smaller radius of curvature
602 $r = 2804 \text{ m}$, and we require $B = 8.33 \text{ T}$. To produce this large field, we need to use
603 superconducting magnets, as discussed in the next section.

604 **Magnets**

605 There are many magnets used by the LHC machine, but the most important are the
606 1232 dipole magnets; a schematic is shown in Fig.4.2 and a photograph is shown in



CERN AC/DI/MM — 2001/06

Figure 4.2: Schematic of an LHC dipole magnet.

607 Fig.4.3.

608 The magnets are made of Niobium and Titanium. The maximum field strength is
 609 10 T when cooled to 1.9 Kelvin. The magnets are cooled by superfluid helium, which
 610 is supplied by a large cryogenic system. Due to heating between the eight helium
 611 refrigerators and the beampipe, the helium is cooled in the refrigerators to 1.8 K.

612 A failure in the cooling system can cause what is known as a *quench*. If the
 613 temperature goes above the critical superconducting temperature, the metal loses its
 614 superconducting properties, which leads to a large resistance in the metal. This leads
 615 to rapid temperature increases, and can cause extensive damages if not controlled.

616 The dipole magnets are 16.5 meters long with a diameter of 0.57 meters. There
 617 are two individual beam pipes inside each magnet, which allows the dipoles to house
 618 the beams travelling in both directions around the LHC ring. They curve slightly,
 619 at an angle of 5.1 mrad, which carefully matches the curvature of the ring. The

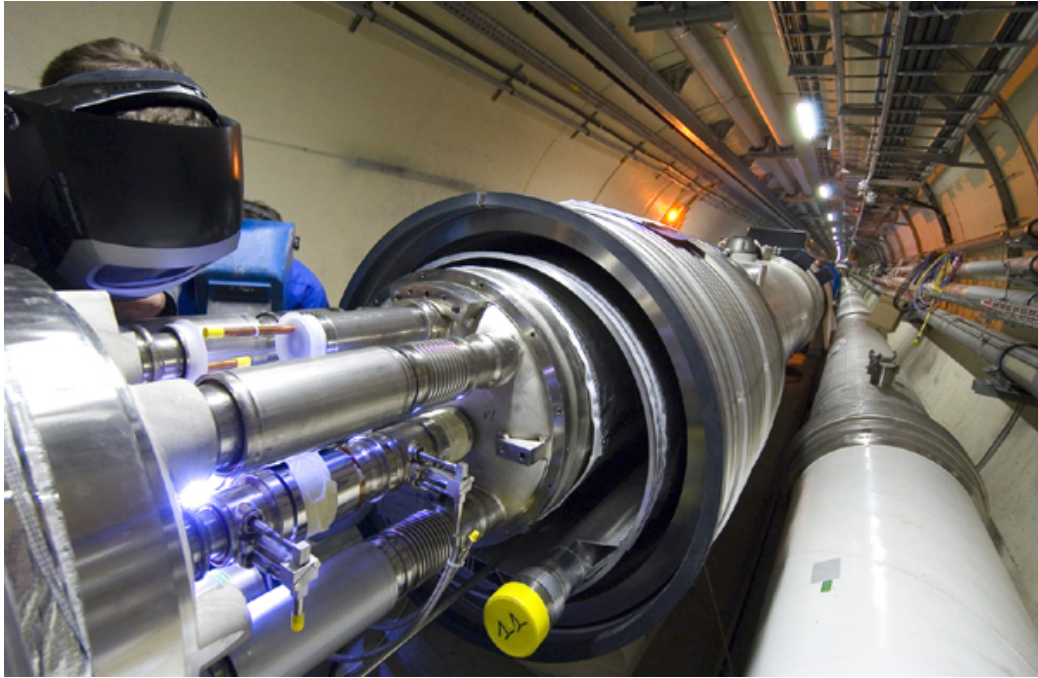


Figure 4.3: Photograph of a technician connecting an LHC dipole magnet.

620 beampipes inside of the magnets are held in high vacuum, to avoid stray particles
621 interacting with the beam.

622 **4.4 Dataset Delivered by the LHC**

623 In this thesis, we analyze the data delivered by the LHC to ATLAS in the 2015 and
624 2016 datasets. The beam parameters relevant to this dataset are available in Table
625 [4.1](#).

626 The peak instantaneous luminosity delivered in 2015 (2016) was $L =$
627 $5.2(11) \text{ cm}^{-2}\text{s}^{-1} \times 10^{33}$. One can note that the instantaneous luminosity delivered in
628 the 2016 dataset exceeds the design luminosity of the LHC. The total integrated
629 luminosity delivered was 13.3 fb^{-1} . In Figure [4.4](#), we display the integrated luminosity
630 as a function of day for 2015 and 2016.

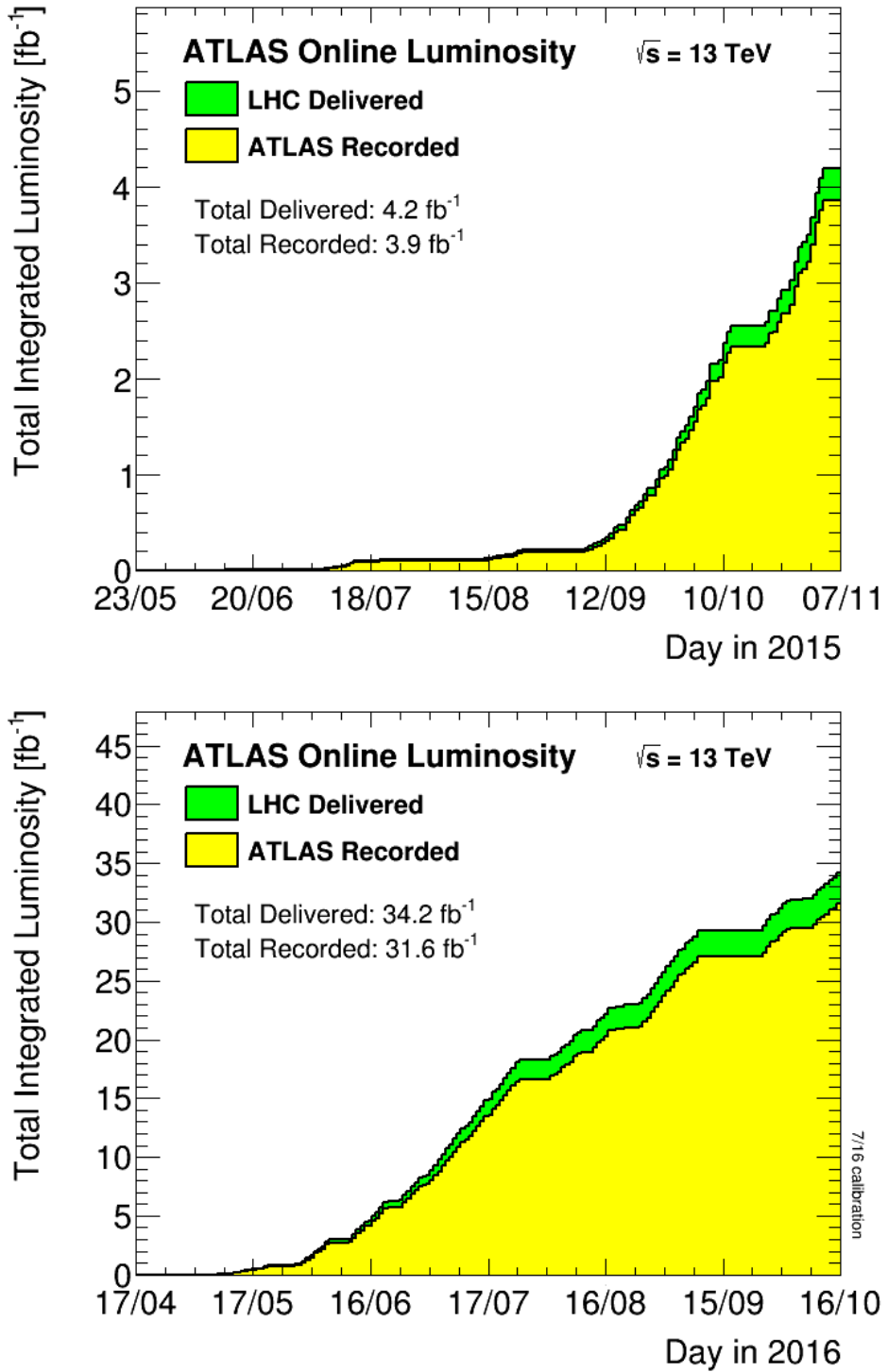


Figure 4.4: Integrated Luminosity delivered by the LHC and collected by ATLAS in the 2015 and 2016 datasets.

Parameter	Injection	Extraction
Energy (GeV)	450	7000
Rigidity (T-m)	3.8	23353
Bunch spacing (ns)	25	25
Design Luminosity ($\text{cm}^{-2}\text{s}^{-1} \times 10^3$)	-	1.0
Bunches per proton beam	2808	2808
Protons per bunch	1.15 e11	1.15 e11
Beam lifetime (hr)	-	10
Normalized Emittance ϵ_N (mm μrad)	3.3	3.75
Betatron function at collision point β^* (cm)	-	55

Table 4.1: Beam parameters of the Large Hadron Collider.

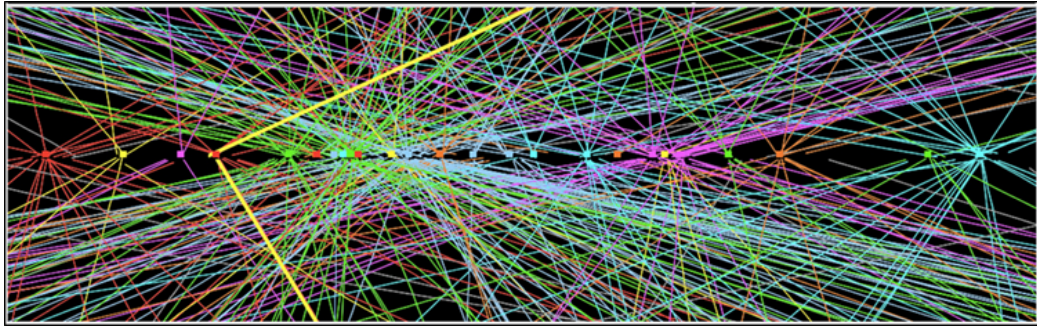


Figure 4.5: Simulated event with many pileup vertices.

631 Pileup

632 *Pileup* is the term for the additional proton-proton interactions which occur during
 633 each bunch crossing of the LHC. At the beginning of the LHC physics program, there
 634 had not been a collider which averaged more than a single interaction per bunch
 635 crossing. In the LHC, each bunch crossing (or *event*) generally contains multiple
 636 proton-proton interactions. An simulated event with many *vertices* can be seen in
 637 Fig.4.5. The so-called *primary vertex* (or *hard scatter vertex*) refers to the vertex
 638 which has the highest Σp_T^2 ; this summation occurs over the *tracks* in the detector,
 639 which we will describe later[**ATL-INDET-PUB-2009-001**]. We then distinguish
 640 between *in-time* pileup and *out-of-time* pileup. In-time pileup refers to the additional
 641 proton-proton interactions which occur in the event. Out-of-time pileup refers to
 642 effects related to proton-proton interactions previous bunch crossings.

643 We quantify in-time pileup by the number of “primary”² vertices in a particular
644 event. To quantify the out-of-time pileup, we use the average number of interactions
645 per bunch crossing $\langle \mu \rangle$ over some human-scale time. In Figure 4.6, we show the
646 distribution of μ for the dataset used in this thesis.

²The primary vertex is as defined above, but we unfortunately use the same name here.



Figure 4.6: Mean number of interactions per bunch crossing in the 2015 and 2016 datasets.

The ATLAS detector

649 The dataset analyzed in this thesis was taken by the ATLAS detector [88], which is
 650 located at the “Point 1” cavern of the LHC beampipe, just across the street from
 651 the main CERN campus. The much-maligned acronym stands for *A Toroidal LHC*
 652 *ApparatuS*. ATLAS is a massive cylindrical detector, with a radius of 12.5 m and a
 653 length of 44 m, with nearly hermitic coverage around the collision point. It consists
 654 of multiple subdetectors; each plays a role in ATLAS’s ultimate purpose of measuring
 655 the energy, momentum, and type of the particles produced in collisions delivered by
 656 the LHC. These subdetectors are immersed in a hybrid solenoid-toroid magnet system
 657 whichs forces charged particles to curve, which allows for precise measurements of
 658 their momenta. These magnetic fields are maximized in the central solenoid magnet,
 659 which contains a magnetic field of 2 T. A schematic of the detector can be seen in
 660 5.1.

661 The *inner detector* (ID) lies closest to the collision point, and contains three
 662 separate subdetectors. It provides pseudorapidity¹coverage of $|\eta| < 2.5$ for charged
 663 particles to interact with the tracking material. The tracks reconstructed from the
 664 inner detector hits are used to reconstruct the primary vertices, as noted in Ch.??,

¹ATLAS uses a right-handed Cartesian coordinate system; the origin is defined by the nominal beam interaction point. The positive- z direction is defined by the incoming beam travelling counterclockwise around the LHC. The positive- x direction points towards the center of the LHC ring from the origin, and the positive- y direction points upwards towards the sky. For particles of transverse (in the $x - y$ plane) momentum $p_T = \sqrt{p_x^2 + p_y^2}$ and energy E , it is generally most convenient fully describe this particle’s kinematics as measured by the detector in the (p_T, ϕ, η, E) basis. The angle $\phi = \arctan(p_y/p_x)$ is the standard azimuthal angle, and $\eta = \ln \tan(\theta/2)$ is known as the pseudorapidity, and defined based on the standard polar angle $\theta = \arccos(p_z/p_T)$. For locations of i.e. detector elements, both (r, ϕ, η) and (z, ϕ, η) can be useful.

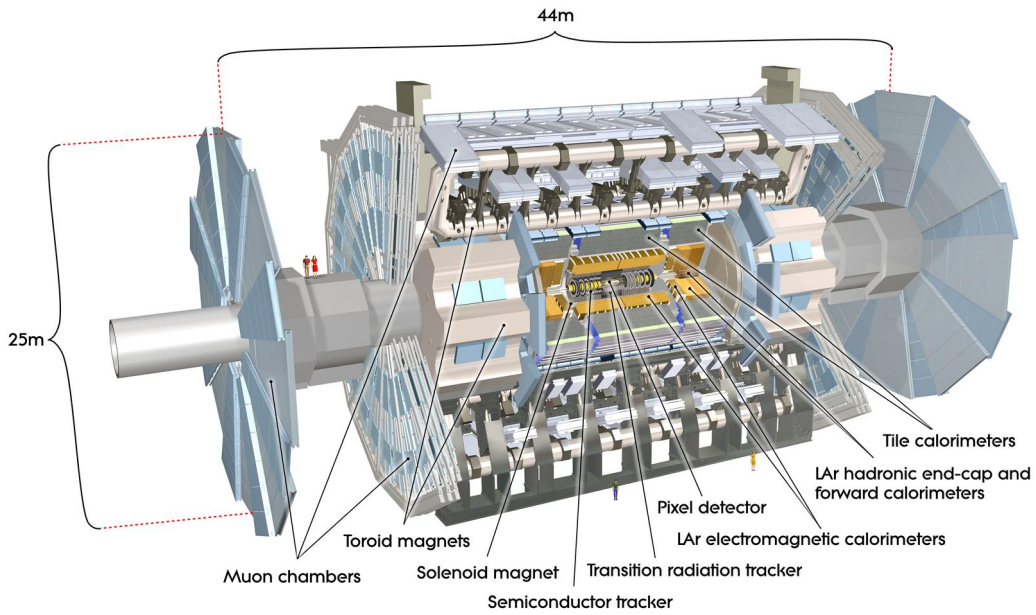


Figure 5.1: The ATLAS detector

and to determine the momemta of charged particles. The ATLAS *calorimeter* consists of two subdetectors, known as the *electromagnetic* and *hadronic* calorimeters. These detectors stop particles in their detector material, and measure the energy deposition inside, which measures the energy of the particles deposited. The calorimeters provide coverage out to pseudorapidity of $|\eta| < 4.9$. The muon spectrometer is aptly named; it is specifically used for muons, which are the only particles which generally reach the outer portions of the detector. In this region, we have the large tracking systems of the muon spectrometer, which provide precise measurements of muon momenta. The muon spectrometer has pseudorapidity coverage of $|\eta| < 2.7$.

5.1 Magnets

ATLAS contains multiple magnetic systems; primarily, we are concerned with the solenoid, used by the inner detector, and the toroids located outside of the ATLAS calorimeter. A schematic is shown in Fig.5.2. These magnetic fields are used to bend

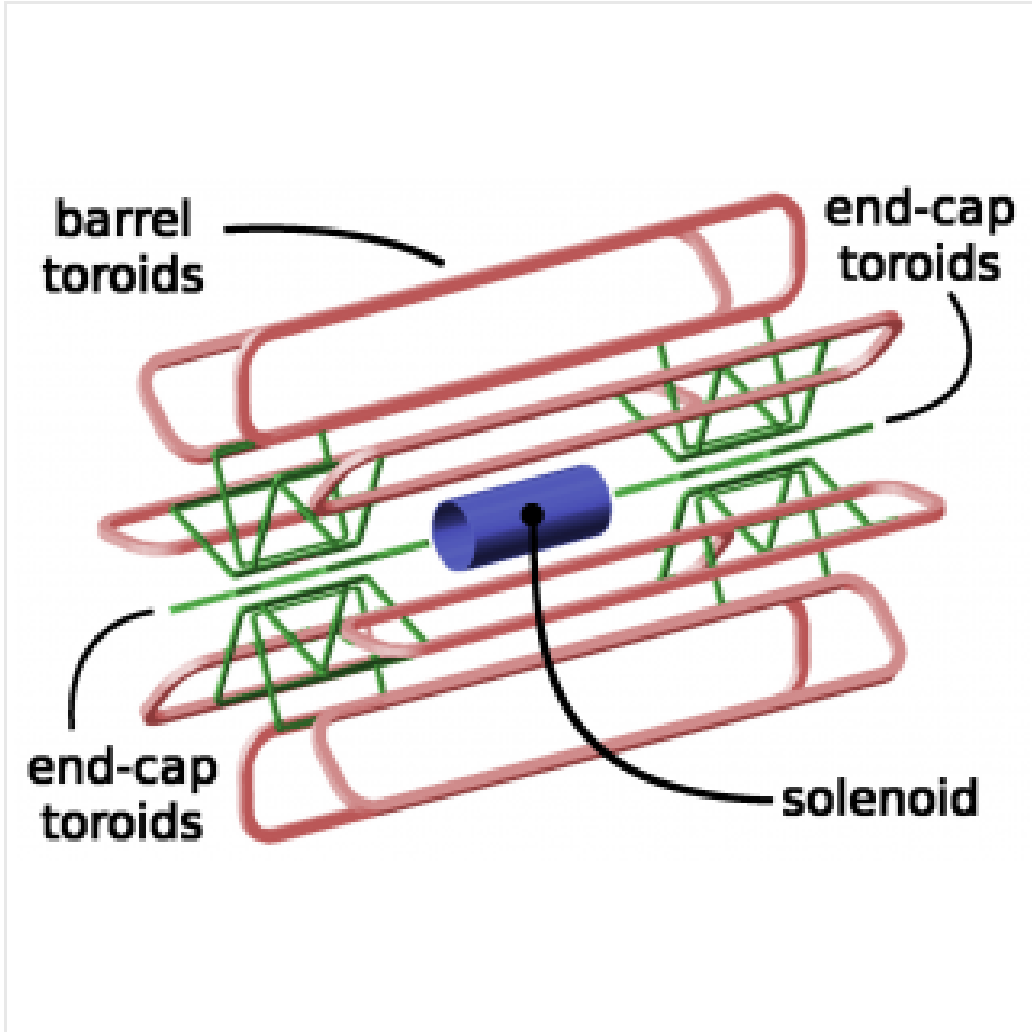


Figure 5.2: The ATLAS magnet system

678 charged particles under the Lorentz force, which subsequently allows one to measure
679 their momentum.

680 The ATLAS central solenoid is a 2.3 m diameter, 5.3 m long solenoid at the center
681 of the ATLAS detector. It produces a uniform magnetic field of 2 T; this strong field
682 is necessary to accurately measure the charged particles in this field. An important
683 design constraint for the central solenoid was the decision to place it in between the
684 inner detector and the calorimeters. To avoid excessive impacts on measurements in
685 the calorimetry, the central solenoid must be as transparent as possible².

²This is also one of the biggest functional differences between ATLAS and CMS; in CMS, the



Figure 5.3: The ATLAS inner detector

686 The toroid system consists of eight air-core superconducting barrel loops; these
 687 give ATLAS its distinctive shape. There are also two endcap air-core magnets. These
 688 produce a magnetic field in a region of approximately 26 m in length and 10 m of
 689 radius. The magnetic field in this region is non-uniform, due to the prohibitive costs
 690 of a solenoid magnet of that size.

691 **5.2 Inner Detector**

692 The ATLAS inner detector consists of three separate tracking detectors, which are
 693 known as, in order of increasing distance from the interaction point, the Pixel
 694 Detector, Semiconductor Tracker (SCT), and the Transition Radiation Tracker
 695 (TRT). When charged particles pass through these tracking layers, they produce
 696 *hits*, which using the known 2 T magnetic field, allows the reconstruction of *tracks*.
 697 Tracks are used as inputs for reconstruction of many higher-level physics objects,

solenoid is outside of the calorimeters.

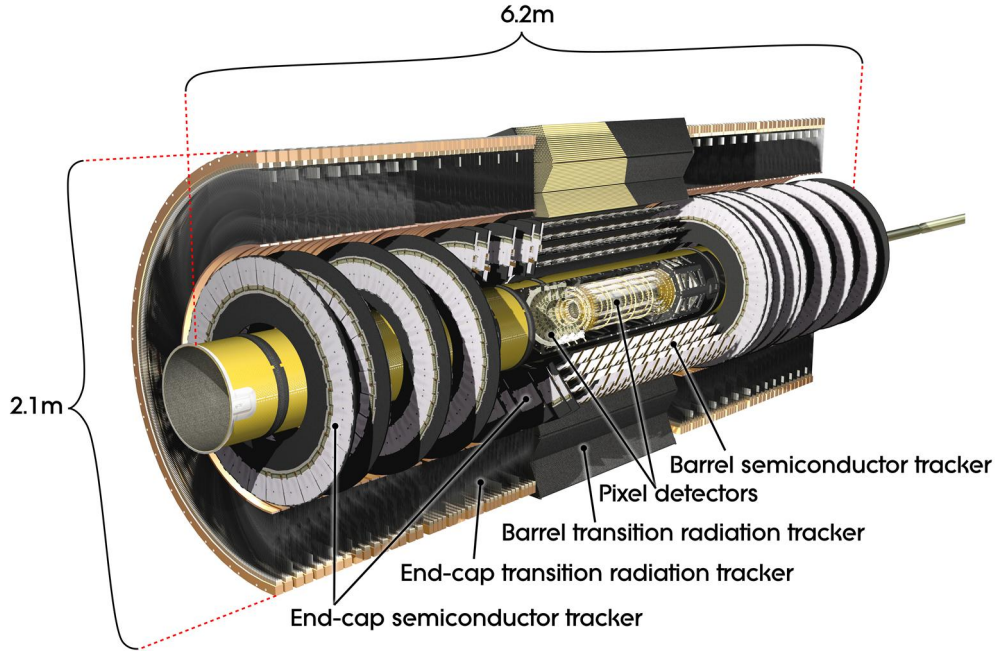


Figure 5.4: The ATLAS pixel detector

such as electrons, muons, photons, and E_T^{miss} . Accurate track reconstruction is thus crucial for precise measurements of charged particles.

Pixel Detector

The ATLAS pixel detector consists four layers of silicon “pixels”. This refers to the segmentation of the active medium into the pixels; compare to the succeeding silicon detectors, which will use silicon “strips”. This provides precise 3D hit locations. The layers are known as the “Insertable”³B-Layer (IBL), the B-Layer (or Layer-0), Layer-1, and Layer-2, in order of increasing distance from the interaction point. These layers are very close to the interaction point, and therefore experience a large amount of radiation.

Layer-1, Layer-2, and Layer-3 were installed with the initial construction of ATLAS. They contain front-end integrated electronics (FEI3s) bump-bonded to 1744

³Very often, the IBL is mistakenly called the Inner B-Layer, which would have been a much more sensible name.

710 silicon modules; each module is $250\ \mu\text{m}$ in thickness and contains 47232 pixels. These
711 pixels have planar sizes of $50 \times 400\ \mu^2$ or $50 \times 600\ \mu^2$, to provide highly accurate
712 location information. The FEI3s are mounted on long rectangular structures known
713 as staves, which encircle the beam pipe. A small tilt to each stave allows full coverage
714 in ϕ even with readout systems which are installed. These layers are at radia of 50.5
715 mm, 88.5 mm, and 122.5 mm from the interaction point.

716 The IBL was added to ATLAS after Run1 in 2012 at a radius of 33 mm from the
717 interaction point. The entire pixel detector was removed from the center of ATLAS
718 to allow an additional pixel layer to be installed. The IBL was required to preserve
719 the integrity of the pixel detector as radiation damage leads to inoperative pixels in
720 the other layers. The IBL consists of 448 FEI4 chips, arranged onto 14 staves. Each
721 FEI4 has 26880 pixels, of planar size $50 \times 250\ \mu\text{m}$. This smaller granularity was
722 required due to the smaller distance to the interaction point.

723 In total, a charged particle passing through the inner detector would expect to
724 leave four hits in the pixel detector.

725 Semiconductor Tracker

726 The SCT is directly beyond Layer-2 of the pixel detector. This is a silicon strip
727 detector, which do not provide the full 3D information of the pixel detector. The
728 dual-sensors of the SCT contain 2×768 individual strips; each strip has area $6.4\ \text{cm}^2$.
729 The SCT dual-sensor is then double-layered, at a relative angle of 40 mrad;
730 together these layers provide the necessary 3D information for track reconstruction.
731 There are four of these double-layers, at radia of 284 mm, 355 mm, 427 mm, and 498
732 mm. These double-layers provide hits comparable to those of the pixel detector, and
733 we have four additional hits to reconstruct tracks for each charged particle.

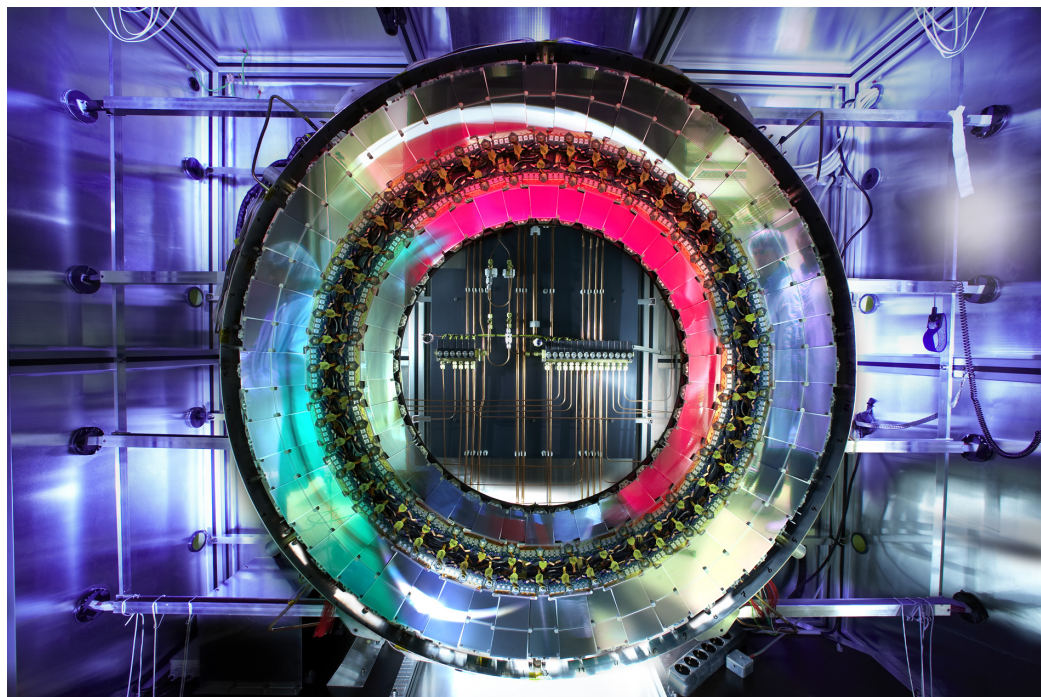


Figure 5.5: A ring of the Semiconductor Tracker

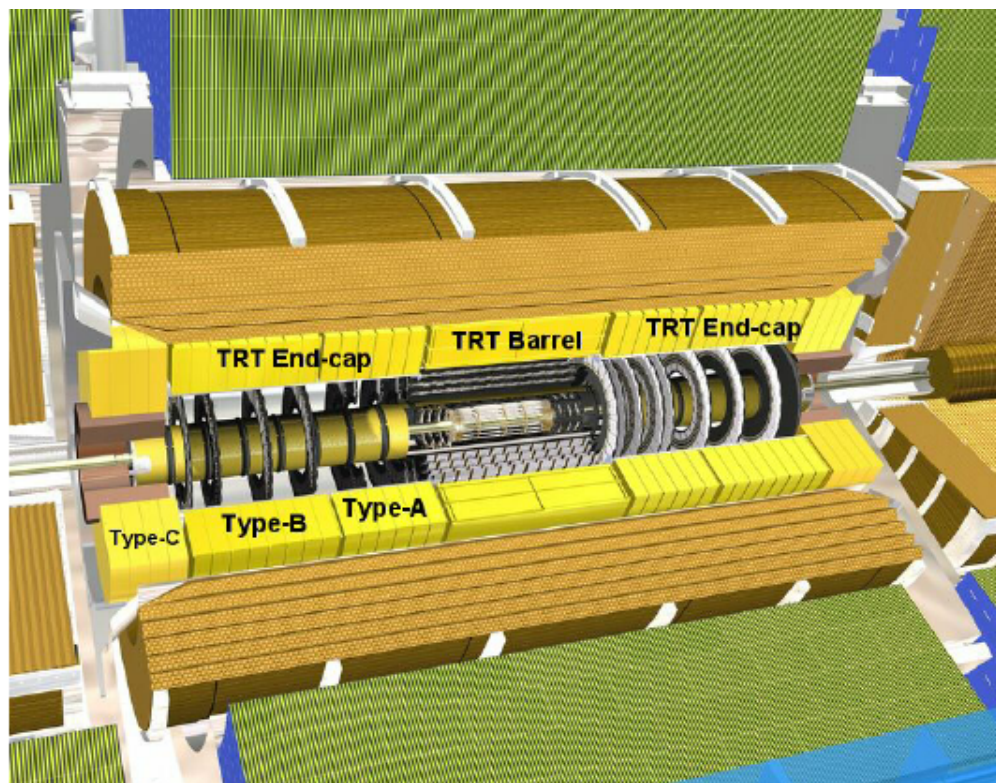


Figure 5.6: A schematic of the Transition Radiation Tracker

734 **Transition Radiation Tracker**

735 The Transition Radiation Tracker is the next detector radially outward from the SCT.
736 It contains straw drift tubes; these contain a tungsten gold-plated wire of $32 \mu\text{m}$
737 diameter held under high voltage (-1530 V) with the edge of the Kapton-aluminum
738 tube. They are filled with a gas mixture of primarily xenon that is ionized when
739 a charged particle passes through the tube. The ions are collected by the “drift”
740 due to the voltage inside the tubes, which is read out by the electronics. This gives
741 so-called “continuous tracking” throughout the tube, due to the large number of ions
742 produced.

743 The TRT is so-named due to the *transition radiation* (TR) it induces. Due to
744 the dielectric difference between the gas and tubes, TR is induced. This is important
745 for distinguishing electrons from their predominant background of minimum ionizing
746 particles. Generally, electrons have a much larger Lorentz factor than minimum
747 ionizing particles, which leads to additional TR. This can be used as an additional
748 handle for electron reconstruction.

749 **5.3 Calorimetry**

750 The calorimetry of the ATLAS detector also includes multiple subdetectors; these sub-
751 detectors allow precise measurements of the electrons, photons, and hadrons produced
752 by the ATLAS detector. Generically, calorimeters work by stopping particles in their
753 material, and measuring the energy deposition. This energy is deposited as a cascade
754 particles induce from interactions with the detector material known *showers*. ATLAS
755 uses *sampling* calorimeters; these alternate a dense absorbing material, which induces
756 showers, with an active layer which measures energy depositions by the induced
757 showers. Since some energy is deposited into the absorption layers as well, the energy
758 depositions must be properly calibrated for the detector.

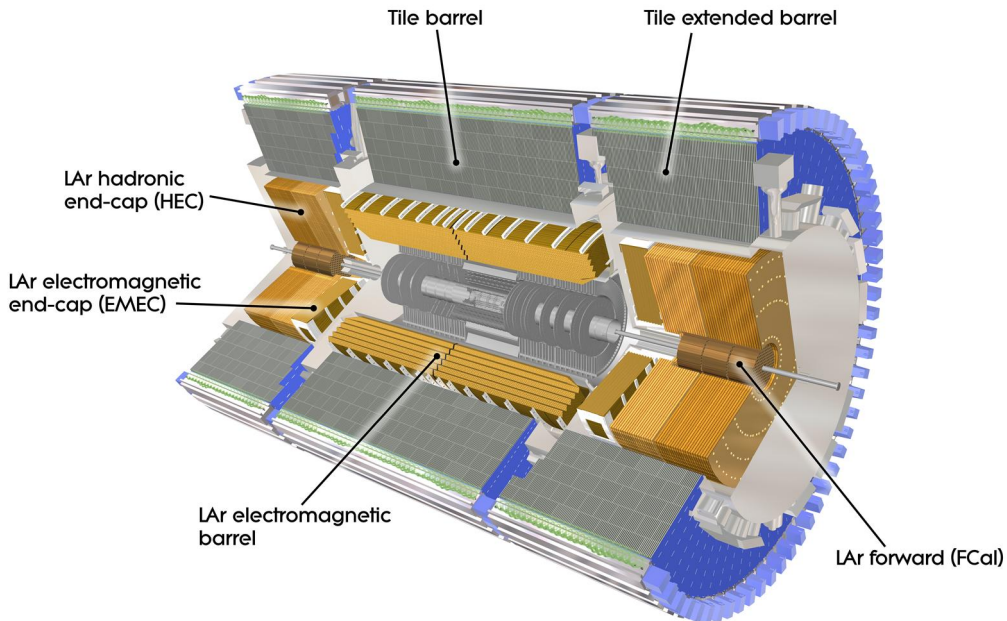


Figure 5.7: The ATLAS calorimeter

759 Electromagnetic objects (electrons and photons) and hadrons have much different
 760 interaction properties, and thus we need different calorimeters to accurately measure
 761 these different classes of objects; we can speak of the *electromagnetic* and *hadronic*
 762 calorimeters. ATLAS contains four separate calorimeters : the liquid argon (LAr)
 763 electromagnetic barrel calorimeter, the Tile barrel hadronic calorimeter, the LAr
 764 endcap electromagnetic calorimeter, the LAr endcap hadronic calorimeter, and the
 765 LAr Forward Calorimeter (FCal). Combined, these provide full coverage in ϕ up to
 766 $|\eta| < 4.9$, and can be seen in Fig.5.7.

767 **Electromagnetic Calorimeters**

768 The electromagnetic calorimeters of the ATLAS detector consist of the barrel and
 769 endcap LAr calorimeters. These are arranged into an ingenious “accordion” shape,
 770 shown in 5.8, which allows full coverage in ϕ and exceptional coverage in η while
 771 still allowing support structures for detector operation. The accordion is made of



Figure 5.8: A schematic of a subsection of the barrel LAr electromagnetic calorimeter

772 layers with liquid argon (active detection material) and lead (absorber) to induce
 773 electromagnetic showers. The LAr EM calorimeters are each more than 20 radiation
 774 lengths deep, which provides the high stopping power necessary to properly measure
 775 the electromagnetic showers.

776 The barrel component of the LAr EM calorimeter extends from the center of the
 777 detector out to $|\eta| < 1.475$. The calorimeter has a presampler, which measures the
 778 energy of any EM shower induced before the calorimeter. This has segmentation of
 779 $\Delta\eta = 0.025, \Delta\phi = .01$. There are three “standard” layers in the barrel, which have
 780 decreasing segmentation into calorimeter *cells* as one travels radially outward from
 781 the interaction point. The first layer has segmentation of $\Delta\eta = 0.003, \Delta\phi = .1$, and
 782 is quite thin relative to the other layers at only 4 radiation lengths deep. It provides
 783 precise η and ϕ measurements for incoming EM objects. The second layer is the
 784 deepest at 16 radiation lengths, with a segmentation of $\Delta\eta = 0.025, \Delta\phi = 0.025$. It



Figure 5.9: A schematic of Tile hadronic calorimeter

785 is primarily responsible for stopping the incoming EM particles, which dictates its
 786 large relative thickness, and measures most of the energy of the incoming particles.
 787 The third layer is only 2 radiation lengths deep, with a rough segmentation of $\Delta\eta =$
 788 0.05, $\Delta\phi = .025$. The deposition in this layer is primarily used to distinguish hadrons
 789 interacting electromagnetically and entering the hadronic calorimeter from the strictly
 790 EM objects which are stopped in the second layer.

791 The barrel EM calorimeter has a similar overall structure, but extends from
 792 $1.4 < |\eta| < 3.2$. The segmentation in η is better in the endcap than the barrel;
 793 the ϕ segmentation is the same. In total, the EM calorimeters contain about 190000
 794 individual calorimeter cells.

795 Hadronic Calorimeters

796 The hadronic calorimetry of ATLAS sits directly outside the EM calorimetry. It
 797 contains three subdetectors : the barrel Tile calorimeter, the endcap LAr calorimeter,

798 and the Forward LAr Calorimeter. Similar to the EM calorimeters, these are
799 sampling calorimeters that alternate steel (dense material) with an active layer
800 (plastic scintillator).

801 The barrel Tile calorimeter extends out to $|\eta| < 1.7$. There are again three layers,
802 which combined give about 10 interactions length of distance, which provides excellent
803 stopping power for hadrons. This is critical to avoid excess *punchthrough* to the muon
804 spectrometer beyond the hadronic calorimeters. The first layer has a depth of 1.5
805 interaction lengths. The second layer is again the thickest at a depth of 4.1 interaction
806 lengths; most of the energy of incoming particle is deposited here. Both the first and
807 second layer have segmentation of about $\Delta\eta = 0.1, \Delta\phi = 0.1$. Generally, one does not
808 need as fine of granularity in the hadronic calorimeter, since the energy depositions
809 in the hadronic calorimeters will be summed into the composite objects we know as
810 jets. The third layer has a thickness of 1.8 interaction lengths, with a segmentation of
811 $\Delta\eta = 0.2, \Delta\phi = 0.1$. The use of multiple layers allows one to understand the induced
812 hadronic shower as it propagates through the detector material.

813 The endcap LAr hadronic calorimeter covers the region $1.5 < |\eta| < 3.2$. It is
814 again a sampling calorimeter; the active material is LAr with a copper absorbed. It
815 does not use the accordion shape of the other calorimeters; it has a “standard” flat
816 shape perpendicular to the interaction point. The segmentation varies with η . For
817 $1.5 < |\eta| < 2.5$, the cells are $\Delta\eta = 0.1, \Delta\phi = 0.1$; in the region $2.5 < |\eta| < 3.2$, the
818 cells are $\Delta\eta = 0.2, \Delta\phi = 0.2$ in size.

819 The final calorimeter in ATLAS is the forward LAr calorimeter. Of those
820 subdetectors which are used for standard reconstruction techniques, the FCal sits
821 at the most extreme values of $3.1 < |\eta| < 4.9$. The FCal itself is made of three
822 subdetectors; FCal1 is actually an electromagnetic module, while FCal2 and FCal3
823 are hadronic. The absorber in FCal1 is copper, with a liquid argon active medium.
824 FCal2 and FCal3 also use a liquid argon active medium, with a tungsten absorber.

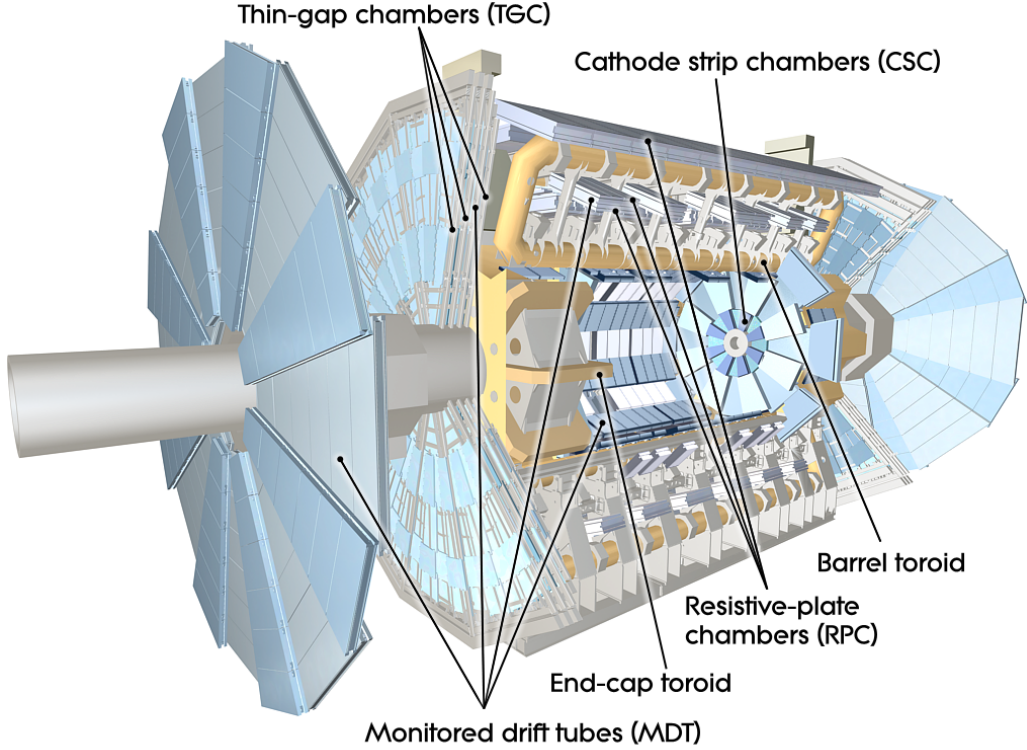


Figure 5.10: The ATLAS muon spectrometer

825 5.4 Muon Spectrometer

826 The muon spectrometer is the final major subdetector of the ATLAS detector.
 827 The muon spectrometer sits outside the hadronic calorimetry, with pseudorapidity
 828 coverage out to $|\eta| < 2.7$. The MS is a huge detector, with some detector elements
 829 existing as far as 11 m in radius from the interaction point. This system is used
 830 almost exclusively to measure the momenta of muons; these are the only measured
 831 SM particles which consistently exit the hadronic calorimeters. These systems provide
 832 a rough measurement, which is used in triggering (described in Ch.5.5), and a precise
 833 measurement to be used in offline event reconstruction as described in Ch.???. The
 834 MS produces tracks in a similar way to the ID; the hits in each subdetector are
 835 recorded and then tracks are produced from these hits. Muon spectrometer tracks are
 836 largely independent of the ID tracks due to the independent solenoidal and toroidal
 837 magnet systems used in the ID and MS respectively. The MS consists of four separate

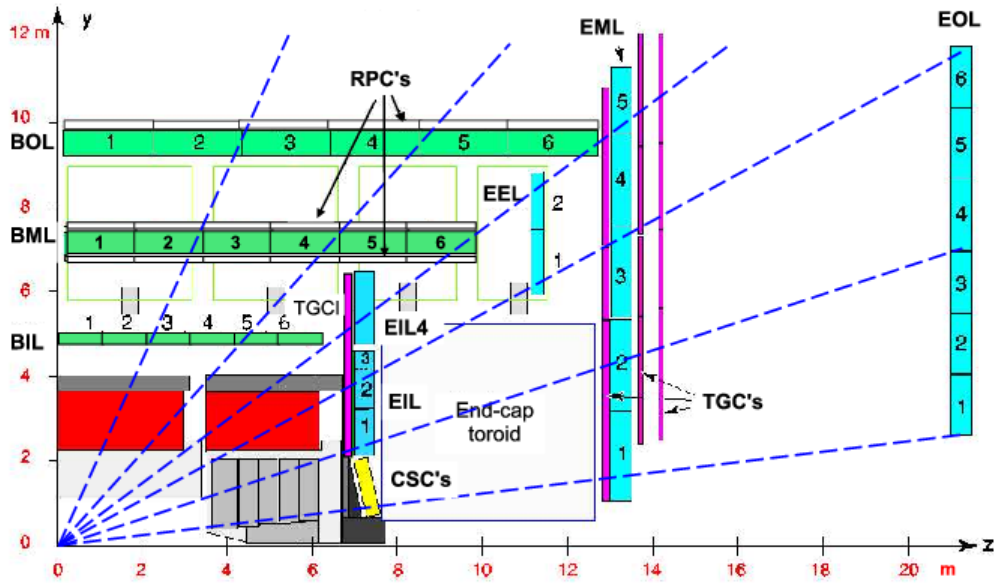


Figure 5.11: A schematic in z/η showing the location of the subdetectors of the muon spectrometer

838 subdetectors: the barrel region is covered by the Resistive Plate Chambers (RPCs)
 839 and Monitored Drift Tubes (MDTs) while the endcaps are covered by MDTs, Thin
 840 Gap Chambers (TGCs), and Cathode Strip Chambers (CSCs).

841 Monitored Drift Tubes

842 The MDT system is the largest individual subdetector of the MS. MDTs provide
 843 precision measurements of muon momenta as well as fast measurements used for
 844 triggers. There are 1088 MDT chambers providing coverage out to pseudorapidity
 845 $|\eta| < 2.7$; each consists of an aluminum tube containing an argon- CO_2 gas mixture.
 846 In the center of each tube there $50\mu\text{m}$ diameter tungsten-rhenium wire at a voltage of
 847 3080 V. A muon entering the tube will induce ionization in the gas, which will “drift”
 848 towards the wire due to the voltage. One measures this ionization as a current in the
 849 wire; this current comes with a time measurement related to how long it takes the
 850 ionization to drift to the wire.

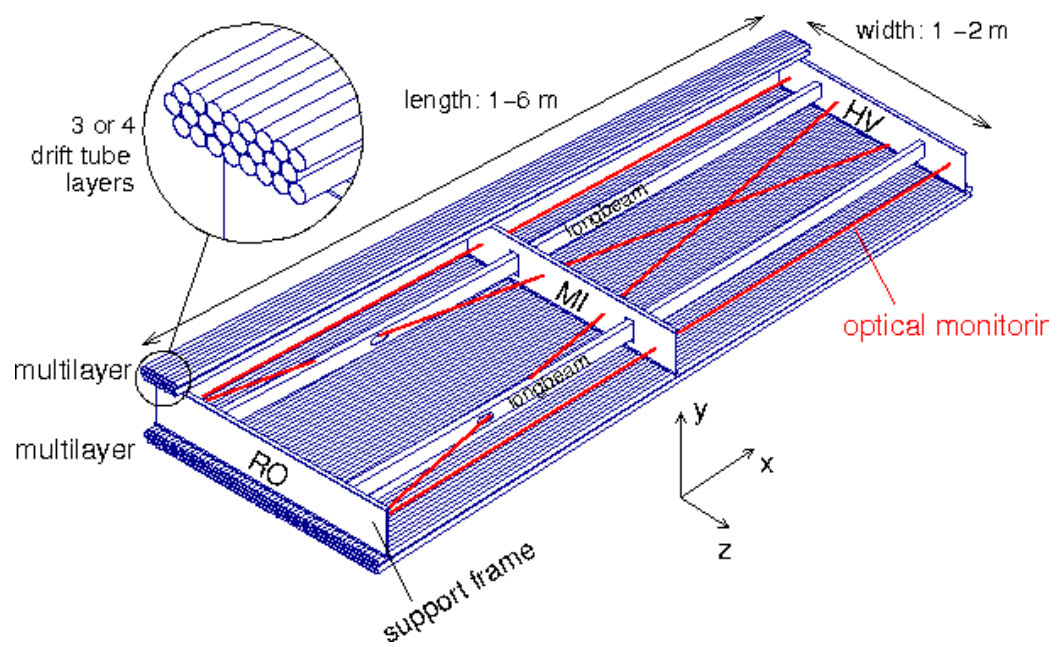


Figure 5.12: Schematic of a Muon Drift Tube chamber

851 These tubes are layered in a pattern shown in Fig.5.12. Combining the measure-
852 ments from the tubes in each layer gives good position resolution. The system consists
853 of three subsystems of these layers, at 5 m, 7m, and 9 m from the interaction point.
854 The innermost layer is directly outside the hadronic calorimeter. The combination of
855 these three measurements gives precise momenta measurements for muons.

856 Resistive Plate Chambers

857 The RPC system is alternated with the MDT system in the barrel; the first two layers
858 of RPC detectors surround the second MDT layer while the third is outside the final
859 MDT layer. The RPC system covers pseudorapidity $|\eta| < 1.05$. Each RPC consists
860 of two parallel plates at a distance of 2 mm surrounding a $\text{C}_2\text{H}_2\text{F}_4$ mixture. The
861 electric field between these plates is 4.9k kV/mm. Just as in the MDTs, an incoming
862 muon ionizes the gas, and the deposited ionization is collected by the detector (in this
863 case on the plates). It is quite fast, but with a relatively poor spatial resolution of
864 1 cm. Still, it can provide reasonable ϕ resolution due to its large distance from the
865 interaction point. This is most useful in triggering, where the timing requirements are
866 quite severe. The RPCs are also complement the MDTs by providing a measurement
867 of the non-bending coordinate.

868 Cathode Strip Chambers

869 The CSCs are used in place of MDTs in the first layer of the endcaps. This region, at
870 $2.0 < |\eta| < 2.7$, has higher particle multiplicity at the close distance to the interaction
871 point from low-energy photons and neutrons. The MDTs were not equip to deal with
872 the higher particle rate of this region, so the CSCs were designed to deal with this
873 deficiency.

874 Each CSC consists multiwire proportional chambers, oriented radially outward
875 from the interaction point. These chambers overlap partially in ϕ . The wires contain



Figure 5.13: Photo of the installation of Cathode Strip Chambers and Monitored Drift Tubes

876 a gas mixture of argon and CO₂, which is ionized when muons enter. The detectors
877 operate with a voltage of 1900 V, with much lower drift times than the MDTs. They
878 provide less hits than MDTs, but their lower drift times lower uptime and reduce the
879 amount of detector overload.

880 The CSCs are arranged into four planes on the wheels of the muon spectrometer,
881 as seen in Fig.???. There are 32 CSCs in total, with 16 on each side of the detector
882 in η .

883 **Thin Gap Chambers**

884 The TGCs serve the purpose of the RPCs in the endcap at pseudorapidity of $1.05 <$
885 $|\eta| < 2.4$; they provide fast measurements used in triggering. The TGCs are also
886 multiwire proportional chambers a la the CSCs. The fast readouts necessary for
887 trigger are provided by a high electric field and a small wire-to-wire distance of 1.8
888 mm. These detectors provide both η and ϕ information, allowing the trigger to use
889 as much information as possible when selecting events.



Figure 5.14: Photo of a muon Big Wheel, consisting of Thin Gap Chambers

890 5.5 Trigger System

891 The data rate delivered by the LHC is staggering [89]. In the 2016 dataset, the
892 collision rate was 40 MHz, meaning a *bunch spacing* of 25 ns. In each of the event,
893 as we saw in Ch.??, there are many proton-proton collisions. Most of the collisions
894 are uninteresting, such as elastic scattering of protons, or even inelastic scattering
895 leading to low-energy dijet events. These types of events have been studied in detail
896 in previous experiments.

897 Even if one is genuinely interested in these events, it's *impossible* to save all of
898 the information available in each event. If all events were written "to tape" (as the
899 jargon goes), ATLAS would store terabytes of data per second. We are limited to only
900 about 1000 Hz readout by computing processing time and storage space. We thus
901 implement a *trigger* which provides fast inspection of events to drastically reduce
902 the data rate from the 40 MHz provided by the LHC to the 1000 Hz we can write to
903 tape for further analysis.

904 The ATLAS trigger system consists of a two-level trigger, known as the Level-
905 1 trigger (L1 trigger) and the High-Level Trigger (HLT)⁴. Trigger selections are
906 organized into *trigger chains*, where events passing a particular L1 trigger are passed
907 to a corresponding HLT trigger. For example, one would require a particular high- p_T
908 muon at L1, with additional quality requirements at HLT. One can also use HLT
909 triggers as prerequisites for each other, as is done in some triggers requiring both jets
910 and E_T^{miss} .

911 **Level-1 Trigger**

912 The L1 trigger is hardware-based, and provides the very fast rejection needed to
913 quickly select events of interest. The L1 trigger uses only what is known as *prompt*
914 data to quickly identify interesting events. Only the calorimeters and the triggering
915 detectors (RPCs and TGCs) of the MS are fast enough to be considered at L1,
916 since the tracking reconstruction algorithms used by the ID and the more precise
917 MS detectors are very slow. This allows quick identification of events with the
918 most interesting physical objects : large missing transverse momentum and high-
919 p_T electrons, muons, and jets.

920 L1 trigger processing is done locally. This means that events are selected without
921 considering the entire available event. Energy deposits over some threshold are
922 reconstructed as *regions of interest*. These RoIs are then compared using pattern
923 recognition hardware to “expected” patterns for the given RoIs. Events with RoIs
924 matching these expected patterns are then handed to the HLT through the Central
925 Trigger Processor. This step alone lowers the data rate down by about three orders
926 of magnitude.

⁴In Run1, ATLAS ran with a three-level trigger system. The L1 was essentially as today; the HLT consisted of two separate systems known as the L2 trigger and the Event Filter (EF). This was changed to the simpler system used today during the shutdown between Run1 and Run2.

927 **High-Level Trigger**

928 The HLT performs the next step, taking the incoming data rate from the L1 trigger
929 of ~ 75 kHz down to the ~ 1 kHz that can be written to tape. The HLT really
930 performs much like a simplified offline reconstruction, using many common quality
931 and analysis cuts to eliminate uninteresting events. This is done by using computing
932 farms located close to the detector, which process events in parallel. Individually, each
933 event which enters the computing farms takes about 4 seconds to reconstruct; the
934 HLT reconstruction time also has a long tail, which necessitates careful monitoring
935 of the HLT to ensure smooth operation.

936 HLT triggers are targetted to a particular physics process, such as a E_T^{miss} trigger,
937 single muon trigger, or multijet trigger. The collection of all triggers is known as
938 the trigger *menu*. Since many low-energy particles are produced in collisions, it is
939 necessary to set a *trigger threshold* on the object of interest; this is really just a fancy
940 naming for a trigger p_T cut. Due to the changing luminosity conditions of the LHC,
941 these thresholds change constantly, mostly by increasing thresholds with increasing
942 instantaneous luminosity. This allows an approximately constant number of events to be
943 written for further analysis. Triggers which have rates higher than those designated
944 by the menu are *prescaled*. This means writing only some fraction of the triggered
945 events. Of course, for physics analyses, one wishes to investigate all data events
946 passing some set of analysis cuts, so often one uses the “lowest threshold unprescaled
947 trigger”. *Turn-on curves* allow one to select the needed offline analysis cut to ensure
948 the trigger is fully efficient. An example turn-on curve for the E_T^{miss} triggers used in
949 the signal region of this analysis is shown in ??.

950 The full set of the lowest threshold unprescaled triggers considered here can be
951 found in Table 5.1. These are the lowest unprescaled triggers associated to the SUSY
952 signal models and Standard Model backgrounds considered in this thesis. More
953 information can be found in [89].

Physics Object	Trigger	p_T (GeV)	Threshold	Level-1 Seed	Additional Requirements	Approximate Rate (Hz)
2015 Data						
E_T^{miss}	HLT_xe70	70	L1_XE50	-	60	
Muon	HLT_mu24_iloose_L1MU15	50	L1_MU15	isolated, loose	130	
Muon	HLT_mu50	50	L1_MU15	-	30	
Electron	HLT_e24_1hmedium_ll2base_L1EM20VH		L1_EM20VH	medium OR isolated, loose	140	
Electron	HLT_e60_1hmedium	60	L1_EM20VH	medium	10	
Electron	HLT_e120_1hloose	120	L1_EM20VH	loose	<10	
Photon	HLT_g120_loose	120	L1_EM20VH	loose	20	
2016 Data						
E_T^{miss}	HLT_xe100_mht_L1XE5000		L1_XE50	-	180	
Muon	HLT_mu24_ivarmedium4	50	L1_MU20	medium	120	
Muon	HLT_mu50	50	L1_MU20	-	40	
Electron	HLT_e24_1htight_noD1ivarloose		L1_EM22VHI	tight with no d_0 or loose	110	
Electron	HLT_e60_1hmedium_nd60		L1_EM22VHI	medium with no d_0	10	
Electron	HLT_e140_1hloose_noD0		L1_EM22VHI	loose with no d_0	<10	
Photon	HLT_g140_loose	140	L1_EM22VHI	loose	20	

Table 5.1: High-Level Triggers used in this thesis. Descriptions of loose, medium, tight, and isolated can be found in [89]. The d_0 cut refers to a quality cut on the vertex position; this was removed from many triggers in 2016 to increase sensitivity to displaced vertex signals. For most triggers, the increased thresholds in 2016 compared to 2016 were designed to keep the rate approximately equal. The exception is the E_T^{miss} triggers; see 5.5.

954 **Razor Triggers**

955 For the analysis presented in this thesis, the *razor triggers* were developed. These are
956 topological triggers, combining both jet and E_T^{miss} information to select interesting
957 events. In particular, they use the razor variable M_{Δ}^R which will be described in
958 Chapter ??.

959 Based on 2015 run conditions, these triggers would have allowed the use of a lower
960 offline E_T^{miss} cut with a similar rate to the nominal E_T^{miss} triggers. This can be seen
961 in the turn-on curves shown in Figure 5.15. The razor triggers are fully efficient at
962 nearly 100 GeV lower than the corresponding E_T^{miss} triggers in M_{Δ}^R .

963 There was a quite big change in the 2016 menu, which increased the rate given to
964 E_T^{miss} triggers drastically. This can be seen in the difference in rate shown between
965 E_T^{miss} triggers in 2015 and 2016 in Table 5.1. This allowed the E_T^{miss} triggers to
966 maintain a lower threshold throughout the dataset used in this thesis.

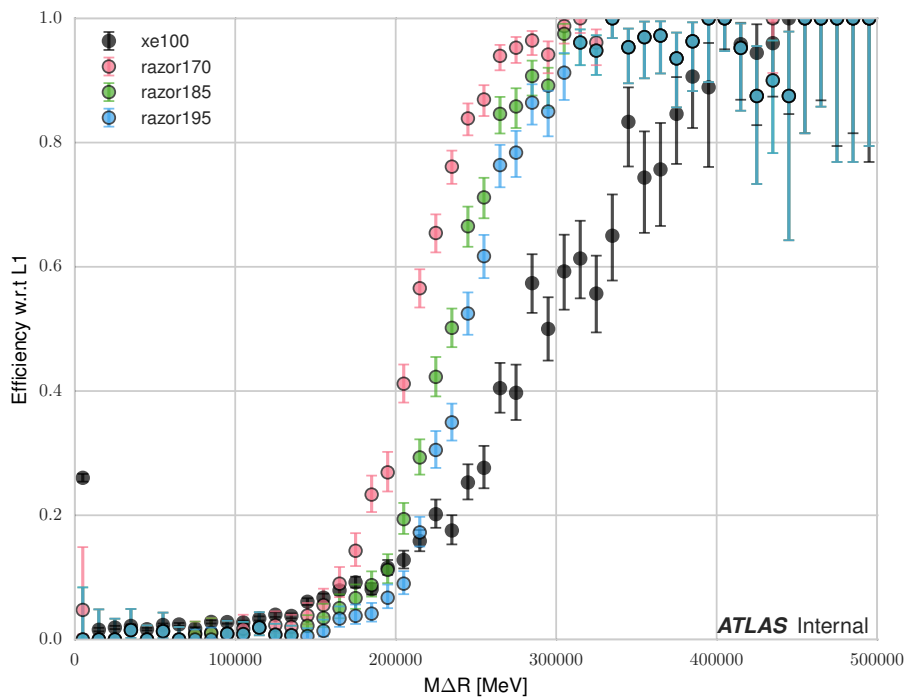
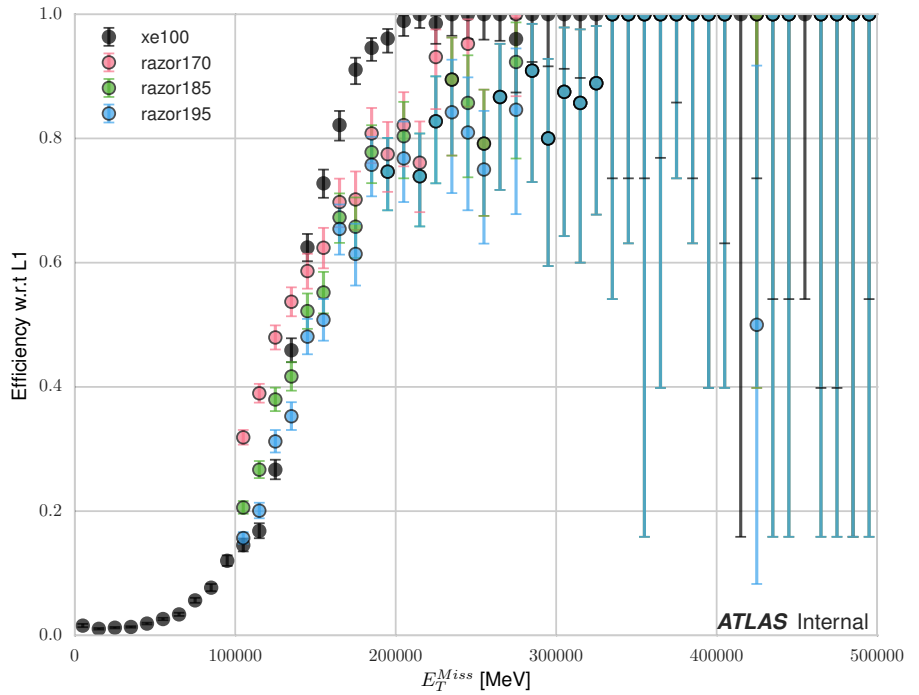


Figure 5.15: Turn-on curves for the razor triggers and nominal E_T^{miss} trigger. The razor triggers show a much sharper turn-on in M_{Δ}^R relative to the E_T^{miss} trigger. The converse is true for the E_T^{miss} triggers.

Object Reconstruction

969 This chapter describes the reconstruction algorithms used within ATLAS. We will
970 make the distinction between the “primitive” objects which are reconstructed from
971 the detector signals from the “composite” physics objects we use in measurements
972 and searches for new physics.

973 6.1 Primitive Object Reconstruction

974 The primitive objects reconstructed by ATLAS are *tracks* and (calorimeter) *clusters*.
975 These are reconstructed directly from tracking hits and calorimeter energy deposits
976 into cells. Tracks can be further divided into inner detector and muon spectrom-
977 eter tracks. Calorimeter clusters can be divided into sliding-window clusters and
978 topological clusters (topoclusters).

979 Inner Detector Tracks

980 Inner detector tracks are reconstructed from hits in the inner detector [90, 91] These
981 hits indicate that a charged particle has passed through the detector material. Due
982 to the 2 T solenoid in the inner detector, the hits associated with any individual
983 particle will be curved. The amount of curvature determines the momentum of the
984 particle. In any given event, there are upwards of 10^4 hits, making it impossible to do
985 any sort of combinatorics to reconstruct tracks. There are two algorithms used by
986 ATLAS track reconstruction, known as *inside-out* and *outside-in*.

987 ATLAS first employs the inside-out algorithm. One assumes the track begins
988 at the interaction point. Moving out from the interaction point, one creates track
989 seeds. Track seeds are proto-tracks constructed from three hits. These hits can be
990 distributed as three pixel hits, two pixel hits and one SCT hit, or three SCT hits.
991 One extrapolates the track and uses a combinatorial Kalman filter[90], which adds
992 the rest of the pixel and SCT hits to the seeds. This is done seed by seed, so it
993 avoids the combinatorial complexity involved with checking all hits with all seeds.
994 At this point, the algorithm applies an additional filter to avoid ambiguities from
995 nearby tracks. The TRT hits are added to the seeds using the same method. After
996 this procedure, all hits are associated to a track.

997 The next step is to figure out the correct kinematics of the track. This is
998 done by applying a fitting algorithm which outputs the best-fit track parameters
999 by minimizing the track distance from hits, weighted by each hit's resolution. These
1000 parameters are $(d_0, z_0, \eta, \phi, q/p)$ where d_0 (z_0) is the transverse (longitudinal) impact
1001 parameter and q/p is the charge over the track momenta. This set of parameters
1002 uniquely defines the measurement of the trajectory of the charged particle associated
1003 to the track. An illustration of a track with these parameters is shown in Fig.6.1.

1004 The other track reconstruction algorithm is the outside-in algorithm. As the
1005 name implies, we start from the outside of the inner detector, in the TRT, and
1006 extend the tracks in toward the interaction point. One begins by seeding from
1007 TRT hits, and extending the track back towards the center of the detector. The
1008 same fitting procedure is used as in the inside-out algorithm to find the optimal
1009 track parameters. This algorithm is particularly important for finding tracks which
1010 originate from interactions with the detector material, especially the SCT. For tracks
1011 from primary vertices, this often finds the same tracks as the inside-out algorithm,
1012 providing an important check on the consistency of the tracking procedure.

1013 In the high luminosity environment of the LHC, even the tracks reconstructed

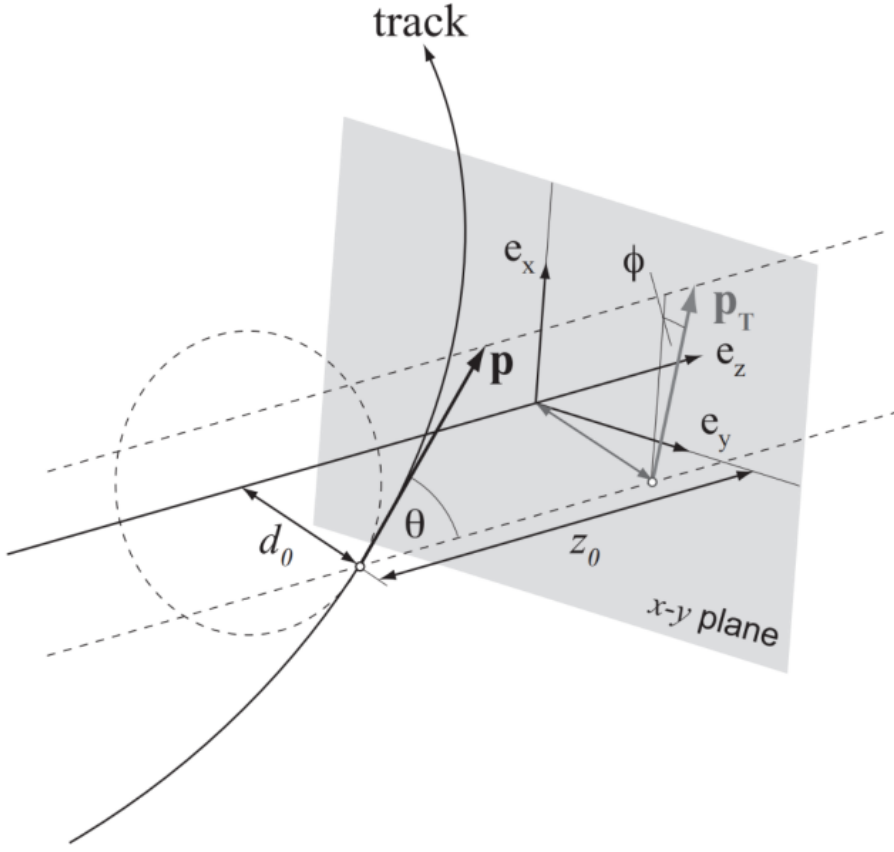


Figure 6.1: The parameters associated to a track.

from precision detectors such as those of ATLAS inner detector can sometimes lead to fake tracks from simple combinatoric chance. Several quality checks are imposed after track fitting which reduce this background. Seven silicon (pixel + SCT) hits are required for all tracks. No more than two *holes* are allowed in the pixel detector. Holes are expected measurements from the track that are missing in the pixel detector. Finally, tracks with poor fit quality, as measured by χ^2/ndf , are also rejected. Due to the high quality of the silicon measurements in the pixel detector and SCT, these requirements give good track reconstruction efficiency, as seen in Fig.6.2 for simulated events[92].



(a) Track reconstruction as a function of p_T . (b) Track reconstruction as a function of η .

Figure 6.2: Track reconstruction efficiency as a function of track p_T and η . The efficiency is defined as the number of reconstructed tracks divided by the number of generate charged particles.

1023 Sliding-window clusters

1024 The sliding-window algorithm is a way to combine calorimeter cells into composite
 1025 objects (clusters) to be used as inputs for other algorithms[93]. Sliding-window
 1026 clusters are the primary inputs to electron and photon reconstruction, as described
 1027 below. The electromagnetic calorimeter has high granularity, with a cell size of
 1028 $(\eta, \phi) = (.025, .025)$ in the coarsest second layer throughout most of the calorimeter.
 1029 The “window” consists of 3 by 5 cells in the (η, ϕ) space. All layers are added on
 1030 this same 2D space. One translates this window over the space and seeds a cluster
 1031 whenever the energy sum of the cells is maximized. If the seed energy is greater
 1032 than 2.5 GeV, this seed is called a sliding-window cluster. This choice was motivated
 1033 to optimize the reconstruction efficiency of proto-electrons and proto-photons while
 1034 rejecting fakes from electronic noise and additional particles from pileup vertices.

1035 Topological clusters

1036 Topoclusters are the output of the algorithm used within ATLAS to combine
1037 hadronic and electromagnetic calorimeter cells in a way which extracts signal from
1038 a background of significant electronic noise[94]. They are the primary input to the
1039 algorithms which reconstruct jets.

1040 Topological clusters are reconstructed from calorimeter cells in the following way.
1041 First, one maps all cells onto a single $\eta - \phi$ plane so one can speak of *neighboring*
1042 cells. Two cells are considered neighboring if they are in the same layer and directly
1043 adjacent, or if they are in adjacent layers and overlap in $\eta - \phi$ space. The *significance*
1044 ξ_{cell} of a cell during a given event is

$$\xi_{\text{cell}} = \frac{E_{\text{cell}}}{\sigma_{\text{noise},\text{cell}}} \quad (6.1)$$

1045 where $\sigma_{\text{noise},\text{cell}}$ is measured for each cell in ATLAS and E_{cell} measures the current
1046 energy level of the cell. One thinks of this as the measurement of the energy *over*
1047 *threshold* for the cell.

1048 Topocluster *seeds* are defined as calorimeter cells which have a significance $\xi_{\text{cell}} >$
1049 4. These are the inputs to the algorithm. One iteratively tests all cells adjacent
1050 to these seeds for $\xi_{\text{cell}} > 2$. Each cells passing this selection is then added to the
1051 topocluster, and the procedure is repeated. When the algorithm reaches the point
1052 where there are no additional adjacent cells with $\xi_{\text{cell}} > 2$, every positive-energy cell
1053 adjacent to the current proto-cluster is added. The collection of summed cells is a
1054 topocluster. An example of this procedure for a simulation dijet event is shown in
1055 Fig.6.3.

1056 There are two calibrations used for clusters[95]. These are known as the
1057 electromagnetic (EM) scale and the local cluster weighting (LCW) scale. The EM
1058 scale is the energy read directly out of the calorimeters as described. This scale
1059 is appropriate for electromagnetic processes. The LCW scale applies additional



Figure 6.3: Example of topoclustering on a simulated dijet event.

1060 scaling to the clusters based on the shower development. The cluster energy can be
1061 corrected for calorimeter non-compensation and the differences in the hadronic and
1062 electromagnetic calorimeters’ responses. This scale provides additional corrections
1063 that improve the accuracy of hadronic energy measurements. This thesis only uses
1064 the EM scale corrections. LCW scaling requires additional measurements that only
1065 became available with additional data. Due to the jet calibration procedure that
1066 we will describe below, it is also a relatively complicated procedure to rederive the
1067 “correct” jet energy.

1068 Muon Spectrometer Tracks

1069 Muon spectrometer tracks are fit using the same algorithms as the ID tracks, but
1070 different subdetectors. The tracks are seeded by hits in the MDTs or CSCs. After
1071 seeding in the MDTs and CSCs, the hits from all subsystems are refit as the final
1072 MS track. These tracks are used as inputs to the muon reconstruction, as we will see
1073 below.

1074 6.2 Physics Object Reconstruction and Quality

1075 Identification

1076 There are essentially six objects used in ATLAS searches for new physics: electrons,
1077 photons, muons, τ -jets, jets, and E_T^{miss} . The reconstruction of these objects is
1078 described here. In this thesis, τ lepton jets are not treated differently from other
1079 hadronic jets, and we will not consider their reconstruction algorithms. A very
1080 convenient summary plot is shown in Fig.6.4.

1081 One often wishes to understand “how certain” we are that a particular object
1082 is truly the underlying physics object. In ATLAS, we often generically consider, in



Figure 6.4: The interactions of particles with the ATLAS detector. Solid lines indicate the particle is interacting with the detector, while dashed lines are shown where the particle does not interact.

1083 order, *very loose*, *loose*, *medium*, and *tight* objects¹. These are ordered in terms of
 1084 decreasing object efficiency, or equivalently, decreasing numbers of fake objects. We
 1085 will also describe briefly the classification of objects into these categories.

1086 In this thesis, since we present a search for new physics in a zero lepton final state,
 1087 we will provide additional details about jet and E_T^{miss} reconstruction.

¹ These are not all used for all objects, but it's conceptually useful to think of these different categories.

1088 **Electrons and Photons**

1089 **Reconstruction**

1090 The reconstruction of electrons and photons (often for brevity called “electromagnetic
1091 objects”) is very similar [93, 96, 97]. This is because the reconstruction begins with
1092 the energy deposit in the calorimeter in the form of an electromagnetic shower. For
1093 any incoming e/γ , this induces many more electrons and photons in the shower. The
1094 measurement in the calorimeter is similar for these two objects.

1095 One begins the reconstruction of electromagnetic objects from the sliding-window
1096 clusters reconstructed from the EM calorimeter. These $E > 2.5$ GeV clusters the
1097 the primary seed for electrons and photons. One then looks for all ID tracks within
1098 $\Delta R < 0.3$, where $\Delta R = \sqrt{\Delta\eta^2 + \Delta\phi^2}$. We “match” the track and cluster if they are
1099 within $\Delta\phi < 0.2$ in the direction of track curvature, or $\Delta\phi < 0.05$ in the direction
1100 opposite the track curvature. Those track-cluster seeds with tracks pointing to the
1101 primary vertex are reconstructed as electrons.

1102 For photons, we have two options to consider, known as *converted* and *unconverted*
1103 photons. Due to the high energy of the LHC collisions, typical photons have energy
1104 $>\sim 1$ GeV. At this scale, photons interact almost exclusively via pair-production in
1105 the presence of the detector material, as shown in Fig.6.5 [56]. If the track-cluster seed
1106 has a track which does not point at the primary vertex, we reconstruct this object as a
1107 converted photon. This happens since the photon travels a distance before decay into
1108 two electrons, and see the tracks coming from this secondary vertex. Those clusters
1109 which do not have any associated tracks are then reconstruced as an unconverted
1110 photon.

1111 The final step in electromagnetic object reconstruction is the final energy value
1112 assigned to these objects. This process is different between electrons and photons due
1113 to their differing signatures in the EM calorimeter. In the barrel, electrons energies

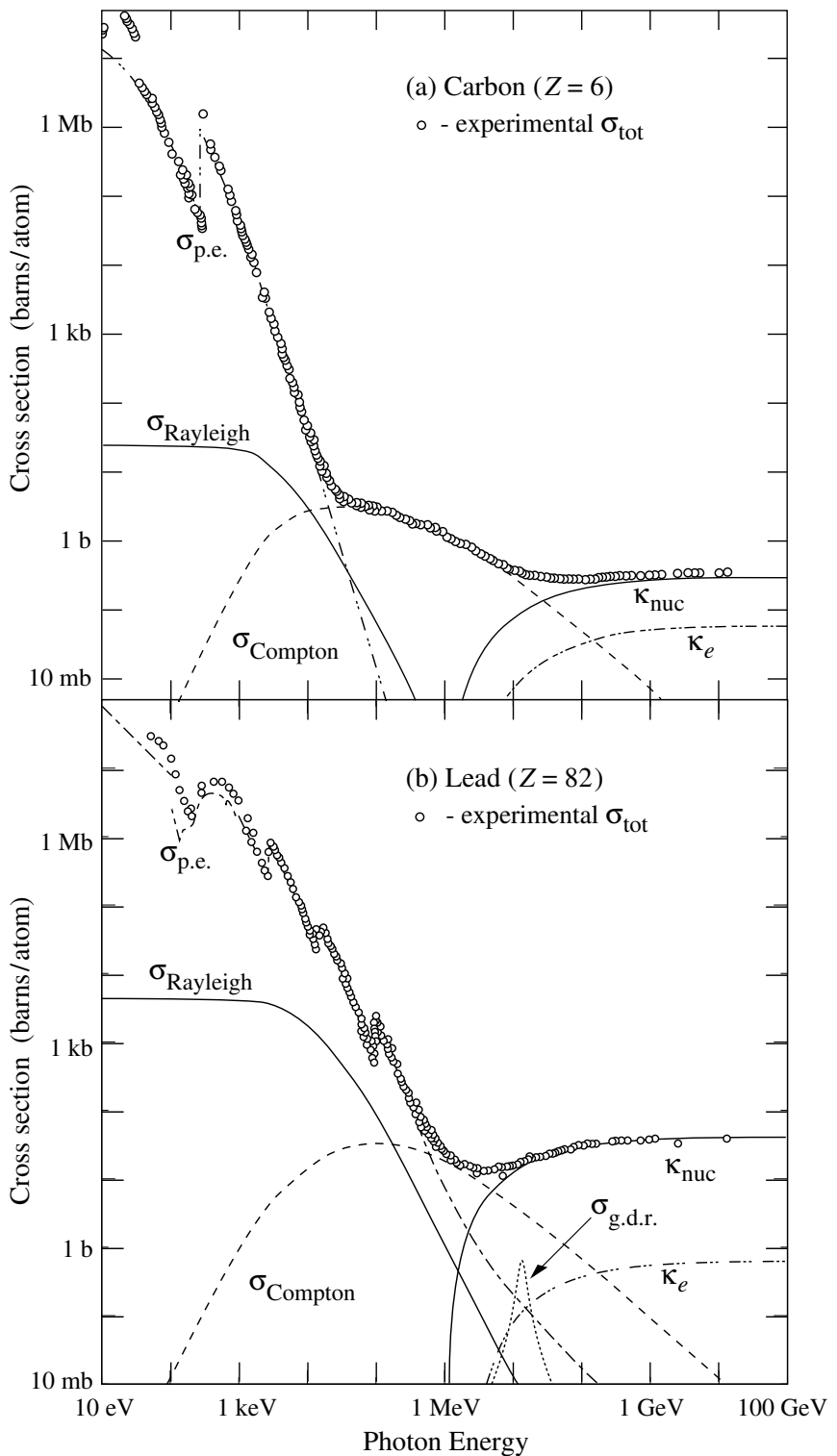


Figure 6.5: Photon total cross sections as a function of energy in carbon and lead, showing the contributions of different processes[56].

1114 are assigned as the sum of the 3 clusters in η and 7 clusters in ϕ to account for the
1115 electron curving in the ϕ direction. Barrel photons are assigned the energy sum of
1116 (3, 5) clusters in (η, ϕ) space. In the endcap, the effect of the magnetic field on the
1117 electrons is smaller, and there is a coarser granularity. Both objects sum the (5, 5)
1118 clusters for their final energy value.

1119 Quality Identification

1120 Electrons have a number of important backgrounds which can give fakes. Fake
1121 electrons come primarily from secondary vertices in hadron decays or misidentified
1122 hadronic jets. To reduce these backgrounds, quality requirements are imposed on
1123 electron candidates. Loose electrons have requirements imposed on the shower
1124 shapes in the electromagnetic calorimeter and on the quality of the associated ID
1125 track. There is also a requirement that there is a small energy deposition in the
1126 hadronic calorimeter behind the electron, to avoid jets being misidentified as electrons
1127 (low hadronic leakage). Medium and tight electrons have increasingly stronger
1128 requirements on these variables, and additional requirements on the isolation (as
1129 measured by ΔR) and matching of the ID track momentum and the calorimeter
1130 energy deposit.

1131 Photons are relatively straightforward to measure, since there are few background
1132 processes[98]. The primary one is pion decays to two photons, which can cause a jet
1133 to be misidentified as photon. Loose photons have requirements on the shower shape
1134 and hadronic leakage. Tight photons have tighter shower shape cuts, especially on
1135 the high granularity first layer of the EM calorimeter. The efficiency for unconverted
1136 tight photons as a function of p_T is shown in

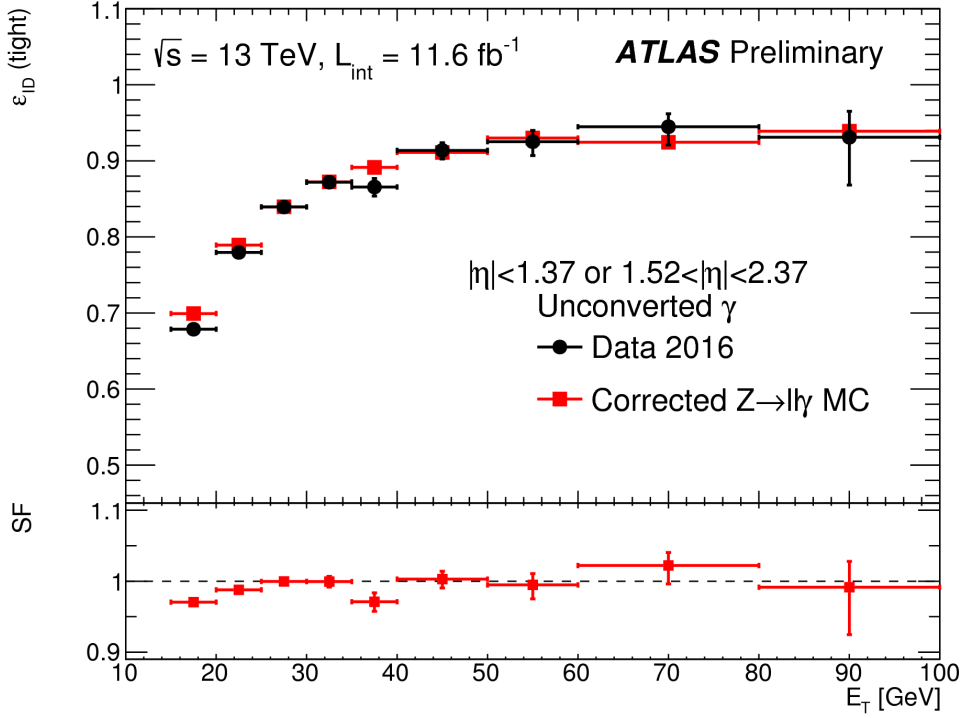


Figure 6.6: Unconverted photon efficiency as measured in [98].

1137 Muons

1138 Reconstruction

1139 Muons are reconstructed using measurements from all levels of the ATLAS detec-
 1140 tor[99]. They leave a ID track, a small, characteristic deposition in the EM calorime-
 1141 ter, and then a track in the muon spectrometer. The primary reconstruction technique
 1142 produces a so-called *combined* muon. “Combined” means using a combination of the
 1143 ID and MS tracks to produce the final reconstructed muon kinematics. This is done
 1144 by refitting the hits associated to both tracks, and using this refit track for the muon
 1145 kinematics. This process produces the best measured muons, although several other
 1146 worse algorithms are used when the full detector information is missing. An example
 1147 is in the region $2.5 < |\eta| < 2.7$ outside the ID acceptance, where MS tracks are used
 1148 without the corresponding ID tracks.

1149 **Quality Identification**

Several additional criteria are used to assure muon measurements are free of significant background contributions, especially from pion and kaon decays to muons. Muons produced via these decay processes are often characterized by a “kink”. Candidate muons with a poor fit quality, characterized by $\chi^2/\text{n.d.f.}$, are thus rejected. Additionally, the absolute difference in momentum measurements between the ID and MS provide another handle, since the other decay products from hadron decays carry away some amount of the initial hadron momentum. This is measured by

$$\rho' = \frac{|p_T^{\text{ID}} - p_T^{\text{MS}}|}{p_T^{\text{Combined}}}. \quad (6.2)$$

Additionally, there is a requirement on the q/p significance, defined as

$$S_{q/p} = \frac{|(q/p)^{\text{ID}} - (q/p)^{\text{MS}}|}{\sqrt{\sigma_{\text{ID}}^2 + \sigma_{\text{MS}}^2}}. \quad (6.3)$$

1150 The $\sigma_{\text{ID,MS}}$ in the denominator of Eq.6.3 are the uncertainties on the corresponding
1151 quantity from the numerator. Finally, cuts are placed on the number of hits in the
1152 various detector elements.

1153 Subsequently tighter cuts on these variables allow one to define the different muon
1154 identification criteria. Loose muons have the highest reconstruction efficiency, but
1155 the highest number of fake muons, since there are no requirements on the number
1156 of subdetector hits and the loosest requirements on the suite of quality variables.
1157 Medium muons consist of Loose muons with tighter cuts on the quality variables.
1158 They also require more than three MDT hits in at least two MDT layers. These are
1159 the default used by ATLAS analyses. Tight muons have stronger cuts than those of
1160 the medium selection, and reducing the reconstruction efficiency. The reconstruction
1161 efficiency as a function of p_T can be seen for Medium muons in Fig.6.7.

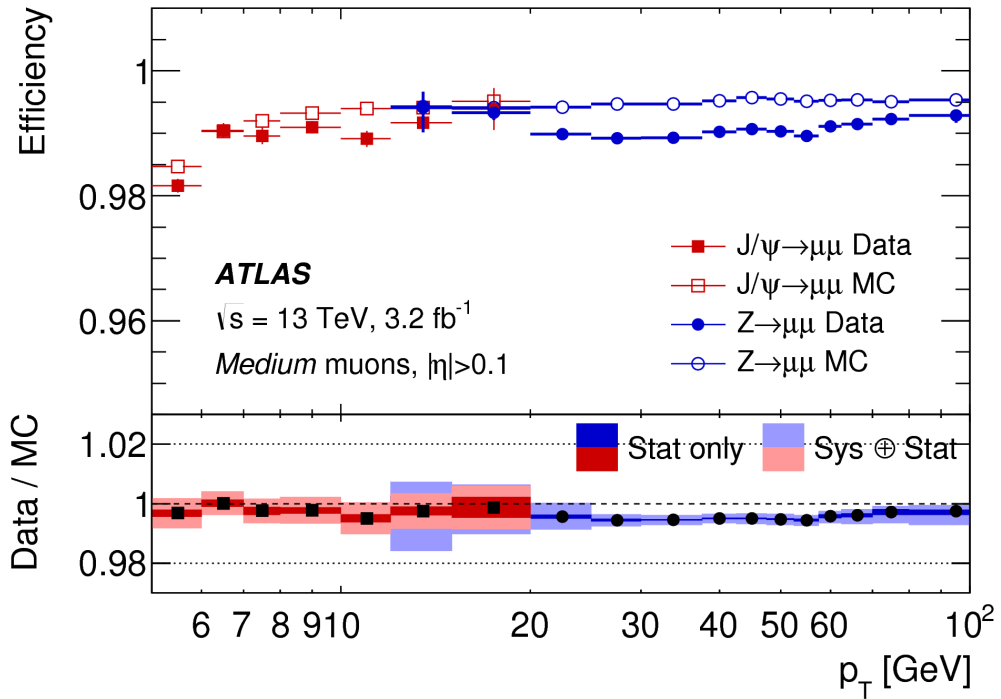


Figure 6.7: Medium muon efficiency as measured in [99].

1162 Jets

1163 Jets are composite objects corresponding to many physical particles [56, 100, 101]
 1164 This is a striking difference from the earlier particles. Fortunately, we normally (and
 1165 in this thesis) care about the original particle produced in primary collision. In the
 1166 SM, this corresponds to quarks and gluons. Due to the hadronization process, free
 1167 quarks and gluons spontaneously hadronize and produce a hadronic shower, which
 1168 we call a jet. These showers can be measured by the EM and hadronic calorimeters,
 1169 and the charged portions can be measured in the ID. The first question is how to
 1170 combine these measurements into a composite object representing the underlying
 1171 physical parton. This is done via jet algorithms.

1172 **Jet Algorithms**

1173 It might seem straightforward to combine the underlying physical particles into a
1174 jet. There are three important characteristics required for any jet reconstruction
1175 algorithm to be used by ATLAS.

- 1176 • Collinear safety - if any particle with four-vector p is replaced by two particles
1177 of p_1, p_2 with $p = p_1 + p_2$, the subsequent jet should not change

1178 • Radiative (infrared) safety - if any particle with four-vector p radiates a particle
1179 of energy $\alpha \rightarrow 0$, the subsequent jet should not change

1180 • Fast - the jet algorithm should be “fast enough” to be useable by ATLAS
1181 computing resources

1182 The first two requirements can be seen in terms of requirements on soft gluon emission.
1183 Since partons emit arbitrarily soft gluons freely, one should expect the algorithms
1184 to not be affected by this emission. The final requirement is of course a practical
1185 limitation.

The algorithms in use by ATLAS (and CMS) which satisfies these requirements are collectively known as the k_T algorithms [102–104]. These algorithms iteratively combine the “closest” objects, defined using the following distance measures :

$$d_{ij} = \min(k_{T,i}^{2p}, k_{T,j}^{2p}) \frac{\Delta_{ij}^2}{R^2} \quad (6.4)$$
$$d_{iB} = k_{Ti}^{2p}$$

1186 In Eq.6.4, k_T, i is the transverse momentum of i -th jet *constituent*, Δ_{ij} is the angular
1187 distance between the constituents. Both R and p are adjustable parameters: R is
1188 known as the (jet) *cone size* and p regulates the power of the energy versus the
1189 geometrical scales. The algorithm sequence, for a given set of objects i with four-
1190 vector k :

- 1191 1. Find the minimum distance in the set of all d_{ij} and d_{iB} .

1192 2. If the distance is one of the d_{ij} , combine the input pair of object i, j and return
1193 to (1). If the distance is one of the d_{iB} , remove the object from the list, call it
1194 a jet, and return to (1).

1195 This process ends when all objects i have been added to a jet.

1196 Any choice of (p, R) has the requirements of collinear and radiative safety. In
1197 essence, the choice is then to optimize based on speed and the potential for new
1198 physics discoveries. In ATLAS, we make the choice of $p = -1$ which is also known
1199 as the *anti- k_T* algorithm. The choice of $R = 0.4$ is used for the distance parameter of
1200 the jets.

1201 The primary “nice” quality of this algorithm can be seen with the following
1202 example. Consider three inputs to an anti- k_T algorithm, all with $\eta = 0$:

1203 • Object 1 : $(p_T, \phi) = (30 \text{ GeV}, 0)$

1204 • Object 2 : $(p_T, \phi) = (20 \text{ GeV}, -0.2)$

1205 • Object 3 : $(p_T, \phi) = (10 \text{ GeV}, 0.2)$

1206 • Object 4 : $(p_T, \phi) = (1 \text{ GeV}, 0.5)$

1207 . In the case shown, it seems natural to first combine the “bigger” objects 1 and 2.
1208 These then pick up the extra small object 3, and object 4 is not included in the jet.
1209 This is exactly what is done by the anti- k_T algorithm. The (normal) k_T algorithm with
1210 $p = 1$ instead combines the smallest objects, 3 and 4, first. Object 1 and 2 combine
1211 to form their own jet, instead of these jets picking up object 3. This behavior is not
1212 ideal due to the effects of pileup, as we will see in the next section.

1213 **Jet Reconstruction**

1214 In ATLAS, jets are reconstructed using multiple different objects as inputs, including
1215 tracks, “truth” objects, calorimeter clusters, and *particle flow objects* (PFOs). For

1216 physics analyses, ATLAS primarily uses jets reconstructed from calorimeter clusters,
1217 but we will describe the others here, as they are often used for derivations of
1218 systematic uncertainties or future prospects.

1219 Calorimeter jets are reconstructed using topoclusters using the anti- k_T algorithm
1220 with $R = 0.4$. The jet reconstruction algorithm is run on the collection of all
1221 topoclusters reconstructed as in Sec.6.1. Both EM and LCW scale clusters are used
1222 in the ATLAS reconstruction software and produce two sets of jets for analysis. As
1223 stated above, this thesis presents an analysis using jets reconstructed using EM scale
1224 clusters, which we refer to these as *EM jets*.

1225 Tracks can be used as inputs to jet reconstruction algorithms. Jets reconstructed
1226 from tracks are known as *track jets*. Since the ID tracks do not measure neutral
1227 objects, these jets measure an incorrect energy. However, these are still useful for
1228 checks and derivations of systematic uncertainties.

1229 *Truth* jets are reconstructed from *truth* particles. In this case, truth is jargon for
1230 simulation. In simulation, the actual simulated particles are available and used as
1231 inputs to the jet reconstruction algorithms. Similarly to track jets, these are not useful
1232 in and of themselves. Instead, truth jets are used for comparisons and derivations of
1233 systematic uncertainties.

1234 The last object used as inputs to jet reconstruction algorithms are *particle flow*
1235 *objects* (PFOs). These are used extensively as the primary input to jet particle
1236 reconstruction algorithms by the CMS collaboration[105]. Particle flow objects are
1237 reconstructed by associating tracks and clusters through a combination of angular
1238 distance measures and detector response measurements to create a composite object
1239 which contains information from both the ID and the calorimeters. For calorimeter
1240 clusters which do not have any associated ID track, the cluster is simply the PFO.
1241 The natural association between tracks and clusters provides easy pileup subtraction
1242 since tracks are easily associated to the primary vertex. This technique is generally

1243 used in CMS, and ATLAS has been slow to adopt the same. As pileup has increased,
1244 the utility of using PFOs as inputs to jet reconstruction has increased as well.

1245 **Jet Calibration**

1246 Jets as described in the last section are still *uncalibrated*. Even correcting the cluster
1247 energies using the LCW does not fully correct the jet energy, due to particles losing
1248 energy in the calorimeters. The solution to this is the *jet energy scale* (JES). The
1249 JES is a series of calibrations which on average restore the correct truth jet energy
1250 for a given reconstructed jet. These steps are shown in Fig.6.8 and described here.

1251 The first step is the origin correction. This adjusts the jet to point at the
1252 primary vertex. Next, is the jet-area based pileup correction. This step subtracts
1253 the “average” pileup as measured by the energy density ρ outside of the jets and
1254 assumes this is a good approximation for the pileup inside the jet. One then removes
1255 energy $\Delta E = \rho \times A_{\text{jet}}$ in this step. The residual pileup correction makes a final offset
1256 correction by parametrizing the change in jet energy as a function of the number of
1257 primary vertices N_{PV} and the average number of interactions μ .

1258 The next step is the most important single correction, known as the AbsoluteEta-
1259 JES step. Due to the use of non-compensation and sampling calorimeters in ATLAS,
1260 the measured energy of a jet is a fraction of the true energy of the outgoing parton.
1261 Additionally, due to the use of different technologies and calorimeters throughout the
1262 detector, there are directional biases induced by these effects. The correction bins a
1263 multiplicative factor in p_{T} and η which scales the reconstructed jets to corresponding
1264 truth jet p_{T} . This step does not entirely correct the jets, since it is entirely a
1265 simulation-based approach.

1266 The final steps are known as the global sequential calibration (GSC) and the
1267 residual in-situ calibration. The GSC uses information about the jet showering shape
1268 to apply additional corrections based on the expected shape of gluon or quark jets.

1269 The final step is the residual in-situ calibration, which is only applied to data. This
1270 step uses well-measured objects recoiling off a jet to provide a final correction to the
1271 jets in data. In the low p_T region ($20 \text{ GeV} \sim < p_{T,\text{jet}} \sim < 200 \text{ GeV}$), $Z \rightarrow ll$ events are
1272 used as a reference object. In the middle p_T region ($100 \text{ GeV} \sim < p_{T,\text{jet}} \sim < 600 \text{ GeV}$),
1273 the reference object is a photon, while in the high p_T region ($p_{T,\text{jet}} \sim > 200 \text{ GeV}$),
1274 the high p_T jet is compared to multiple smaller p_T jets. The reference object is this
1275 group of multijets. After this final correction, the data and MC scales are identical
1276 up to the corresponding uncertainties. The combined JES uncertainty as a function
1277 of p_T is shown in Fig.6.9.

1278 Jet Vertex Tagger

1279 The *jet vertex tagger* (JVT) technique is used to separate pileup jets from those
1280 associated to the hard primary vertex[106]. The technique for doing so first involves
1281 *ghost association*[107]. Ghost association runs the anti- k_T jet clustering algorithm on
1282 a combined collection of the topoclusters and tracks. The tracks *only* momenta are
1283 set to zero², with only the directional information is included. As discussed above,
1284 the anti- k_T algorithm is “big to small”; tracks are associated to the “biggest” jet near
1285 them in (η, ϕ) . This method uniquely associates each track to a jet, without changing
1286 the final jet kinematics.

1287 The JVT technique uses a combination of these track variables to determine the
1288 likelihood that the jet originated at the primary vertex. For jets which have associated
1289 tracks from ghost association, this value ranges from 0 (likely pileup jet) to 1 (likely
1290 hard scatter jet). Jets without associated tracks are assigned $\text{JVT} = -.1$. The
1291 working point of $\text{JVT} > .59$ is used for jets in this thesis.

²Well, not exactly zero, since zero momentum tracks wouldn’t have a well-defined (η, ϕ) coordinate, but set to a value obeying $p_{T,\text{track}} << 400 \text{ MeV} = p_{\text{track,min}}$. This is the minimum momentum for a track to reach the ATLAS inner detector.

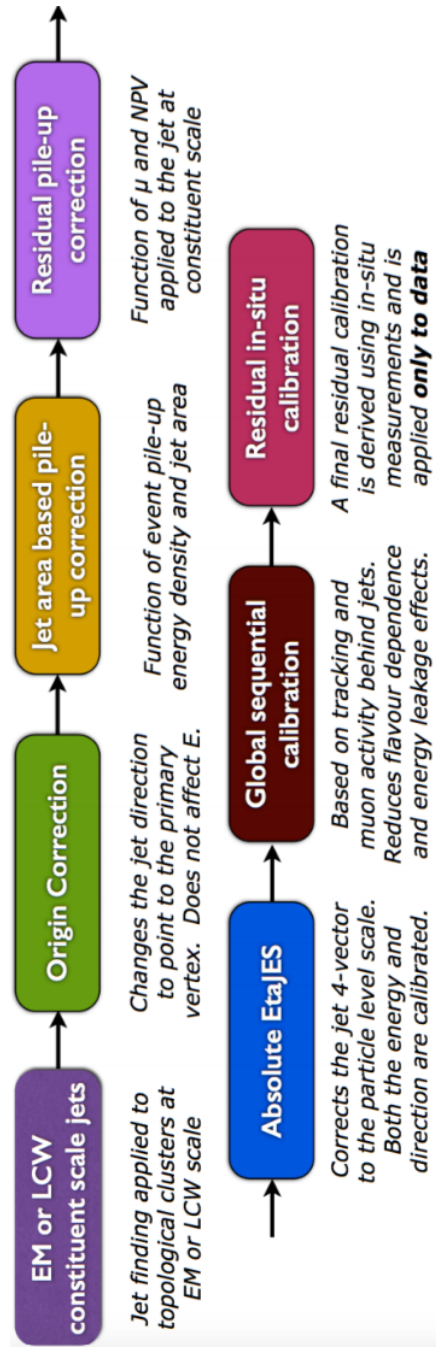


Figure 6.8: The steps used by ATLAS to calibrate jets

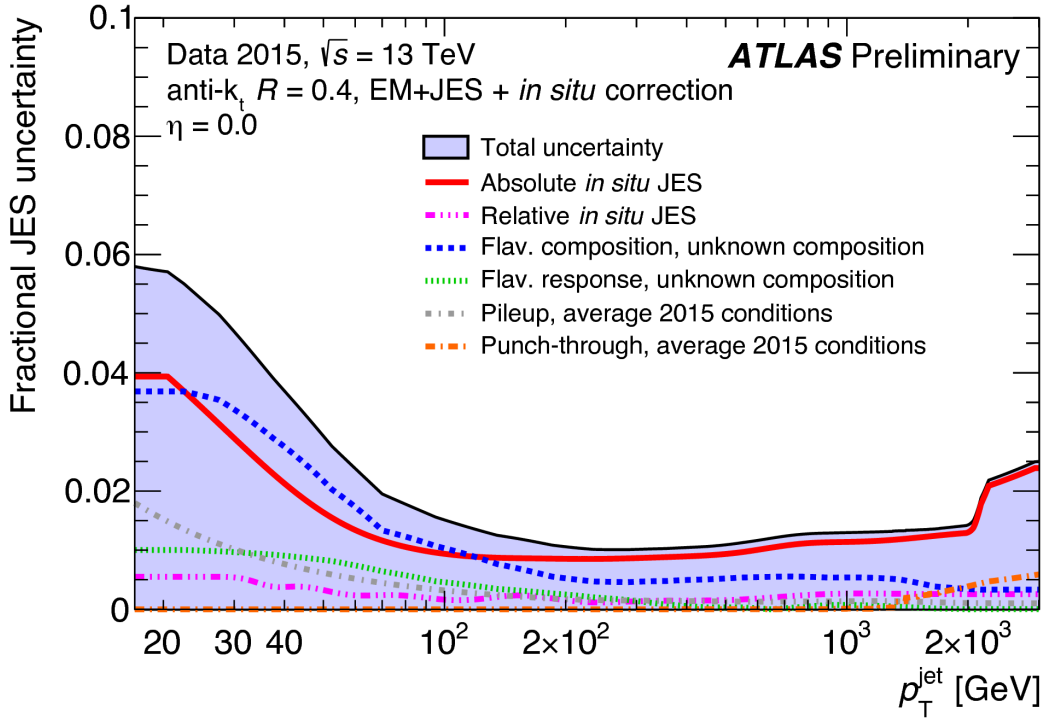


Figure 6.9: Combined jet energy scale uncertainty as a function of p_T at $\eta = 0$.

1292 B-jets

1293 Jets originating from bottom quarks (b-jets) are interesting physical phenomena that
 1294 can be *tagged* by the ATLAS detector[Aad:2015ydr, 108]. B-hadrons, which have
 1295 a comparatively long lifetime compared to hadrons consisting of lighter quarks, can
 1296 travel a macroscopic distance inside the ATLAS detector. The high-precision tracking
 1297 detectors identify the secondary vertices from these decays and the jet matched to
 1298 that vertex is called a *b-jet*. The “MV2c10” algorithm, based on boosted decision
 1299 trees, identifies these jets using a combination of variables sensitive to the difference
 1300 between light-quark and b-quark jets. The efficiency of this tagger is 77%, with a
 1301 rejection factor of 134 for light-quarks and 6 for charm jets.

1302 **Missing Transverse Momentum**

1303 Missing transverse momentum E_T^{miss} [109] is a key observable in searches for new
1304 physics, especially in SUSY searches[110, 111]. However, E_T^{miss} is not a uniquely
1305 defined object when considered from the detector perspective (as compared to the
1306 Feynammn diagram), and it is useful to understand the choices that affect the
1307 performance of this observable in searches for new physics.

1308 **E_T^{miss} Definitions**

Hard objects refers to all physical objects as defined in the previous sections. The
 E_T^{miss} reconstruction procedure uses these hard objects and the *soft term* to provide
a value and direction of the missing transverse momentum. The $E_{x(y)}^{\text{miss}}$ components
are calculated as:

$$E_{x(y)}^{\text{miss}} = E_{x(y)}^{\text{miss, } e} + E_{x(y)}^{\text{miss, } \gamma} + E_{x(y)}^{\text{miss, jets}} + E_{x(y)}^{\text{miss, } \mu} + E_{x(y)}^{\text{miss, soft}}, \quad (6.5)$$

1309 where each value $E_{x(y)}^{\text{miss, } i}$ is the negative vectorial sum of the calibrated objects defined
1310 in the previous sections.

1311 For purposes of E_T^{miss} reconstruction, we must assign an ordering of *overlap*
1312 *removal*. This is to avoid double counting of the underlying primitive objects (clusters
1313 and tracks) which are inputs to the reconstruction of the physics objects. We resolve
1314 this in the following order : electrons, photons , jets and muons. This is motivated
1315 by the performance of the reconstruction of these objects in the calorimeters.

1316 The soft term $E_{x(y)}^{\text{miss, soft}}$ contains all of the primitive objects which are not
1317 associated to any of the reconstructed physics objects. Of course, we need to choose
1318 which primitive object to use. The primary choices which have been used within
1319 ATLAS are the *calorimeter-based soft term* (CST) and the *track-based soft term*
1320 (TST). Based on the soft term choice, we then call E_T^{miss} built with a CST (TST)

1321 soft term simply CST (TST) E_T^{miss} . An additional option, which will be important
1322 as pileup continues to increase, particle flow E_T^{miss} (PFlow E_T^{miss}).

1323 The CST E_T^{miss} was used for much of the early ATLAS data-taking. CST E_T^{miss} is
1324 built from the calibrated hard objects, combined with the calorimeter clusters which
1325 are *not* assigned to any of those hard objects. In the absence of pileup, it provides the
1326 best answer for the “true” E_T^{miss} in a given event, due to the impressive hermiticity of
1327 the calorimeters. Unfortunately, the calorimeters do not know “where” from where
1328 their energy deposition came, and thus CST is susceptible to drastically reduced
1329 performance as pileup is increased.

1330 TST E_T^{miss} is the standard for ATLAS searches as currently performed by ATLAS.
1331 TST E_T^{miss} is built by using the calibrated hard objects and the soft term is built from
1332 the tracks which are not assigned to any of those hard objects. In particular, due
1333 to the impressive track-vertex association efficiency, one chooses tracks which only
1334 come from the primary vertex. This drastically reduces the pileup contributions to
1335 the E_T^{miss} measurement. However, since the ID tracking system is unable to measure
1336 neutral objects, the TST E_T^{miss} is “wrong”. This bias is important to understand for
1337 many measurements. However, in most searches for new physics, the soft E_T^{miss} is
1338 generally a small fraction of the total E_T^{miss} , and thus this bias is not particularly
1339 hurtful.

1340 PFlow E_T^{miss} uses the PFOs described above to build the E_T^{miss} . The PFOs which
1341 are assigned to hard objects are calibrated, and the PFOs which are not assigned
1342 to any hard object are added to the soft term. In this context, it is convenient to
1343 distinguish between “charged” and “neutral” PFOs. Charged PFOs can be seen as a
1344 topocluster which has an associated track, while neutral PFOs do not. This charged
1345 PFO is essentially a topocluster that we are “sure” comes from the primary vertex.
1346 The neutral PFOs are in the same status as the original topoclusters. Thus a “full”
1347 PFlow E_T^{miss} should have performance somewhere between TST E_T^{miss} and CST E_T^{miss} ³.

1348 A *charged* PFlow E_T^{miss} should for sanity be the same as TST.

1349 **Measuring E_T^{miss} Performance : event selection**

1350 The question is now straightforward: how do we compare these different algorithms?
1351 We compare these algorithms in $Z \rightarrow \ell\ell + \text{jets}$ and $W \rightarrow \ell\nu + \text{jets}$ events. Due to
1352 the presence of leptons, these events are well-measured “standard candles”. Here
1353 we present the results in early 2015 data with $Z \rightarrow \mu\mu$ and $W \rightarrow e\nu$ events, as
1354 shown in [112, 113]. This result was important to assure the integrity of the E_T^{miss}
1355 measurements at the higher energy and pileup environment of Run-2.

1356 The $Z \rightarrow \ell\ell$ selection is used to measure the intrinsic E_T^{miss} resolution of the
1357 detector. The only possible source of neutrinos in these decays is from heavy-flavor
1358 decays inside of jets, and thus $Z \rightarrow \ell\ell$ events they have very low E_T^{miss} . This provides
1359 an ideal event topology to understand the modelling of E_T^{miss} mismeasurement.
1360 Candidate $Z \rightarrow \mu\mu$ events are first required to pass a muon or electron trigger, as
1361 described in Table 5.1. Offline, the selection of $Z \rightarrow \mu\mu$ events requires exactly two
1362 medium muons. The muons are required to have opposite charge and $p_T > 25 \text{ GeV}$,
1363 and mass of the dimuon system is required to be consistent with the Z mass
1364 $|m_{ll} - m_Z| < 25 \text{ GeV}$.

$W \rightarrow \ell\nu$ events are an important topology to evaluate the E_T^{miss} modelling in
an event with real E_T^{miss} . This E_T^{miss} is from the neutrino, which is not detected.
The E_T^{miss} in these events has a characteristic distribution with a peak at $\frac{1}{2}m_W$. The
selection of $W \rightarrow e\nu$ events begins with the selection of exactly one electron of medium
quality. A selection on TST $E_T^{\text{miss}} > 25 \text{ GeV}$ drastically reduces the background from
multijet events where the jet fakes an electron. The transverse mass is used to select

³Naively, due to approximate isospin symmetry, about 2/3 of the hadrons will be charged and 1/3 will be neutral.

the $W \rightarrow e\nu$ events :

$$m_T = \sqrt{2p_T^\ell E_T^{\text{miss}}(1 - \cos \Delta\phi)}, \quad (6.6)$$

1365 where $\Delta\phi$ is the difference in the ϕ between the E_T^{miss} and the electron. m_T is required
1366 to be greater than 50 GeV.

1367 There are two main ingredients to investigate : the E_T^{miss} resolution and the E_T^{miss}
1368 scale.

1369 **Measuring E_T^{miss} Performance in early 2015 data : metrics**

1370 To compare these algorithms we use the E_T^{miss} resolution, E_T^{miss} scale, and the
1371 linearity. Representative distributions of TST E_x^{miss} , E_y^{miss} , and E_T^{miss} from early
1372 2015 datataking are shown in Fig.6.10.

The E_T^{miss} resolution is an important variable due to the fact that the bulk of the distributions associated to $E_{x(y)}^{\text{miss}}$ are Gaussian distributed [Aad2012]. However, to properly measure the tails of this distribution, especially when considering non-calorimeter based soft terms, it is important to use the root-mean square as the proper measure of the resolution. This is strictly larger than a resolution as measured using a fit to a Gaussian, due to the long tails from i.e. track mismeasurements. The resolution is measured with respect to two separate variables : $\sum E_T$ and N_{PV} . $\sum E_T$ is an important measure of the “total event activity”. It is defined as

$$\sum E_T = \sum p_T^e + \sum p_T^\gamma + \sum p_T^\tau + \sum p_T^{\text{jets}} + \sum p_T^\mu + \sum p_T^{\text{soft}}. \quad (6.7)$$

1373 The measurement as a function of N_{PV} is useful to understand the degradation of
1374 E_T^{miss} performance with increasing pileup. Figure 6.11 shows the E_T^{miss} resolution in
1375 the early 2015 data. The degradation of the E_T^{miss} performance is shown as a function
1376 of pileup N_{PV} and total event activity $\sum E_T$.

Another important performance metric is the E_T^{miss} scale, or how “right” we are in our E_T^{miss} calculation. This can be off in various directions, as CST E_T^{miss} contains

additional particles from pileup, while soft neutral particles⁴ are ignored by TST E_T^{miss} .

To measure this in data, we again use $Z \rightarrow \mu\mu$ events, where the $Z \rightarrow \mu\mu$ system is treated as a well-measured reference object. The component of E_T^{miss} which is in the same direction as the reconstructed $Z \rightarrow \mu\mu$ system is sensitive to potential biases in the detector response. The unit vector \mathbf{A}_Z of the Z system is defined as

$$\mathbf{A}_Z = \frac{\vec{p}_T^{\ell^+} + \vec{p}_T^{\ell^-}}{|\vec{p}_T^{\ell^+} + \vec{p}_T^{\ell^-}|}, \quad (6.8)$$

where $\vec{p}_T^{\ell^+}$ and $\vec{p}_T^{\ell^-}$ are the transverse momenta of the leptons from the Z boson decay. The relevant scale metric is then the mean value of the \vec{E}_T^{miss} projected onto \mathbf{A}_Z : $\langle \vec{E}_T^{\text{miss}} \cdot \mathbf{A}_Z \rangle$. In Figure 6.12, the scale is shown for the early 2015 dataset. The negative bias, which is maximized at about 5 GeV, is a reflection of two separate effects. The soft neutral particles are missed by the tracking system, and thus ignored in TST E_T^{miss} . Missed particles due to the limited ID acceptance can also affect the scale.

For events with real E_T^{miss} , one can also look at the *linearity* in simulation. This is defined as

$$\text{linearity} = \left\langle \frac{E_T^{\text{miss}} - E_T^{\text{miss,Truth}}}{E_T^{\text{miss,Truth}}} \right\rangle. \quad (6.9)$$

$E_T^{\text{miss,Truth}}$ refers to “truth” particles as defined before, or the magnitude of the vector sum of all noninteracting particles. The linearity is expected to be zero if the E_T^{miss} is reconstructed at the correct scale.

1387 Particle Flow Performance

As described above, the resolution, scale, and linearity are the most important metrics to understand the performance of the different E_T^{miss} algorithms. In this section, we present comparisons of the different algorithms, including particle flow, in simulation

⁴“Soft” here means those particles which are not hard enough to be reconstructed as their own particle, using the reconstruction algorithms above.

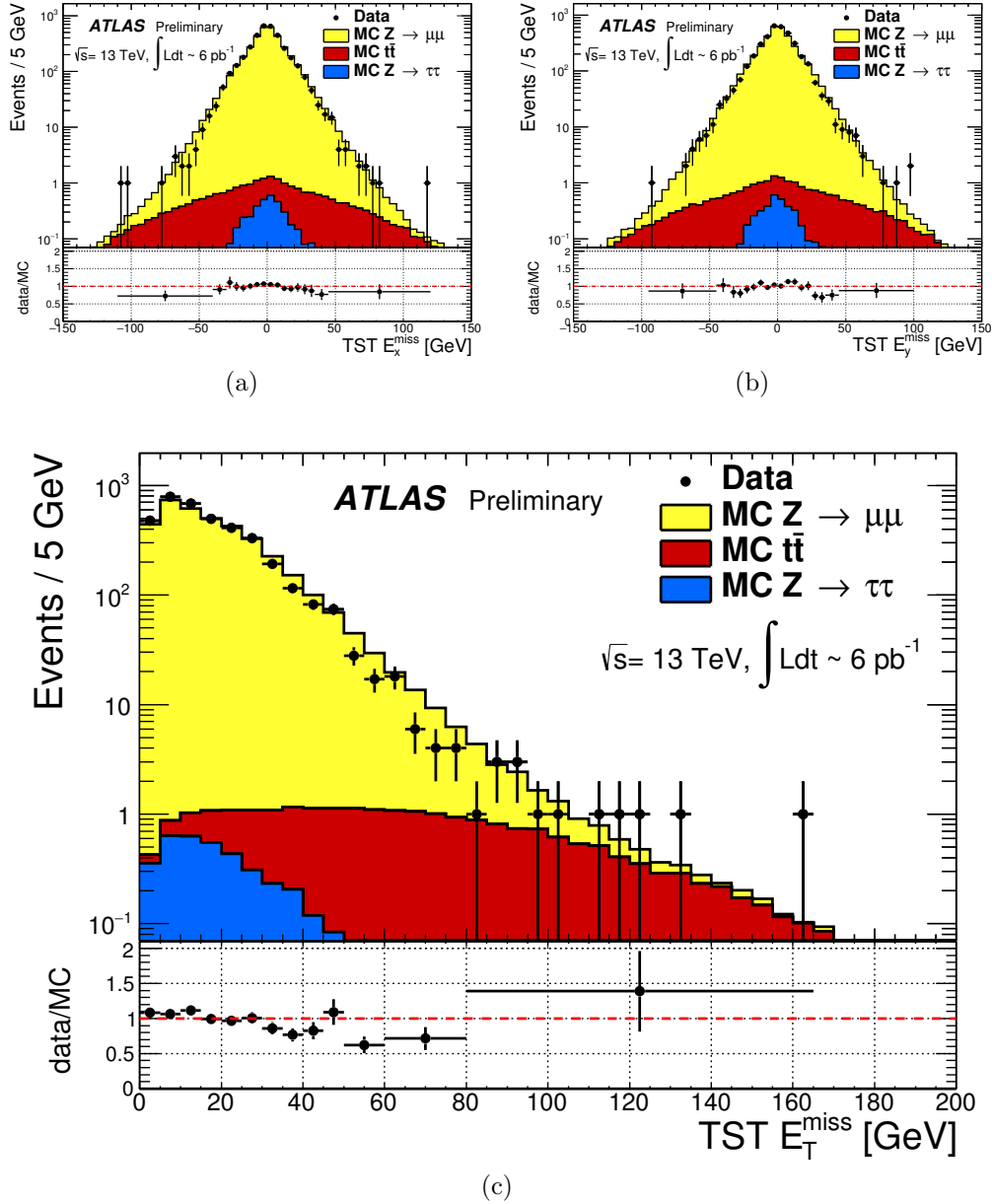


Figure 6.10: $TST E_x^{\text{miss}}$, E_y^{miss} , and E_T^{miss} distributions of early $\sqrt{s} = 13$ TeV data compared with simulation after the $Z \rightarrow \mu\mu$ selection described in Sec. 6.2. The data sample consists of 6 pb^{-1} .

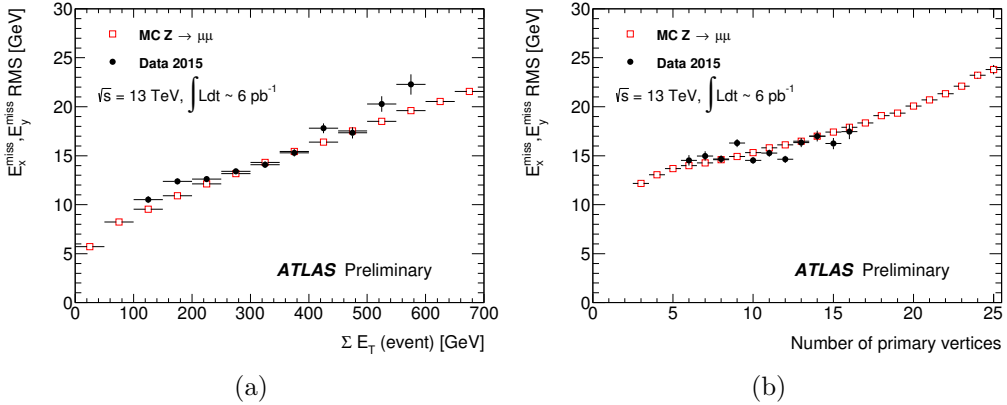


Figure 6.11: Resolution of TST E_T^{miss} of early $\sqrt{s} = 13$ TeV data compared with simulation after the $Z \rightarrow \mu\mu$ selection described in Sec.6.2. The data sample consists of 6 pb^{-1} .

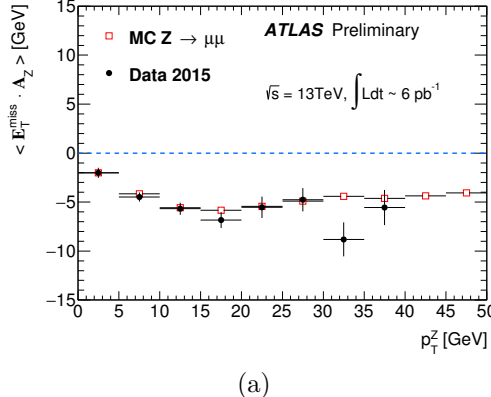


Figure 6.12: Scale of TST E_T^{miss} of early $\sqrt{s} = 13$ TeV data compared with simulation after the $Z \rightarrow \mu\mu$ selection described in Sec.6.2. The data sample consists of 6 pb^{-1} .

1391 and using a data sample from 2015 of 80 pb^{-1} . In these plots, ‘‘MET_PFlow-TST’’
1392 refers to charged PFlow E_T^{miss} , while the other algorithms are as described above.

1393 Figures ?? show the resolution and scale in simulated $Z \rightarrow \mu\mu$ events. The
1394 resolution curves follow the ‘‘intuitive’’ behavior discussed before. Due to the high
1395 pileup in 2015 run conditions, the CST E_T^{miss} resolution is poor, and becomes even
1396 poorer with increasing pileup and event activity. The ‘‘regular’’ PFlow E_T^{miss} shows
1397 reduces pileup and event activity dependence as compared to the CST. As stated
1398 earlier, the E_T^{miss} from the PFlow algorithm can be seen as a hybrid of TST E_T^{miss}

1399 and CST E_T^{miss} . The charged PFOs ($\sim 2/3$) are pileup suppressed, while the neutral
1400 PFOs (or topoclusters) are not. Both charged PFlow and TST E_T^{miss} show only a
1401 small residual dependence on N_{PV} and $\sum E_T$, since they have fully pileup suppressed
1402 inputs through the track associations.

1403 The scale plots are shown for $Z + \text{jets}$ events and Z events with no jets. For the
1404 nonsuppressed CST, the scale continues to worsen with increasing p_T^Z . It is almost
1405 always the worst performing algorithm. The standard PFlow algorithm performs the
1406 second worst in the region of high p_T^Z , but is the best at low p_T^Z . The most exciting note
1407 in this plot is the improved scale of the charged PFlow E_T^{miss} compared to the TST
1408 E_T^{miss} . Considering the resolution is essentially identical, the PFlow algorithm is better
1409 picking up the contributions from additional neutral particles. In events with no jets,
1410 the soft term is essentially the only indication of the E_T^{miss} mismeasurement, since
1411 the muons will be well-measured. In this case, the pileup effects cancel, on average,
1412 due to the $U(1)_\phi$ symmetry of the ATLAS detector, and CST performs rather well
1413 compared to the more complicated track-based algorithms. The full PFlow algorithm
1414 performs best, since it provides a small amount of pileup suppression on the neutral
1415 components from CST.

1416 The resolution and linearity are shown in simulated $W \rightarrow e\nu$ events in Figure ???.
1417 The resolution in $W \rightarrow e\nu$ events shows a similar qualitative behavior to that shown
1418 in $Z \rightarrow \mu\mu$ events. The CST E_T^{miss} has the worst performance, with charged PFlow
1419 E_T^{miss} performing best. The surprise here is that the scale associated to TST E_T^{miss} in
1420 these events is best throughout the space parameterized by $E_T^{\text{miss,Truth}}$, except for one
1421 bin at $40 \text{ GeV} < E_T^{\text{miss,Truth}} < 50 \text{ GeV}$. The scale in these events is best measured
1422 using a track-based soft term.

1423 The resolution also investigated in real data passing the $Z \rightarrow \mu\mu$ selection
1424 described above. A comparison of the E_T^{miss} between real data and simulation for
1425 each algorithm is presented in Figure 6.16. The resolution as a function of $\sum E_T$ and

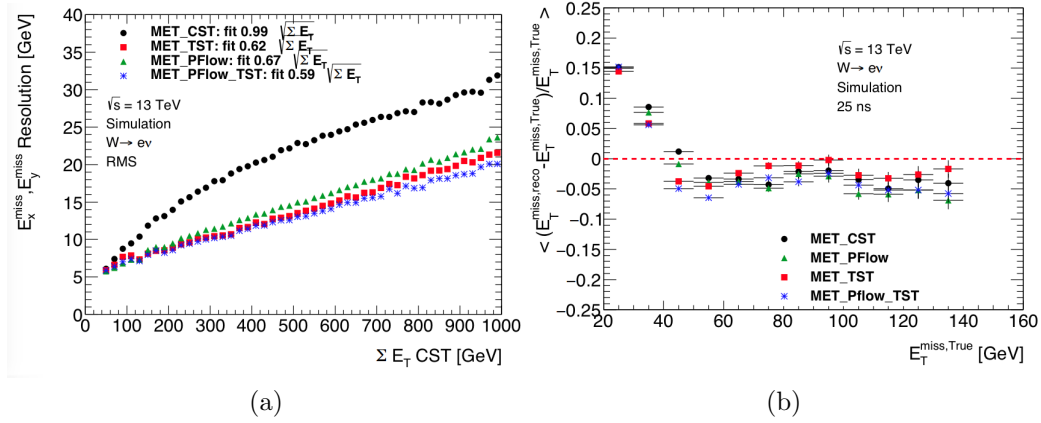


Figure 6.13: Comparison of E_T^{miss} resolution and linearity using different E_T^{miss} algorithms with simulated $W \rightarrow e\nu$ events.

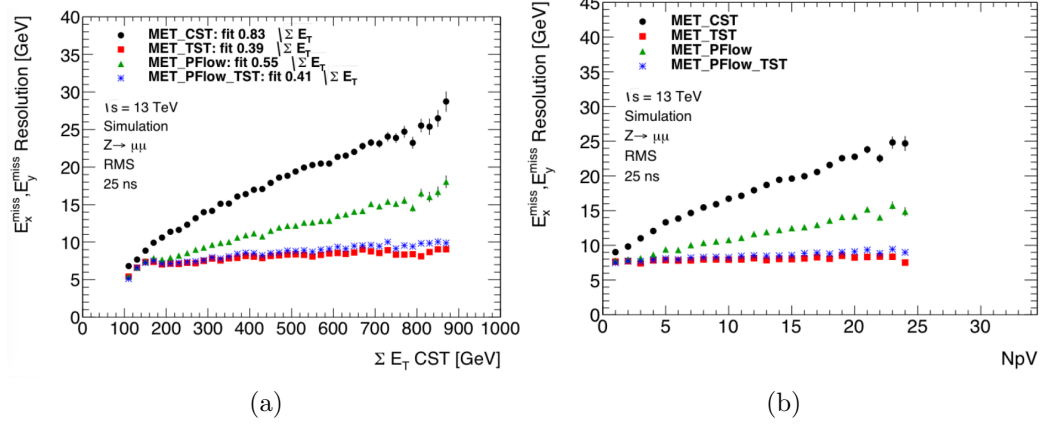


Figure 6.14: Comparison of E_T^{miss} resolution using different E_T^{miss} algorithms with simulated $Z \rightarrow \mu\mu$ events.

1426 N_{PV} is shown in Figure 6.17 for this dataset. Overall, this plot shows the same general
 1427 features as the simulation dataset in terms of algorithm performance. However, the
 1428 performance of all algorithms seems to be significantly worse in data. This is likely due
 1429 to simplifications made in the simulation: soft interactions that cannot be simulated
 1430 can have a significant effect on an event level variable such as the E_T^{miss} resolution.

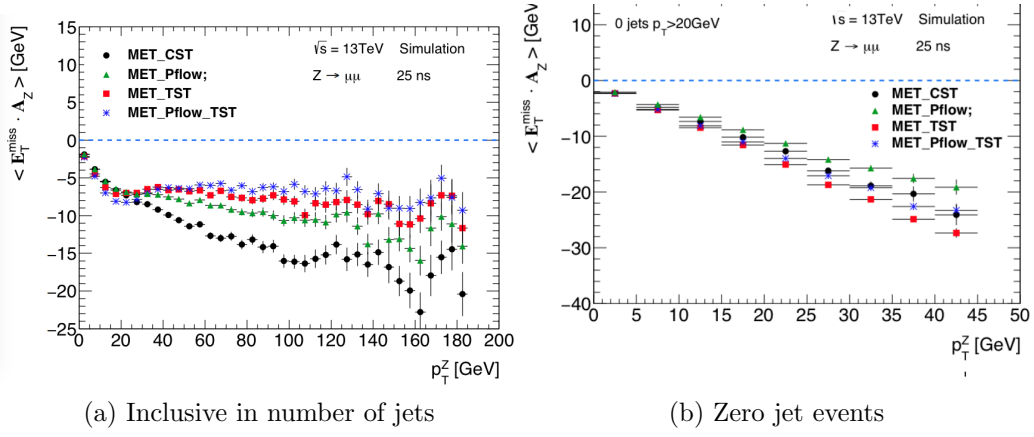


Figure 6.15: Comparison of E_T^{miss} scale using different E_T^{miss} algorithms with simulated $Z \rightarrow \mu\mu$ events.

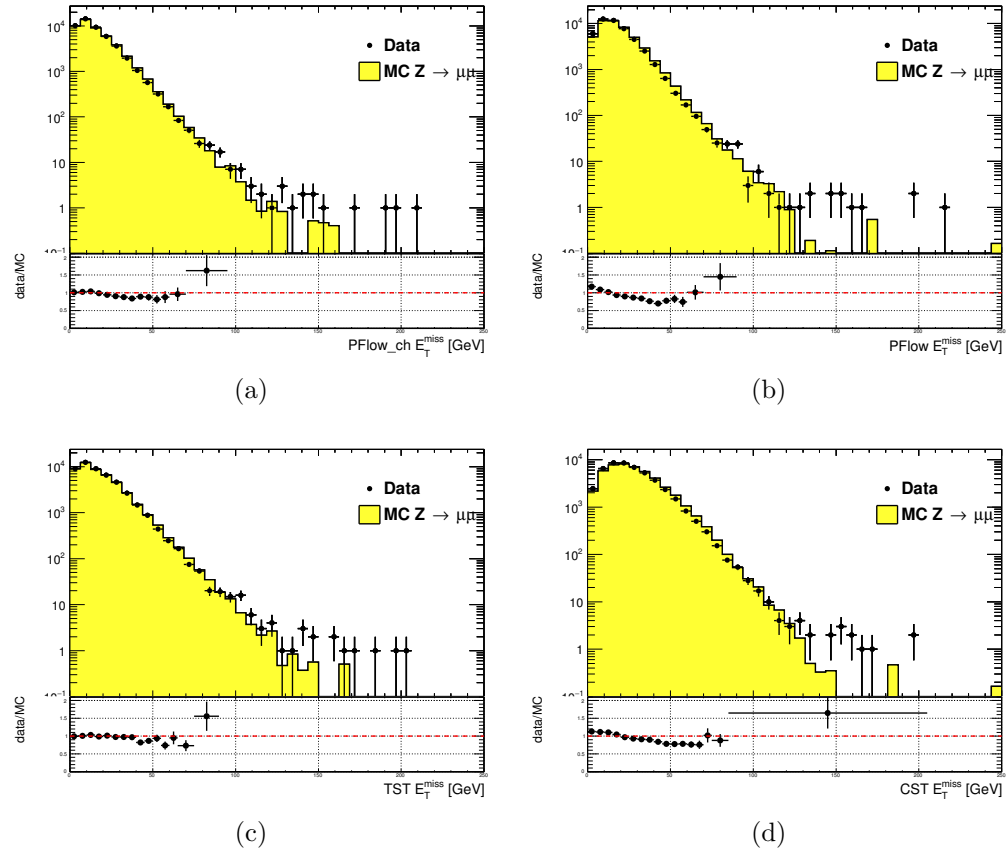


Figure 6.16: Comparison of E_T^{miss} distributions using different E_T^{miss} algorithms with a data sample of 80 pb^{-1} after the $Z \rightarrow \mu\mu$ selection described in Sec. 6.2

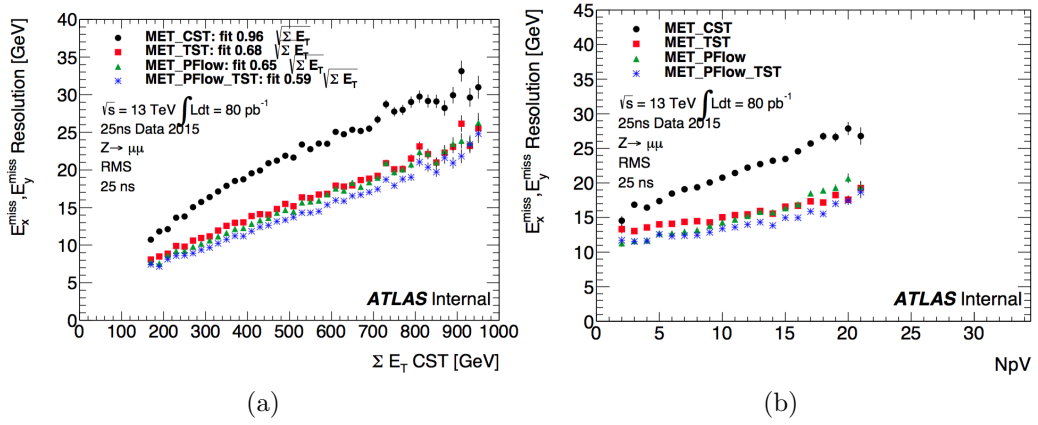


Figure 6.17: Comparison of E_T^{miss} resolution using different E_T^{miss} algorithms with a data sample of 80 pb^{-1} after the $Z \rightarrow \mu\mu$ selection described in Sec.6.2

1431

Chapter 7

1432

Recursive Jigsaw Reconstruction

1433 *Recursive Jigsaw Reconstruction* (RJR) [114, 115] is a novel algorithm used for the
 1434 analysis presented in this thesis. RJR is the conceptual successor to the razor
 1435 technique [116, 117], which has been used successfully in many new physics searches
 1436 [37, 38, 40, 41, 47, 118]. In this chapter, we will first present the razor technique,
 1437 and describe the razor variables. We will then present the RJR algorithm. After the
 1438 description of the algorithm, we will describe the precise RJR variables used by this
 1439 thesis and attempt to provide some physical intuition of what they describe.

1440

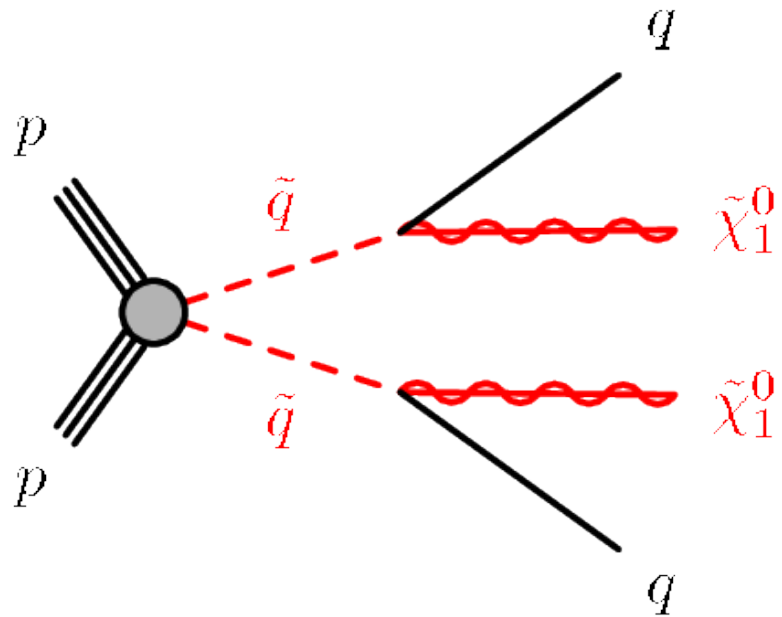
7.1 Razor variables

1441

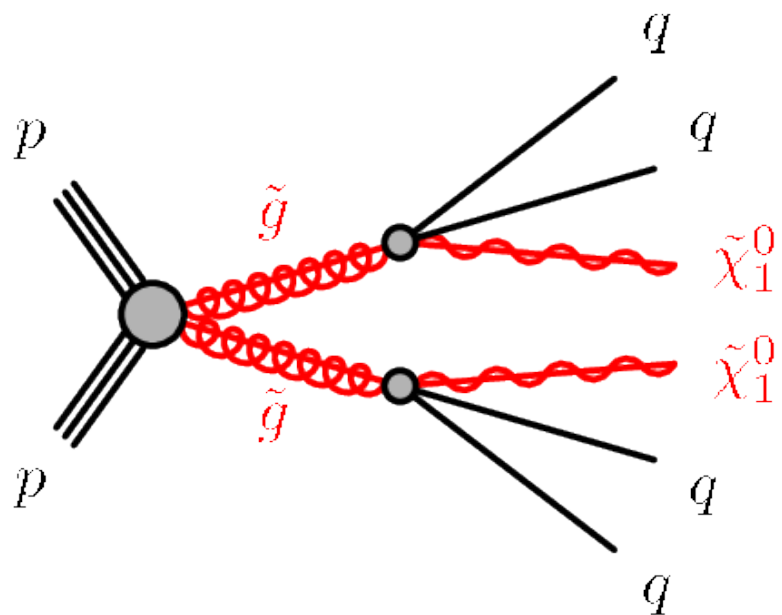
Motivation

1442 In this thesis, we consider SUSY models where gluinos and squarks are pair-produced.
 1443 Pair-production is a consequence of the R -parity imposed in many SUSY models.
 1444 R -parity violation is highly constrained by limits on proton decay[15], and is often
 1445 assumed in SUSY model building. The Feynman diagrams considered are shown in
 1446 Fig.7.1.

1447 As discussed previously, the consequences of this \mathbb{Z}_2 symmetry are drastic. To un-
 1448 derstand the utility of the razor variables, the stability of the lightest supersymmetric
 1449 particle is very important. In many SUSY models, including the ones considered in
 1450 this thesis, this is the lightest neutralino $\tilde{\chi}_1^0$. This means that on either side of a
 1451 SUSY decay process, where we begin with disparticle production, we have a final



(a) Disquark production



(b) Digluino production

Figure 7.1: Feynman diagrams for the SUSY signals considered in this thesis

1452 state particle which is not detected. Generically, this leads to E_T^{miss} . Selections based
1453 on E_T^{miss} are very good at reducing dominant backgrounds, for example from QCD
1454 backgrounds.

1455 However, there are limitations to searches based on E_T^{miss} . Due to jet mismeasurements,
1456 instrumental failures, finite detector acceptance, nongaussian tails in the
1457 detector response, and production of neutrinos inside of jets, there are many sources of
1458 “fake” E_T^{miss} which does not correspond to a Standard Model neutrino or new physics
1459 object such as an LSP. An additional limitation is the complete lack of longitudinal
1460 information. As events from i.e. QCD backgrounds tend to have higher boosts along
1461 the z -direction, this is ignoring an important handle in searches for new physics.
1462 Finally, E_T^{miss} is only one object, which is a measurement for *two* separate LSPs. If one
1463 could factorize this information somehow, this would provide additional information
1464 to potentially discriminate against backgrounds. The *razor variables* (M_{Δ}^R, R^2) are
1465 more robust than standard variables against these effects[116, 117].

1466 Derivation of the razor variables

1467 To derive the razor variables (M_{Δ}^R, R^2), we start with a generic situation of the pair
1468 production of heavy sparticles with mass m_{Heavy} .¹ Each sparticle decays to a number
1469 of observable objects (in this thesis, jets), and an unobservable $\tilde{\chi}_1^0$ of mass $m_{\tilde{\chi}_1^0}$. We
1470 will combine all of the jets into a *megajet*; this process will be described below. We
1471 begin by analyzing the decay in the “rough-approximation”, or in modern parlance,
1472 *razor frame* (*R-frame*). This is the frame where each sparticle is at rest. The complete
1473 set of frames considered in the case of the razor variables is shown in 7.2.

In the *R-frame*, the decay is straightforward to analyze. By construction, there
are in fact two *R-frame* s, and they have identical kinematics. Each megajet has

¹The razor variables have undergone confusing notational changes over the years. We will be self-consistent, but the notation used here may be different from references.

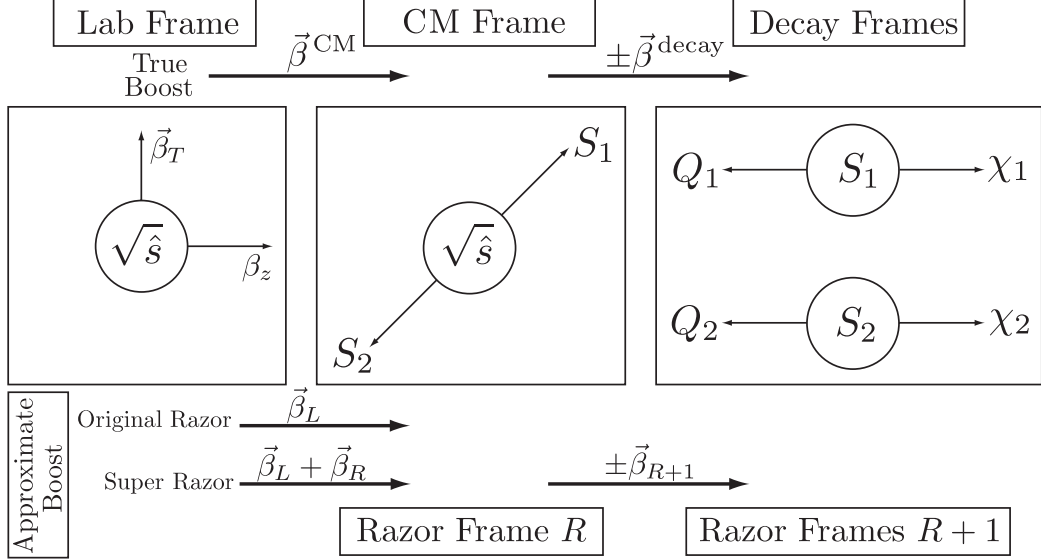


Figure 7.2: Frames considered when applying the razor technique, from [117].

energy E_1^R, E_2^R in the frame of its parent sparticle, and we define a characteristic mass M_R :

$$E_1^R = E_2^R = \frac{m_{\text{Heavy}}^2 - m_{\tilde{\chi}_1^0}^2}{2m_{\text{Heavy}}} \quad (7.1)$$

$$M_R = 2 \times E_1^R = 2 \times E_2^R = \frac{m_{\text{Heavy}}^2 - m_{\tilde{\chi}_1^0}^2}{m_{\text{Heavy}}} \quad (7.2)$$

1474 For cases where $m_{\text{Heavy}} \gg m_{\tilde{\chi}_1^0}$, M_R is an estimator of m_{Heavy} . This scenario happens
 1475 in the SM, such as in $t\bar{t}$ and WW events, where the $\tilde{\chi}_1^0$ is instead a neutrino.

1476 The question now is how to use this simple derivation in the lab frame, where we
 1477 actually have measurements. There are two related issues: how to combine the jets
 1478 into the megajets, and how to “transform” (or *boost*) to the R -frame.

To construct the megajets, the procedure is the following. For a given set of jets $j_i, i = 0, \dots, n_{\text{jet}}$, we construct *all* combinations of their four-momenta such that there is at least one jet inside each megajet. Among this set of possible megajets $\{J_{1,2}\}$, we make the following unique choice for the megajets. We minimize the following quantity:

$$m_{J_1}^2 + m_{J_2}^2. \quad (7.3)$$

1479 In modern parlance, this is known as a *jigsaw*. It is important to note, this is a
 1480 *choice*. It may have nice physical qualities or satisfy some convenient intuition about
 1481 the events, but as we will see later, other choices are possible.

We now describe how we translate our megajet kinematics, measured in the lab frame, to the R -frame. This is a two-step procedure. We perform two *boosts*: a longitudinal boost β_L and a transverse boost β_T . Schematically,

$$J_1^R \xrightarrow{\beta_T} J_1^{CM} \xrightarrow{\beta_L} J_1^{\text{lab}} \quad (7.4)$$

$$J_2^R \xrightarrow{-\beta_T} J_2^{CM} \xrightarrow{\beta_L} J_2^{\text{lab}} \quad (7.5)$$

$$(7.6)$$

1482 The $J_{1,2}^{\text{lab}}$ correspond directly to those in the megajet construction. We drop the
 1483 “lab” designation for the rest of the discussion. The question is how to compute the
 1484 magnitudes of these boosts, given the missing degrees of freedom.

For the transverse boost β_T , recall the two megajets have equal energies in their R -frame by construction. This constraint can be reexpressed as a constraint on the magnitude of this boost, in terms of the boost velocity β_L (and Lorentz factor γ_L):

$$\beta_T = \frac{\gamma_L(E_1 - E_2) - \gamma_L\beta_L(p_{1,z} - p_{2,z})}{\hat{\beta}_T \cdot (\vec{p}_{1,T} + \vec{p}_{2,T})} \quad (7.7)$$

where we have denoted the lab frame four-vectors as $p_i = (E_i, \vec{p}_{i,T}, p_z)$. We now make the *choice* for the direction of the transverse boost $\hat{\beta}_T$:

$$\hat{\beta}_T = \frac{\vec{p}_{1,T} + \vec{p}_{2,T}}{|\vec{p}_{1,T} + \vec{p}_{2,T}|}. \quad (7.8)$$

1485 This choice forces the denominator of 7.7 to unity, and corresponds to aligning the
 1486 transverse boost direction with the sum of the two megajets transverse directions.

For the longitudinal boost, we choose $\vec{\beta}_L$ along the z -direction, with magnitude:

$$\beta_L = \frac{p_{1,z} + p_{2,z}}{E_1 + E_2}. \quad (7.9)$$

1487 Viewed in terms of the original parton-parton interactions, this is the choice which
 1488 “on average” gives $p_{z,\text{CM}} = 0$, as we would expect. This well-motivated choice due to
 1489 the total z symmetry.

We now have well-motivated guesses for both boosts, which allow us write our original characteristic mass M_R in terms of the lab frame variables, by application of these two Lorentz boosts to the energies of 7.1:

$$M_R^2 \xrightarrow{\beta_T} M_{R,\text{CM}}^2 \xrightarrow{\beta_L} M_{R,\text{lab}}^2 = (E_1 + E_2)^2 - (p_{1,z} + p_{2,z})^2. \quad (7.10)$$

Finally, we define an additional mass variable, which include the missing transverse energy $E_{\text{T}}^{\text{miss}}$. Importantly, note that we did not use the $E_{\text{T}}^{\text{miss}}$ in the definition of M_R , which depends only on the energies of the megajets. Backgrounds with no invisible particles (such as multijet events) must have J_1 and J_2 back to back. Thus, we define the transverse mass:

$$(M_R^T)^2 = \frac{1}{2} \left[E_{\text{T}}^{\text{miss}}(p_{1,T} + p_{2,T}) - \vec{E}_{\text{T}}^{\text{miss}} \cdot (\vec{p}_{1,T} + \vec{p}_{2,T}) \right]. \quad (7.11)$$

Generally, we have $M_R^T < M_R$, so we define a dimensionless ratio (“the razor”):

$$R^2 = \left(\frac{M_R^T}{M_R} \right)^2. \quad (7.12)$$

1490 For signal events, we expect R to peak around $R \sim 1/4$, while backgrounds without
 1491 real $E_{\text{T}}^{\text{miss}}$ are expected to have $R \sim 0$.

1492 7.2 Recursive Jigsaw Reconstruction

1493 Recursive Jigsaw Reconstruction is an algorithm allowing the imposition of a decay
 1494 tree interpretation on an particular event[114, 115]. The idea is to construct the
 1495 underlying kinematic variables (the masses and decay angles) on an event-by-event
 1496 level. This is done “recursively” through a decay tree which corresponds (sometimes
 1497 approximately) to the Feynmann diagram for the signal process of interest. After

1498 each step of the recursive procedure, the objects are “placed” into one bucket (or
1499 branch) of the decay tree, and the process is repeated on each frame we have imposed.
1500 The imposition of these decay trees is done by *jigsaw* rule: a procedure to resolve
1501 combinatoric or kinematic ambiguities while traversing the decay tree. This procedure
1502 is performed by the `RestFrames` software packages [119]

1503 In events where all objects are fully reconstructed, this is straightforward, and
1504 of course has been used for many years in particle physics experiments. Events
1505 which contain E_T^{miss} are more difficult, due to the loss of information: the potential
1506 for multiple mismeasured or simply unmeasureable objects, such as neutrinos or the
1507 LSP in SUSY searches. There can also be combinatoric ambiguities in deciding how
1508 to group objects of the same type; specifically here, we will be concerned with the
1509 jigsaw rule to associate jets to a particular branch of a decay tree. The jigsaw rules
1510 we impose will remove these ambiguities. First, we will describe the decay trees used
1511 in this thesis, and then describe the jigsaw rules we will use. Finally, we will describe
1512 the variables used in the all-hadronic SUSY search presented in this thesis.

1513 Decay Trees

1514 The decay trees imposed in this thesis are shown in 7.3. Leaving temporarily the
1515 question of “how” we apply the jigsaw rules, let us compare these trees to the signal
1516 processes of interest. In particular, we want to compare the Feynman diagrams of 7.1
1517 with the decay trees of 7.3. The decay tree in ?? corresponds exactly to that expected
1518 from disquark production, and matches very closely with the principles of the razor
1519 approach. We first apply a jigsaw rule, indicated by a line, to the kinematics of the
1520 objects in the *lab* frame. This outputs the kinematics of our event in the *parent-parent*
1521 (*PP*) frame, or in the razor terminology, the CM frame. That is, the kinematics of
1522 this frame are an estimator for the kinematics in the center of mass frame of the
1523 disquark system. We apply another jigsaw, which splits the objects in the *PP* frame

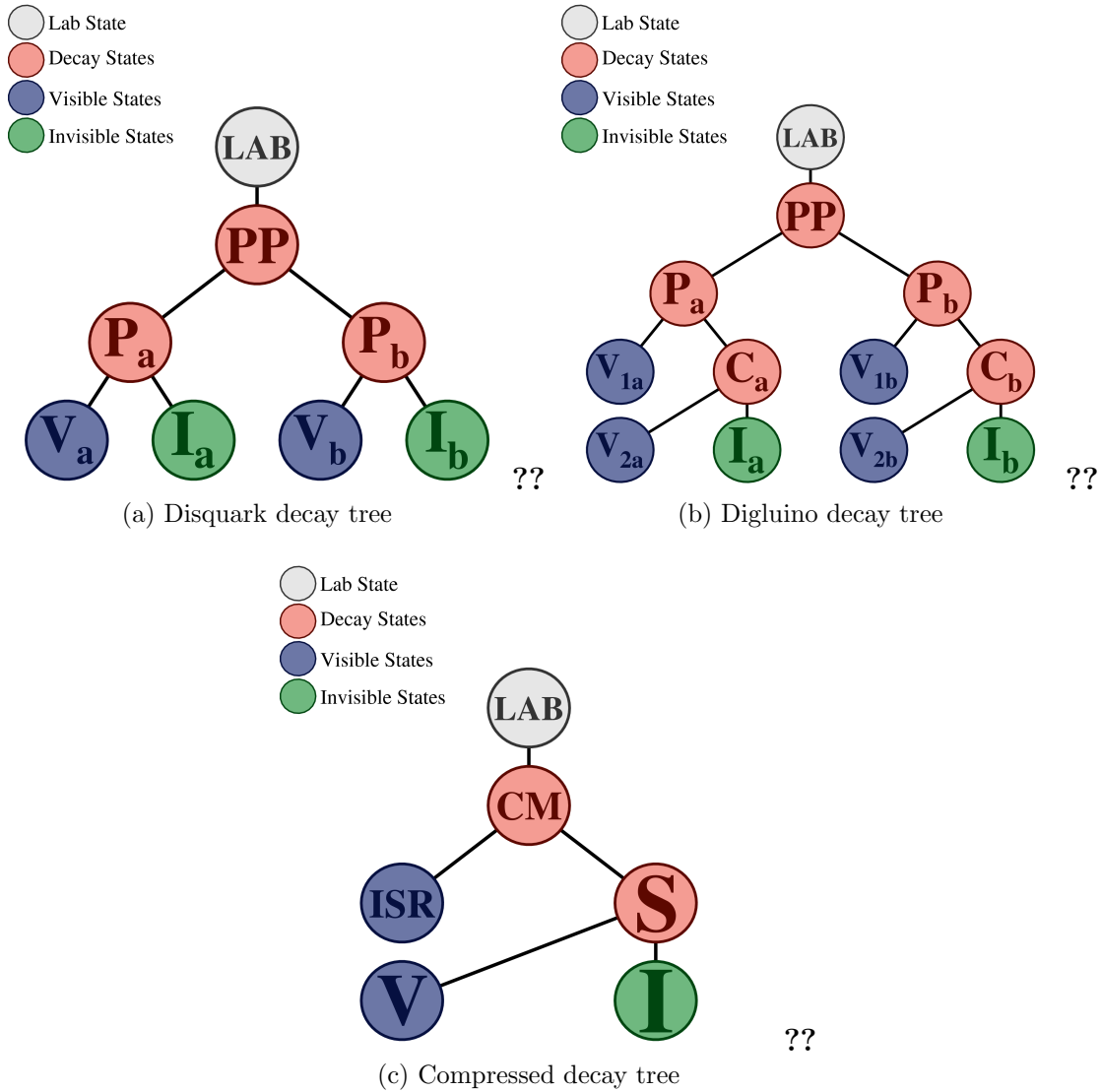


Figure 7.3: RJR decay trees imposed in this thesis

1524 into two new frames, known as the P_a and P_b systems. These are equivalent to the
 1525 razor frames of the razor technique, and represent proxy frames where each squark
 1526 is at rest. In $P_a(P_b)$, the decay is symmetric between the visible $V_a(V_b)$ objects and
 1527 the invisible system $I_a(I_b)$. To generate the estimator of the kinematics of the V_a , V_b ,
 1528 I_a , and I_b systems in the P_a and P_b systems, we apply another jigsaw rule to split the
 1529 total E_T^{miss} between P_a and P_b , which allows calculations of these kinematics in these
 1530 frames. For the case of disquark production, this is the expected decay tree, and we

1531 stop the recursive calculation at that level.

1532 In the case of digluino production, we expect two additional jets, and we can
1533 perform an additional boost in each of P_a and P_b , to what we call the C_a and C_b frames.
1534 The decay tree is shown in ?? . In this case we apply a jigsaw at the level of $P_a(P_b)$
1535 which separates a single visible object V_{1a} (V_{2a}) from the child frame $C_a(C_b)$. This
1536 child frame represents the hypothesized squark after the decay $\tilde{g} \rightarrow g\tilde{q}$, which then
1537 decays as in the squark case. This gives additional information which will be exploited
1538 for the gluino specific search regions.

The final decay tree used in this thesis is the *compressed* decay tree. Compressed refers to signal models which have a small splitting between the mass of the proposed sparticle and the $\tilde{\chi}_1^0$. In this case, the sparticle decay products (i.e. the jets and E_T^{miss}) do not generally have large scale[114]. Instead, the strategy is generally to look for a large-scale initial state radiation (ISR) jet which is recoiling off the disparticle system. In the case where the LSPs receive no momentum from the sparticle decays, the following approximation holds:

$$E_T^{\text{miss}} \sim -p_T^{\text{ISR}} \times \frac{m_{\tilde{\chi}_1^0}}{m_{\text{sparticle}}} \quad (7.13)$$

1539 where p_T^{ISR} is the transverse momentum associated to the entire ISR system.

1540 RJR offers a natural and straightforward way to exploit this feature in events
1541 containing ISR. One imposes the simple decay tree in ?? with associated jigsaw rules.
1542 With suitable jigsaw rules, this decay tree “picks out” the large p_T ISR jet, recoiling
1543 off the E_T^{miss} and additional radiation from the sparticle decays. This provides a
1544 convenient set of variables to understand compressed scenarios.

1545 In this section, we have seen how one imposes particular decay trees on an event
1546 to produce a basis of kinematic variables in the approximated frames relevant to
1547 the hypothesized sparticle decay chain. This explains why we call this procedure
1548 “recursive”: we can continue the procedure through as many steps of a decay tree as

1549 we want, and each application of a jigsaw rule is dependent on the variables produced
1550 in the last step. The question, of course, is *what are these jigsaw rules?*.

1551 **Jigsaw Rules**

1552 Jigsaw rules are the fundamental step that allow the recursive definitions of the
1553 variables of interest. We want rules which allow us to fully define kinematic variables
1554 at each step in a decay tree. The only possible solution to fully define the event
1555 kinematics in terms of the frames of the hypothesized decays is the imposition of
1556 external constraints to eliminate additional degrees of freedom. In principle, these
1557 need not have any particular physical motivation. Instead, the jigsaw rules are a
1558 way to resolve the mathematical ambiguities to fully reconstruct the full decay chain
1559 kinematics. However, most practical jigsaw rules also have some reasonable physical
1560 motivation, which we will also elucidate.

1561 In the original razor point of view, some jigsaw rules can be seen as the definitions
1562 of the boosts which relate the different frames of interest, while other rules allow one
1563 to combine multiple objects and place them into a particular hemisphere (previously
1564 megajet). These are the two forms of jigsaw rules: combinatoric and kinematic. As
1565 we have stressed before, the jigsaw rules are a *choice*; as long as a particular jigsaw
1566 rule allows the definition of variables at each step in a decay tree, it is “as valid” as
1567 any other rule.

Practically speaking, in this thesis we use only a small subset of possible jigsaw
rules. The combinatoric jigsaw rule we use has already been introduced as megajet
construction above. The minimization of

$$m_{J_1}^2 + m_{J_2}^2. \quad (7.14)$$

1568 is a jigsaw rule to deal with the combinatoric ambiguity implicit in which jets go in
1569 which hemisphere. This is the jigsaw rule used in the decay trees when going from

1570 one frame to two frames such as $PP \rightarrow P_a, P_b$.

1571 We will use three other jigsaw rules, which are both kinematic jigsaw rules. One
1572 has already been used in the razor technique. The minimization of β_L will be used
1573 as the jigsaw rule in the first step of each decay tree: the lab frame to the PP/CM
1574 frame. This is in effect the imposition of longitudinal boost invariance, as we expect
1575 on average $p_{z,PP,\text{CM}} = 0$. One defines a unique longitudinal boost by imposition of
1576 this external constraint.

1577 The final two jigsaw rules used in this thesis was not used in the razor technique.

1578 We describe them here.

The first kinematic ambiguity is the total mass of the invisible system M_I . We
guess this to be:

$$M_I^2 = M_V^2 - 4M_{V_a}M_{V_b}. \quad (7.15)$$

1579 As we stated above, there is no need to “justify” the jigsaw rules, as they are in some
1580 ways a mathematical trick to fully resolve the event kinematics. However in this case,
1581 there is a nice property of this guess. The symmetry of the production mechanism,
1582 where we have two decay products V_i and I_i produced from the decay of the same
1583 heavy sparticle, is explicit with this jigsaw choice.

1584 The final jigsaw rule we employ in this thesis is used to resolve the “amount” of
1585 E_T^{miss} that “belongs” to each hemisphere, and therefore how to impose the transverse
1586 boost onto each of i.e. P_a and P_b from PP . Equivalently, it can be seen as the
1587 resolution of the kinematics of the I_a and I_b objects in the disquark and digluino
1588 decay trees. Recall that at this point, we have already approximated the boost
1589 of the PP frame. The choice we use is to minimize the masses P_a and P_b , while
1590 simultaneously constraining $P_a = P_b$. As is the case in the last step, there is a
1591 straightforward physical interpretation of this choice. In the signal models we are
1592 considering, P_a and P_b are the estimated frames of the squark or gluino pair-produced
1593 as a heavy resonance. We then of course expect $M_{P_a} = M_{P_b}$.

1594 The imposition of the decay trees, with ambiguities resolved through the jigsaw
1595 rules, give a full set of boosts relating the frames of each decay tree. In each frame,
1596 we have estimates for the frame mass and decay angles, which can be used in searches
1597 for new physics. In the next section, we describe the variables that are used in this
1598 thesis in more details.

1599 **7.3 Variables used in the search for zero lepton**

1600 **SUSY**

1601 We describe here the variables used in the search described in ???. These were
1602 reconstructed using the RJR algorithm as just described, using the RestFrames
1603 packages[119]. In these frames, the momenta of all objects placed into that branch
1604 of the decay tree are available (after application of the approximated boost), and in
1605 principle we can calculate any variable of interest such as invariant masses or the
1606 angles between these objects. The truly useful set of variables are highly dependent
1607 on the signal process, and we leave their discussion to the subsequent chapters. It is
1608 useful to understand the philosophy employed in the construction of these variables.

1609 In general, we can split variables useful for searches for new physics into two
1610 categories: *scaleful* and *scaleless* variables. In this search, we will use a set of scaleful
1611 variables called the H variables. The scaleless variables will consists of ratios and
1612 angles. In general, we want to limit the number of scaleful cuts we apply, for two
1613 reasons. Different scaleful variables are often highly correlated, and this of course
1614 limits the utility of additional cuts. Addtionally, selections based on many scaleful
1615 variables often “over-optimize” for particular signal model of interest, especially as
1616 related to the mass difference chosen between the sparticle and the LSP. To avoid
1617 this, each decay tree will only use two scale variables, one of which quantifies the
1618 overall mass scale of the event, and another which acts as a measure of the event

1619 balance.

1620 **Squark and gluino variables**

1621 Taking our general philosophy to a particular case, we here describe the variables
1622 used by the squark and gluino searches. We have a suite of scale variables which we
1623 will call the H variables, and a suite of angles and ratios.

1624 As we have described above, the RJR algorithm gives us access to the masses of
1625 each frame of interest. It maybe seem natural, then, that these variables would be the
1626 most useful for discrimination of the signal from background processes. However, due
1627 to the all hadronic state considered in this thesis, the that can be constructed such
1628 as M_{PP} can be affected by extra QCD radiation, which can promote the background
1629 processes to large scales. The H variables show a resilience to this effect. They
1630 take their name from the commonly used variable H_T , which is the scalar sum of
1631 the visible momentum. However, due to the RJR technique, we can evaluate these
1632 variables in the non-lab frame, including longitudinal information. They are also
1633 constructed with *aggregate* momenta using a similar mass minimization procedure
1634 as we have already described.

We label these variables as $H_{n,m}^F$. The frame from where they are evaluated is denoted F ; practically, this means $F \in \{\text{lab}, PP, P_a, P_b\}$. When the discussion applies to both P_a and P_b , we will write P_i . The subscripts n and m denote the number of visible and invisible vectors considered, respectively. When there are more vectors available than n or m , we add up vectors using the hemisphere (megajet) jigsaw rule until there are n (m) objects.² In the opposite case, where n or m is greater than the number of available objects, one simply considers the available objects. The $H_{n,m}^F$

²Recall that these vectors are constructed by the imposition of the decay tree with the relevant jigsaw rules.

variables are then defined as

$$H_{n,m}^F = \sum_i^n |\vec{p}_{\text{vis},i}^F| + \sum_j^m |\vec{p}_{\text{inv},i}^F|. \quad (7.16)$$

It may not be clear that these variables encode independent information. Fundamentally, this is just an expression of the triangle inequality $\sum |\vec{p}| \geq |\sum \vec{p}|$. The different combinations can then include independent information. The final note on the H variables is that we can also consider purely transverse versions of these variables, which we will denote $H_{T,n,m}^F$. Including this view, it is easy to see how the H variables are extensions of the normal H_T variables, as

$$H_T = H_{T,\infty,0}^{\text{lab}}. \quad (7.17)$$

1635 Although the H variables are interesting in their own right, the true power of the
 1636 RJR technique comes from the construction of scaleless variables with the technique.
 1637 This is because the scaleless ratios and angles are in fact measured in the “right”
 1638 frame, where right here means an approximation of the correct frame. This provides
 1639 a less correlated set of variables than those measured in the lab frame, due to the
 1640 corrections to the disparticle or sparticle system boosts from the RJR technique.

1641 For the search for noncompressed disquark production, we use will use the
 1642 following set of RJR variables.

1643 • $H_{1,1}^{PP}$ - scale variable useful for discrimination against QCD backgrounds and
 1644 used in a similar way to E_T^{miss}

1645 • $H_{T,2,1}^{PP}$ - scale variable providing information on the overall mass scale of the
 1646 event for disquark signal production. We will often call this the *full* scale
 1647 variable.

1648 • $H_{T,1,1}^{PP}/H_{2,1}^{PP}$ - ratio used to prevent imbalanced events where the scale variable
 1649 is dominated by one high p_T jet or high E_T^{miss}

1650 • $p_{PP,z}^{\text{LAB}}/(p_{PP,z}^{\text{LAB}} + H_{T,2,1}^{PP})$ - ratio to used to prevent significant boosts in the
1651 z -direction. $p_{PP,z}^{\text{LAB}}$ is a measure of the total boost of the PP system from the lab
1652 frame

1653 • $p_{T,j2}^{PP}/H_{T,2,1}^{PP}$ - ratio to force the second leading jet in the PP frame to carry a
1654 significant portion of the total scalar sum in that frame. This requirement is
1655 another balance requirement, on the total p_T of that second jet in the PP frame.

1656 First, we note that there is an implicit requirement that each hemisphere has at least
1657 one jet (to even reconstruct the P_a and P_b frames), these variables are implicitly using
1658 two or more jets, as we expect in disquark production. The other important thing
1659 to note is that all of the ratios use the full scale variable as the denominator. This
1660 is sensible, as we expect all of these effects to be scaled with the full scale variable
1661 $H_{T,2,1}^{PP}$. We will see a similar behavior for the gluino regions, with a new full scale
1662 variable.

1663 For the search for noncompressed digluino production, we use will use the following
1664 set of RJR variables. Due to the increased complexity of the event topology with four
1665 jets, there are additional handles we can exploit:

1666 • $H_{1,1}^{PP}$ - same as disquark production

1667 • $H_{T,4,1}^{PP}$ - scale variable providing information on the overall mass scale of the
1668 event for digluino signal production. As before, we often call this the *full* scale
1669 variable. Since this variable allows the jets to be separated in the PP frame, it
1670 is more appropriate for digluino production.

1671 • $H_{T,1,1}^{PP}/H_{4,1}^{PP}$ - ratio used to prevent imbalanced events where the scale variable
1672 is dominated by one high p_T jet or high E_T^{miss}

1673 • $H_{T,4,1}^{PP}/H_{4,1}^{PP}$ - ratio used to measure the fraction of the total scalar sum of the
1674 momentum in the transverse plane. Digluino production is expected to be fairly

- 1675 central
- 1676 • $p_{PP,z}^{\text{LAB}}/(p_{PP,z}^{\text{LAB}} + H_{T,4,1}^{PP})$ - ratio to used to prevent significant boosts in the
1677 z -direction
- 1678 • $\min(p_{T,j2}^{PP}/H_{T,2,1}^{PP})$ - ratio to require the second leading jet in *both* squark-like
1679 hemispheres C_a and C_b to contain a significant portion of *that frame's* momenta.
1680 This is similar to the $p_{T,j2}^{PP}/H_{T,2,1}^{PP}$ disquark discriminator, but applied to both
1681 hemispheres C_a and C_b .
- 1682 • $\max(H_{1,0}^{P_i}/H_{2,0}^{P_i})$ - ratio requiring one jet in each of the P_i to not take too much
1683 of the total momentum of that frame. This ratio is generally a very loose cut.

1684 Compressed variables

1685 As we saw above, the decay tree imposed for compressed spectra is simpler. We do
1686 not attempt to fully reconstruct the details of the system recoiling of the ISR system,
1687 but use a straightforward set of variables in this case. One additional simplification
1688 is that all variables are force to be transverse in this case; we simply do not include
1689 the η/z information of the objects as inputs to the RJR reconstruction. We still use
1690 the philosophy of limiting our scaleful variables to just two. The compressed scenario
1691 uses the following set of RJR variables:

- 1692 • $p_{T,S}^{\text{ISR}}$ - scale variable that is the magnitude of the total transverse momenta of all
1693 jets associated to the ISR system, as evaluated in the CM frame
- 1694 • $R_{\text{ISR}} \equiv p_I^{\vec{C}\text{M}} \cdot p_{T,S}^{\hat{C}\text{M}}/p_{T,S}^{\text{CM}}$ - this ratio is our measurement for the ratio of the LSP
1695 mass to the compressed sparticle mass. These are the values in the CM frame
1696 In compressed cases, this should be large, as this estimates the amount of the
1697 total $\text{CM} \rightarrow S$ boost is carried by the invisible system.
- 1698 • $M_{T,S}$ - the transverse mass of the S system

- 1699 • N_{jet}^V - the number of jets associated to the visible system V
1700 • $\Delta\phi_{ISR,I^-}$ the opening angle between the ISR system and the invisible system
1701 measured in the lab frame. As the invisible system is expected to carry much
1702 of the total S system momentum, this should be large, as we expect the ISR
1703 system to recoil directly opposite the I system in that case.

Title of Chapter 1

1706 This section presents the details of the first search employing RJR variables as
 1707 discriminating variables, as described in ???. We will describe the data and simulation
 1708 samples used, and then define the selections where we search for new SUSY
 1709 phenomena, which we call the *signal regions* (SRs) Afterwards, we describe the
 1710 background estimation techniques used in the analysis. Finally, we discuss the
 1711 treatment of systematic uncertainties, and how we combine them using a likelihood
 1712 method[120].

1713 **8.1 Collision data and simulation samples**

1714 Simulated data is fundamentally important to the ATLAS physics program. Cali-
 1715 brations, measurements, and searches use Monte Carlo (MC) simulations¹to compare
 1716 with collision data. In this thesis, MC samples are used to optimize the signal region
 1717 selections, assist in background estimation, and assess the sensitivity to specific SUSY
 1718 signal models. The details of Monte Carlo production, accuracy, and utility are far
 1719 beyond the scope of this thesis, but we provide a short description here.

1720 The first step is MC *generation*. A program is run which does a matrix-element
 1721 calculation, sometimes with additional corrections, which produces a set of output
 1722 particles from the parton interactions. These output particles are then decayed via
 1723 another (or the same) simulation program. This produces a set of *truth* particles,

¹In jargon, often just called “Monte Carlo” or MC.

1724 which are the output of event generation. The details of which generator to use are
1725 the subject of much discussion, and generally (many) comparisons are made between
1726 them, for different processes of interest. Additionally, differences between generators
1727 are often a starting point for the calculation of systematic uncertainties.

1728 The next step is the *simulation*. The detector response to the truth particles
1729 is simulated, and simulated hits are produced. After simulation, the standard
1730 reconstruction algorithms described previously are run with the simulated hits. This
1731 procedure ensures “as close as possible” treatment of simulation and collision data.

1732 We give a brief description of which samples use which generators; additional
1733 details are available in ??.

1734 **MAKE BETTER** 1735 Signal (digluino and disquark) samples are generated with up to two extra partons in the matrix element using MG5_aMC@NLO 2.2.2 event generator [Alwall:2014hca] interfaced to PYTHIA 8.186 [Sjostrand:2014zea]. The nominal cross-section is taken from an envelope of cross-section predictions using different PDF sets and factorization and renormalization scales, as described in Ref. [Kramer:2012bx], considering only light-flavour quarks (u, d, s, c). For the light-flavour squarks (gluinos) in case of gluino- (squark-) pair production, cross-sections are evaluated assuming masses of 450 TeV. The free parameters are $m_{\tilde{\chi}_1^0}$ and

1742 $m_{\tilde{g}}$ ($m_{\tilde{s}}$) for gluino-pair (squark-pair) production models.

1743 we have a 1744 “grid” of 1745 these signal 1746 models 1747 samples 1748 Boson (W, Z, γ) plus jet events are simulated using different SHERPA generators, with COMIX and OPENLOOPS matrix-element generators[comix, openloops, 121]. Photons are required to have transverse momentum of > 35 GeV. Importantly, the $W(Z)+jet$ events are calculated at NLO while the the $\gamma+jet$ events are calculated at LO. The $W/Z + jets$ events are normalized to their NNLO cross-sections

1749 [Catani:2009sm]. The $\gamma+jets$ LO cross-section is taken directly from SHERPA; we will apply a correction factor to be described later.

1750 The various $t\bar{t}$ and single-top processes[122] are generated using two versions of

1751 POWHEG-Box [[powheg-box](#), [122](#)]. These are calculated at NLO and normalized
1752 to various orders ranging from NLO to NNLO+NNLL in the different processes,
1753 which can be seen in [8.1](#)[[Czakon:2013goa](#), [Czakon:2011xx](#), [Aliev:2010zk](#),
1754 [Kant:2014oha](#), [Kidonakis:2010ux](#), [Kidonakis:2011wy](#)].

1755 Diboson processes (WW , WZ , ZZ) [[123](#)] are simulated using the SHERPA 2.1.1
1756 generator. For processes with four charged leptons (4ℓ), three charged leptons and
1757 a neutrino ($3\ell+1\nu$) or two charged leptons and two neutrinos ($2\ell+2\nu$), the matrix
1758 elements contain all diagrams with four electroweak vertices, and are calculated for
1759 up to one (4ℓ , $2\ell+2\nu$) or no partons ($3\ell+1\nu$) at NLO and up to three partons at LO
1760 using the COMIX and OPENLOOPS matrix-element generators, and merged with the
1761 SHERPA parton shower using the ME+PS@NLO prescription. For processes in which
1762 one of the bosons decays hadronically and the other leptonically, matrix elements
1763 are calculated for up to one (ZZ) or no (WW , WZ) additional partons at NLO
1764 and for up to three additional partons at LO using the COMIX and OPENLOOPS
1765 matrix-element generators, and merged with the SHERPA parton shower using the
1766 ME+PS@NLO prescription. In all cases, the CT10 PDF set is used in conjunction
1767 with a dedicated parton-shower tuning developed by the authors of SHERPA. The
1768 generator cross-sections are used in this case.

1769 The multi-jet background is generated with PYTHIA 8.186 using the A14
1770 underlying-event tune and the NNPDF2.3LO parton distribution functions.

1771 A summary of the SM background processes together with the MC generators,
1772 cross-section calculation orders in α_s , PDFs, parton shower and tunes used is given
1773 in Table [8.1](#).

Physics process	Generator	Cross-section normalization	PDF set	Parton shower	Tune
$W(\rightarrow \ell\nu) + \text{jets}$	SHERPA 2.2.0	NNLO	NNPDF3.0NNLO	SHERPA	SHERPA default
$Z/\gamma^*(\rightarrow \ell\bar{\ell}) + \text{jets}$	SHERPA 2.2.0	NNLO	NNPDF3.0NNLO	SHERPA	SHERPA default
$\gamma + \text{jets}$	SHERPA 2.1.1	LO	CT10	SHERPA	SHERPA default
$t\bar{t}$	Powheg-Box v2	NNLO+NNLL	CT10	PYTHIA 6.428	PERUGIA2012
Single top (Wt -channel)	Powheg-Box v2	NNLO+NNLL	CT10	PYTHIA 6.428	PERUGIA2012
Single top (s -channel)	Powheg-Box v2	NLO	CT10	PYTHIA 6.428	PERUGIA2012
Single top (t -channel)	Powheg-Box v1	NLO	CT10f4	PYTHIA 6.428	PERUGIA2012
$t\bar{t} + W/Z/WW$	MG5_aMC@NLO 2.2.3	NLO	NNPDF2.3LO	PYTHIA 8.186	A14
WW, WZ, ZZ	SHERPA 2.1.1	NLO	CT10	SHERPA	SHERPA default
Multi-jet	PYTHIA 8.186	LO	NNPDF2.3LO	PYTHIA 8.186	A14

Table 8.1: The Standard Model background Monte Carlo simulation samples used in this thesis. The generators, the order in α_s of cross-section calculations used for yield normalization, PDF sets, parton showers and tunes used for the underlying event are shown.

1774 For all SM background samples the response of the detector to particles is
 1775 modelled with a full ATLAS detector simulation [**:2010wqa**] based on GEANT4
 1776 [**Agostinelli:2002hh**]. Signal samples are prepared using a fast simulation based on
 1777 a parameterization of the performance of the ATLAS electromagnetic and hadronic
 1778 calorimeters [**ATLAS:2010bfa**] and on GEANT4 elsewhere.

1779 All simulated events are overlaid with multiple pp collisions simulated with
 1780 the soft QCD processes of PYTHIA 8.186 using the A2 tune [**A14tune**] and the
 1781 MSTW2008LO parton distribution functions [**Martin:2009iq**]. The simulations are
 1782 reweighted to match the distribution of the mean number of interactions observed in
 1783 data.

1784 8.2 Event selection

1785 This section describes the selection of events. We begin by describing the *preselection*,
1786 which is used to remove problematic events and reduce the dataset to a manageable
1787 size. We then describe the signal region strategy, and present the signal regions used
1788 in the analysis.

1789 Preselection

1790 The preselection is used to reduce the dataset to that of interest in this thesis. The
1791 table containing the preselection cuts is shown in 8.2. This selection is also used for
1792 the samples used for background estimation, except for the lepton veto.

1793 The cuts [1] and [4] are a set of cleaning cuts to remove problematic events.
1794 The *Good Runs List* is a centrally-maintained list of data runs which have been
1795 determined to be “good for physics”. This determination is made by analysis of the
1796 various subdetectors, and monitoring of their status. Event cleaning is used to veto
1797 events which could be affected by noncollision background, noise bursts, or cosmic
1798 rays.

1799 We require the lowest unprescaled E_T^{miss} trigger for the data run of interest, as
1800 described previously, in cut [2]. The lepton veto is applied in cut [5]. These two cuts
1801 are only used for the signal region selection.

1802 The rest of the preselection is used for the signal region and background estimation
1803 samples. These cuts are mostly used for the reduction of the dataset to a manageable
1804 Signal models with sensitivity to lower values of these scale variables have been ruled
1805 out by previous searches . The final cut is on m_{eff} , which is the scalar sum of all jets cite
1806 and E_T^{miss} . This is the final discriminating variable used in the complementary search
1807 to this thesis, which is also presented in ??.

Cut	Description	
1	Good Runs List	Veto events with intolerable detector errors
2	Trigger	HLT_xe70 (2015), HLT_xe80_tclcw_L1XE50, or HLT_xe100_mht_L1XE50 (2016)
3	Event cleaning	Veto for noncollision background, noise bursts, and cosmic rays
4	Lepton veto	No leptons with $p_T > 10$ GeV after overlap removal
5	E_T^{miss} [GeV] >	250
6	$p_T(j_1)$ [GeV] >	200
7	$p_T(j_2)$ [GeV] >	50
8	m_{eff} [GeV] >	800

Table 8.2: Preselection for the various event topologies used in the analysis.

1808 Signal regions

1809 We define a set of signal regions using the RJR variables previously described.
 1810 These signal regions are split into three general categories: squark pair production
 1811 SRs, gluino pair production SRs, and compressed production SRs. Within these
 1812 general SRs, we have a set of signal regions targetting different mass splittings of the
 1813 sparticle and LSP.

1814 A schematic of this strategy is shown in ???. This type of plane is how most
 1815 ($R-$ parity conserving) SUSY searches are organized in both ATLAS and CMS. The
 1816 horizontal axis is the mass of the sparticle considered. In the case of this thesis,
 1817 this will be the squark or gluino mass. On the horizontal axis, we place the LSP mass.
 1818 These are the two free parameters of the simplified models considered here. Our
 1819 search occurs in this two-parameter space. Each signal region targets some portion
 1820 of this plane. As shown in the figure, a new iteration of a search will use a set of
 1821 signal regions which have sensitivity just beyond those of the previous exclusions.
 1822 The choice of how many signal regions to use to fully cover this plane is in many
 1823 ways a matter of judgment, as it is essentially a matter of under/over-fitting to the
 1824 signal models of interest. One signal region will obscure the different phenomena in

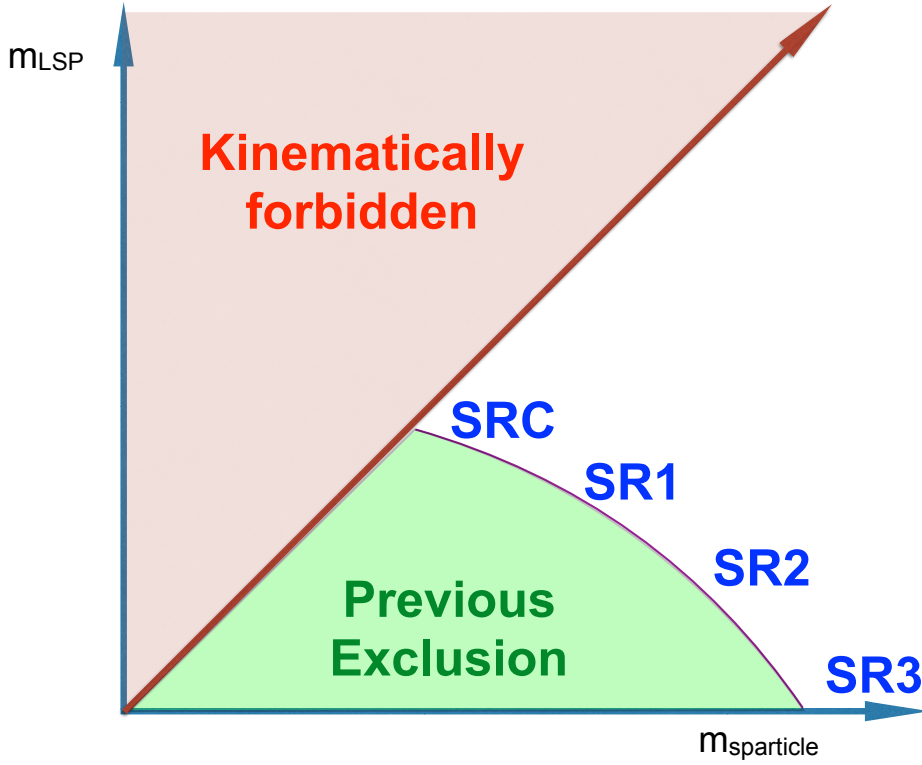


Figure 8.1: Schematic leading the development of the SUSY signal regions in this thesis. A variant of this schematic is used for most SUSY searches on ATLAS and CMS.

1825 signal events with large versus small mass splittings, leading to underfitting. Binning
 1826 as finely as possible² leads to overfitting due to the fluctuations present in the signal
 1827 and background events passing this selection. In this thesis, we use six squark signal
 1828 regions, six gluino signal regions, and five compressed regions, which we describe
 1829 below.

1830 The full table defining all signal regions is shown in 8.3. In all cases, the signal
 1831 region selections contain a combination of scaleful and scaleless cuts. Emphasis
 1832 on cuts on scaleful variables provide stronger sensitivity to larger mass splittings,
 1833 while additional sensitivity to smaller mass splittings is found using stronger cuts on
 1834 scaleless variables. One envisions walking from SR1 (with tight scaleless cuts and

²This can be defined as having a signal region for each simulated signal sample, which for this analysis is ~ 100 .

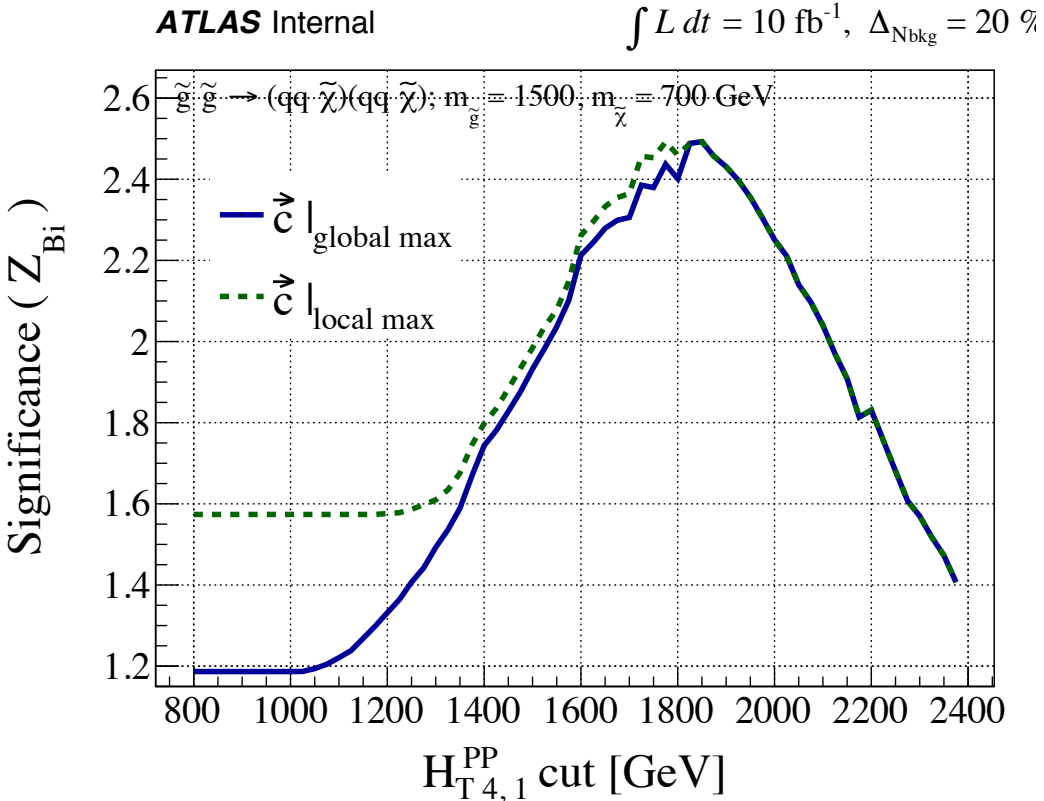


Figure 8.2: Optimization of the $H_{T,4,1}^{PP}$ cut for a gluino signal model with $(m_{\tilde{g}}, m_{\tilde{\chi}_1^0}) = (1500, 700)$ GeV assuming 10 fb^{-1} and an uncertainty of 20% on the background estimate.

1835 loose scaleful cuts) in 8.1 towards SR3 by loosening the scaleless cuts and tightening
 1836 the scaleful cuts. We will see this strategy at work in each set of signal regions.

1837 We have already described the useful variables in the previous chapter. The
 1838 question is how to choose the optimal cuts for a given set of signal models, which are
 1839 grouped in the mass splitting space. This was done by a brute force scan over the
 1840 cut values, using a guess of integrated luminosity with a fixed systematic uncertainty
 1841 scenario, motivated by that from previous analyses. We choose the lowest cut value
 1842 that maximizes the Z_{Bi} , as described in [124]. This figure of merit gives conservative
 1843 estimates, as compared to i.e. S/\sqrt{B} . A figure showing an example of this selection
 1844 tuning procedure is shown in 8.2.

1845 The compressed selections are split into five regions (SRC1-5), and due to the

1846 simplified nature of the compressed decay tree, has sensitivity in both the gluino
1847 and squark planes. The compressed regions target mass splittings with $m_{\text{sparticle}} -$
1848 $m_{\text{LSP}} \tilde{<} 200 \text{ GeV}$. For the compressed region, $M_{T,S}$ is the primary scaleful variable.
1849 We can see the general strategy of lowering increasing scale cuts while decreasing the
1850 scaleless cuts here. SRC1 targets the most compressed scenarios, with mass splittings
1851 of less than 25 GeV, and has the loosest $M_{T,S}$ cut coupled with the tightest R_{ISR} and
1852 $\Delta\phi_{\text{ISR},I}$ cuts. SRC4 and SRC5 target mass splittings of ~ 200 GeV, and are coupled
1853 with the loosest scaleless cuts on R_{ISR} and $\Delta\phi_{\text{ISR},I}$. We also note that SRC4 and
1854 SRC5 have differing cuts on N_{jet}^V , since these SRs are closest to the regions we will
1855 describe below, and can be seen as the “cross-over” where the differences between
1856 squark and gluino production begins to become manifest.

1857 The squark regions (for noncompressed spectra) are organized into six signal
1858 regions. The SRS1 regions are targer

1859 The selection

Targeted signal	$\tilde{s}\tilde{s}, \tilde{s} \rightarrow q\tilde{\chi}_1^0$									
Requirement	Signal Region									
	RJR-S1		RJR-S2		RJR-S3					
$H_{1,1}^{PP}/H_{2,1}^{PP} \geq$	0.6		0.55		0.5					
$H_{1,1}^{PP}/H_{2,1}^{PP} \leq$	0.95		0.96		0.98					
$p_{PP, z}^{lab}/(p_{PP, z}^{lab} + H_{T, 2,1}^{PP}) \leq$	0.5		0.55		0.6					
$p_{j2, T}^{PP}/H_{T, 2,1}^{PP} \geq$	0.16		0.15		0.13					
$\Delta_{QCD} >$	0.001									
	RJR-S1a	RJR-S1b	RJR-S2a	RJR-S2b	RJR-S3a	RJR-S3b				
$H_{T, 2,1}^{PP} [\text{GeV}] >$	1000	1200	1400	1600	1800	2000				
$H_{1,1}^{PP} [\text{GeV}] >$	1000		1400		1600					
Targeted signal	$\tilde{g}\tilde{g}, \tilde{g} \rightarrow q\bar{q}\tilde{\chi}_1^0$									
Requirement	Signal Region									
	RJR-G1		RJR-G2		RJR-G3					
$H_{1,1}^{PP}/H_{4,1}^{PP} \geq$	0.35		0.25		0.2					
$H_{T, 4,1}^{PP}/H_{4,1}^{PP} \geq$	0.8		0.75		0.65					
$p_{PP, z}^{lab}/(p_{PP, z}^{lab} + H_{T, 4,1}^{PP}) \leq$	0.5		0.55		0.6					
$\min(p_{j2, T}^{PP}/H_{T, 2,1}^{PP}) \geq$	0.12		0.1		0.08					
$\max(H_{1,0}^{Pi}/H_{2,0}^{Pi}) \leq$	0.95		0.97		0.98					
$ \frac{2}{3}\Delta\phi_{V,P}^{PP} - \frac{1}{3}\cos\theta_p \leq$	0.5		-							
$\Delta_{QCD} >$	0									
	RJR-G1a	RJR-G1b	RJR-G2a	RJR-G2b	RJR-G3a	RJR-G3b				
$H_{T, 4,1}^{PP} [\text{GeV}] >$	1000	1200	1500	1900	2300	2800				
$H_{1,1}^{PP} [\text{GeV}] >$	600		800		900					
Targeted signal	compressed spectra in $\tilde{s}\tilde{s}$ ($\tilde{s} \rightarrow q\tilde{\chi}_1^0$); $\tilde{g}\tilde{g}$ ($\tilde{g} \rightarrow q\bar{q}\tilde{\chi}_1^0$)									
Requirement	Signal Region									
	RJR-C1	RJR-C2	RJR-C3	RJR-C4	RJR-C5					
$R_{ISR} \geq$	0.9	0.85	0.8	0.75	0.70					
$\Delta\phi_{ISR, I} \geq$	3.1	3.07	2.95	2.95	2.95					
$\Delta\phi(\text{jet}_{1,2}, \mathbf{E}_T^{\text{miss}})_{\text{min}}$	-	-	-	0.4	0.4					
$M_{TS} [\text{GeV}] \geq$	100	100	200	500	500					
$p_{TS}^{CM} [\text{GeV}] \geq$	800	800	600	600	600					
$N_{jet}^V \geq$	1	1	2	2	3					

Table 8.3: Selection criteria and targeted signal model used to define signal regions in the RJR-based search, indicated by the prefix ‘RJR’. Each SR is labelled with the targeted SUSY particle or the targeted region of parameter space, such that ‘S’, ‘G’ and ‘C’ denote regions searching for squark-, gluino-pair production, or compressed spectra, respectively.

1860 **8.3 Background estimation**

1861 **Control and Validation Regions**

1862 CRT,CRW,CRY,CRQ

1863 **R Z/ γ method**

1864 **Systematic Uncertainties**

1865

Chapter 9

1866

Title of Chapter 1

1867 Here you can write some introductory remarks about your chapter. I like to give each
1868 sentence its own line.

1869 When you need a new paragraph, just skip an extra line.

1870 **9.1 Statistical Analysis**

1871 maybe to be moved to an appendix

1872 **9.2 Signal Region distributions**

1873 **9.3 Pull Plots**

1874 **9.4 Exclusion plots**

1875

Conclusion

1876 Here you can write some introductory remarks about your chapter. I like to give each
1877 sentence its own line.

1878 When you need a new paragraph, just skip an extra line.

1879 **9.5 New Section**

1880 By using the asterisk to start a new section, I keep the section from appearing in the
1881 table of contents. If you want your sections to be numbered and to appear in the
1882 table of contents, remove the asterisk.

Bibliography

- 1884 [1] O. Perdereau, *Planck 2015 cosmological results*,
1885 *AIP Conf. Proc.* **1743** (2016) p. 050014.
- 1886 [2] N. Aghanim et al.,
1887 *Planck 2016 intermediate results. LI. Features in the cosmic microwave*
1888 *background temperature power spectrum and shifts in cosmological parameters*
1889 (2016), arXiv: [1608.02487 \[astro-ph.CO\]](https://arxiv.org/abs/1608.02487).
- 1890 [3] J. S. Schwinger,
1891 *On Quantum electrodynamics and the magnetic moment of the electron*,
1892 *Phys. Rev.* **73** (1948) p. 416.
- 1893 [4] S. Laporta and E. Remiddi,
1894 *The Analytical value of the electron (g-2) at order alpha**3 in QED*,
1895 *Phys. Lett.* **B379** (1996) p. 283, arXiv: [hep-ph/9602417 \[hep-ph\]](https://arxiv.org/abs/hep-ph/9602417).
- 1896 [5] S. Schael et al., *Precision electroweak measurements on the Z resonance*,
1897 *Phys. Rept.* **427** (2006) p. 257, arXiv: [hep-ex/0509008 \[hep-ex\]](https://arxiv.org/abs/hep-ex/0509008).
- 1898 [6] S. L. Glashow, *Partial Symmetries of Weak Interactions*,
1899 *Nucl. Phys.* **22** (1961) p. 579.
- 1900 [7] S. Weinberg, *A Model of Leptons*, *Phys. Rev. Lett.* **19** (1967) p. 1264.
- 1901 [8] A. Salam, *Weak and Electromagnetic Interactions*,
1902 *Conf. Proc.* **C680519** (1968) p. 367.
- 1903 [9] M. Gell-Mann, *A Schematic Model of Baryons and Mesons*,
1904 *Phys. Lett.* **8** (1964) p. 214.
- 1905 [10] G. Zweig, “An SU(3) model for strong interaction symmetry and its
1906 breaking. Version 2,” *DEVELOPMENTS IN THE QUARK THEORY OF*
1907 *HADRONS. VOL. 1. 1964 - 1978*, ed. by D. Lichtenberg and S. P. Rosen,
1908 1964 p. 22,
1909 URL: <http://inspirehep.net/record/4674/files/cern-th-412.pdf>.

- 1910 [11] S. Weinberg, *Implications of Dynamical Symmetry Breaking*,
1911 Phys. Rev. **D13** (1976) p. 974.
- 1912 [12] S. Weinberg, *Implications of Dynamical Symmetry Breaking: An Addendum*,
1913 Phys. Rev. **D19** (1979) p. 1277.
- 1914 [13] E. Gildener, *Gauge Symmetry Hierarchies*, Phys. Rev. **D14** (1976) p. 1667.
- 1915 [14] L. Susskind, *Dynamics of Spontaneous Symmetry Breaking in the*
1916 *Weinberg-Salam Theory*, Phys. Rev. **D20** (1979) p. 2619.
- 1917 [15] S. P. Martin, “A Supersymmetry Primer,” 1997,
1918 eprint: [arXiv:hep-ph/9709356](https://arxiv.org/abs/hep-ph/9709356).
- 1919 [16] V. C. Rubin and W. K. Ford Jr., *Rotation of the Andromeda Nebula from a*
1920 *Spectroscopic Survey of Emission Regions*, Astrophys. J. **159** (1970) p. 379.
- 1921 [17] M. S. Roberts and R. N. Whitehurst,
1922 “*The rotation curve and geometry of M31 at large galactocentric distances*,
1923 Astrophys. J. **201** (1970) p. 327.
- 1924 [18] V. C. Rubin, N. Thonnard, and W. K. Ford Jr.,
1925 *Rotational properties of 21 SC galaxies with a large range of luminosities and*
1926 *radii, from NGC 4605 /R = 4kpc/ to UGC 2885 /R = 122 kpc/*,
1927 Astrophys. J. **238** (1980) p. 471.
- 1928 [19] V. C. Rubin et al., *Rotation velocities of 16 SA galaxies and a comparison of*
1929 *Sa, Sb, and SC rotation properties*, Astrophys. J. **289** (1985) p. 81.
- 1930 [20] A. Bosma,
1931 *21-cm line studies of spiral galaxies. 2. The distribution and kinematics of*
1932 *neutral hydrogen in spiral galaxies of various morphological types.*,
1933 Astron. J. **86** (1981) p. 1825.
- 1934 [21] M. Persic, P. Salucci, and F. Stel, *The Universal rotation curve of spiral*
1935 *galaxies: 1. The Dark matter connection*,
1936 Mon. Not. Roy. Astron. Soc. **281** (1996) p. 27,
1937 arXiv: [astro-ph/9506004](https://arxiv.org/abs/astro-ph/9506004) [astro-ph].
- 1938 [22] M. Lisanti, “Lectures on Dark Matter Physics,” 2016,
1939 eprint: [arXiv:1603.03797](https://arxiv.org/abs/1603.03797).
- 1940 [23] H. Miyazawa, *Baryon Number Changing Currents*,
1941 Prog. Theor. Phys. **36** (1966) p. 1266.

- 1942 [24] J.-L. Gervais and B. Sakita, *Generalizations of dual models*,
 1943 *Nucl. Phys.* **B34** (1971) p. 477.
- 1944 [25] J.-L. Gervais and B. Sakita,
 1945 *Field Theory Interpretation of Supergauges in Dual Models*,
 1946 *Nucl. Phys.* **B34** (1971) p. 632.
- 1947 [26] Yu. A. Golfand and E. P. Likhtman, *Extension of the Algebra of Poincare
 1948 Group Generators and Violation of p Invariance*,
 1949 *JETP Lett.* **13** (1971) p. 323, [*Pisma Zh. Eksp. Teor. Fiz.* **13**, 452 (1971)].
- 1950 [27] A. Neveu and J. H. Schwarz, *Factorizable dual model of pions*,
 1951 *Nucl. Phys.* **B31** (1971) p. 86.
- 1952 [28] A. Neveu and J. H. Schwarz, *Quark Model of Dual Pions*,
 1953 *Phys. Rev.* **D4** (1971) p. 1109.
- 1954 [29] D. V. Volkov and V. P. Akulov, *Is the Neutrino a Goldstone Particle?*
 1955 *Phys. Lett.* **B46** (1973) p. 109.
- 1956 [30] J. Wess and B. Zumino,
 1957 *A Lagrangian Model Invariant Under Supergauge Transformations*,
 1958 *Phys. Lett.* **B49** (1974) p. 52.
- 1959 [31] A. Salam and J. A. Strathdee, *Supersymmetry and Nonabelian Gauges*,
 1960 *Phys. Lett.* **B51** (1974) p. 353.
- 1961 [32] S. Ferrara, J. Wess, and B. Zumino, *Supergauge Multiplets and Superfields*,
 1962 *Phys. Lett.* **B51** (1974) p. 239.
- 1963 [33] J. Wess and B. Zumino, *Supergauge Transformations in Four-Dimensions*,
 1964 *Nucl. Phys.* **B70** (1974) p. 39.
- 1965 [34] J. D. Lykken, “Introduction to supersymmetry,” *Fields, strings and duality. Proceedings, Summer School, Theoretical Advanced Study Institute in Elementary Particle Physics, TASI’96, Boulder, USA, June 2-28, 1996*, 1996
 1966 p. 85, arXiv: [hep-th/9612114](https://arxiv.org/abs/hep-th/9612114) [hep-th],
 1968 URL: http://lss.fnal.gov/cgi-bin/find_paper.pl?pub=96-445-T.
- 1970 [35] A. Kobakhidze, “Intro to SUSY,” 2016, URL: <https://indico.cern.ch/event/443176/page/5225-pre-susy-programme>.
- 1972 [36] G. R. Farrar and P. Fayet, *Phenomenology of the Production, Decay, and
 1973 Detection of New Hadronic States Associated with Supersymmetry*,
 1974 *Phys. Lett.* **B76** (1978) p. 575.

- 1975 [37] ATLAS Collaboration, *Search for the electroweak production of supersymmetric particles in*
 1976 *$\sqrt{s} = 8 \text{ TeV}$ pp collisions with the ATLAS detector,*
 1977 *Phys. Rev. D* **93** (2016) p. 052002, arXiv: [1509.07152 \[hep-ex\]](#).
- 1979 [38] ATLAS Collaboration, *Summary of the searches for squarks and gluinos using $\sqrt{s} = 8 \text{ TeV}$ pp collisions with the ATLAS experiment at the LHC*,
 1980 *JHEP* **10** (2015) p. 054, arXiv: [1507.05525 \[hep-ex\]](#).
- 1982 [39] ATLAS Collaboration, *ATLAS Run 1 searches for direct pair production of third-generation squarks at the Large Hadron Collider*,
 1983 *Eur. Phys. J. C* **75** (2015) p. 510, arXiv: [1506.08616 \[hep-ex\]](#).
- 1985 [40] CMS Collaboration, *Search for supersymmetry with razor variables in pp collisions at $\sqrt{s} = 7 \text{ TeV}$* , *Phys. Rev. D* **90** (2014) p. 112001,
 1986 arXiv: [1405.3961 \[hep-ex\]](#).
- 1988 [41] CMS Collaboration, *Inclusive search for supersymmetry using razor variables in pp collisions at $\sqrt{s} = 7 \text{ TeV}$* , *Phys. Rev. Lett.* **111** (2013) p. 081802,
 1989 arXiv: [1212.6961 \[hep-ex\]](#).
- 1991 [42] CMS Collaboration, *Search for Supersymmetry in pp Collisions at 7 TeV in Events with Jets and Missing Transverse Energy*,
 1992 *Phys. Lett. B* **698** (2011) p. 196, arXiv: [1101.1628 \[hep-ex\]](#).
- 1994 [43] CMS Collaboration, *Search for Supersymmetry at the LHC in Events with Jets and Missing Transverse Energy*, *Phys. Rev. Lett.* **107** (2011) p. 221804,
 1995 arXiv: [1109.2352 \[hep-ex\]](#).
- 1997 [44] CMS Collaboration, *Search for supersymmetry in hadronic final states using M_{T2} in pp collisions at $\sqrt{s} = 7 \text{ TeV}$* , *JHEP* **10** (2012) p. 018,
 1998 arXiv: [1207.1798 \[hep-ex\]](#).
- 2000 [45] CMS Collaboration, *Searches for supersymmetry using the M_{T2} variable in hadronic events produced in pp collisions at 8 TeV*, *JHEP* **05** (2015) p. 078,
 2001 arXiv: [1502.04358 \[hep-ex\]](#).
- 2003 [46] CMS Collaboration, *Search for new physics with the M_{T2} variable in all-jets final states produced in pp collisions at $\sqrt{s} = 13 \text{ TeV}$* , *JHEP* (2016),
 2004 arXiv: [1603.04053 \[hep-ex\]](#).
- 2006 [47] ATLAS Collaboration, *Multi-channel search for squarks and gluinos in $\sqrt{s} = 7 \text{ TeV}$ pp collisions with the ATLAS detector at the LHC*,
 2007 *Eur. Phys. J. C* **73** (2013) p. 2362, arXiv: [1212.6149 \[hep-ex\]](#).

- 2009 [48] Y. Grossman, “Introduction to the SM,” 2016, URL: <https://indico.fnal.gov/sessionDisplay.py?sessionId=3&confId=11505#20160811>.
- 2010
- 2011 [49] W Buchmuller and C Ludeling, *Field Theory and Standard Model* (Sept. 2006) p. 70, URL: <https://cds.cern.ch/record/984122>.
- 2012
- 2013 [50] P. W. Higgs, *Broken Symmetries and the Masses of Gauge Bosons*, Phys. Rev. Lett. **13** (1964) p. 508.
- 2014
- 2015 [51] ATLAS Collaboration, *Observation of a new particle in the search for the Standard Model Higgs boson with the ATLAS detector at the LHC*, Phys. Lett. B **716** (2012) p. 1, arXiv: [1207.7214 \[hep-ex\]](https://arxiv.org/abs/1207.7214).
- 2016
- 2017
- 2018 [52] CMS Collaboration, *Observation of a new boson at a mass of 125 GeV with the CMS experiment at the LHC*, Phys. Lett. B **716** (2012) p. 30, arXiv: [1207.7235 \[hep-ex\]](https://arxiv.org/abs/1207.7235).
- 2019
- 2020
- 2021 [53] A. Chodos et al., *A New Extended Model of Hadrons*, Phys. Rev. **D9** (1974) p. 3471.
- 2022
- 2023 [54] A. Chodos et al., *Baryon Structure in the Bag Theory*, Phys. Rev. **D10** (1974) p. 2599.
- 2024
- 2025 [55] J. C. Collins, D. E. Soper, and G. F. Sterman, *Factorization of Hard Processes in QCD*, Adv. Ser. Direct. High Energy Phys. **5** (1989) p. 1, arXiv: [hep-ph/0409313 \[hep-ph\]](https://arxiv.org/abs/hep-ph/0409313).
- 2026
- 2027
- 2028
- 2029 [56] K. A. Olive et al., *Review of Particle Physics*, Chin. Phys. **C38** (2014) p. 090001.
- 2030
- 2031 [57] N. Cabibbo, *Unitary Symmetry and Leptonic Decays*, Phys. Rev. Lett. **10** (1963) p. 531, [[648\(1963\)](#)].
- 2032
- 2033 [58] M. Kobayashi and T. Maskawa, *CP Violation in the Renormalizable Theory of Weak Interaction*, Prog. Theor. Phys. **49** (1973) p. 652.
- 2034
- 2035
- 2036 [59] W. F. L. Hollik, *Radiative Corrections in the Standard Model and their Role for Precision Tests of the Electroweak Theory*, Fortsch. Phys. **38** (1990) p. 165.
- 2037
- 2038
- 2039 [60] D. Yu. Bardin et al., *ELECTROWEAK RADIATIVE CORRECTIONS TO DEEP INELASTIC*
- 2040

- 2041 *SCATTERING AT HERA! CHARGED CURRENT SCATTERING,*
 2042 *Z. Phys. C***44** (1989) p. 149.
- 2043 [61] D. C. Kennedy et al.,
 2044 *Electroweak Cross-Sections and Asymmetries at the Z0,*
 2045 *Nucl. Phys. B***321** (1989) p. 83.
- 2046 [62] A. Sirlin, *Radiative Corrections in the SU(2)-L x U(1) Theory: A Simple*
 2047 *Renormalization Framework*, *Phys. Rev. D***22** (1980) p. 971.
- 2048 [63] S. Fanchiotti, B. A. Kniehl, and A. Sirlin,
 2049 *Incorporation of QCD effects in basic corrections of the electroweak theory*,
 2050 *Phys. Rev. D***48** (1993) p. 307, arXiv: [hep-ph/9212285 \[hep-ph\]](#).
- 2051 [64] C. Quigg, “Cosmic Neutrinos,” *Proceedings, 35th SLAC Summer Institute on*
 2052 *Particle Physics: Dark matter: From the cosmos to the Laboratory (SSI*
 2053 *2007): Menlo Park, California, July 30- August 10, 2007*, 2008,
 2054 arXiv: [0802.0013 \[hep-ph\]](#),
 2055 URL: http://lss.fnal.gov/cgi-bin/find_paper.pl?conf-07-417.
- 2056 [65] S. R. Coleman and J. Mandula, *All Possible Symmetries of the S Matrix*,
 2057 *Phys. Rev. 159* (1967) p. 1251.
- 2058 [66] R. Haag, J. T. Lopuszanski, and M. Sohnius,
 2059 *All Possible Generators of Supersymmetries of the s Matrix*,
 2060 *Nucl. Phys. B***88** (1975) p. 257.
- 2061 [67] A. Salam and J. A. Strathdee, *On Superfields and Fermi-Bose Symmetry*,
 2062 *Phys. Rev. D***11** (1975) p. 1521.
- 2063 [68] S. Dimopoulos and H. Georgi, *Softly Broken Supersymmetry and SU(5)*,
 2064 *Nucl. Phys. B***193** (1981) p. 150.
- 2065 [69] S. Dimopoulos, S. Raby, and F. Wilczek,
 2066 *Supersymmetry and the Scale of Unification*, *Phys. Rev. D***24** (1981) p. 1681.
- 2067 [70] L. E. Ibanez and G. G. Ross,
 2068 *Low-Energy Predictions in Supersymmetric Grand Unified Theories*,
 2069 *Phys. Lett. B***105** (1981) p. 439.
- 2070 [71] W. J. Marciano and G. Senjanovic,
 2071 *Predictions of Supersymmetric Grand Unified Theories*,
 2072 *Phys. Rev. D***25** (1982) p. 3092.

- 2073 [72] L. Girardello and M. T. Grisaru, *Soft Breaking of Supersymmetry*,
 2074 *Nucl. Phys.* **B194** (1982) p. 65.
- 2075 [73] D. J. H. Chung et al.,
 2076 *The Soft supersymmetry breaking Lagrangian: Theory and applications*,
 2077 *Phys. Rept.* **407** (2005) p. 1, arXiv: [hep-ph/0312378 \[hep-ph\]](#).
- 2078 [74] J. Hisano et al., *Lepton flavor violation in the supersymmetric standard*
 2079 *model with seesaw induced neutrino masses*, *Phys. Lett.* **B357** (1995) p. 579,
 2080 arXiv: [hep-ph/9501407 \[hep-ph\]](#).
- 2081 [75] F. Gabbiani et al., *A Complete analysis of FCNC and CP constraints in*
 2082 *general SUSY extensions of the standard model*,
 2083 *Nucl. Phys.* **B477** (1996) p. 321, arXiv: [hep-ph/9604387 \[hep-ph\]](#).
- 2084 [76] F. Gabbiani and A. Masiero,
 2085 *FCNC in Generalized Supersymmetric Theories*,
 2086 *Nucl. Phys.* **B322** (1989) p. 235.
- 2087 [77] J. S. Hagelin, S. Kelley, and T. Tanaka, *Supersymmetric flavor changing*
 2088 *neutral currents: Exact amplitudes and phenomenological analysis*,
 2089 *Nucl. Phys.* **B415** (1994) p. 293.
- 2090 [78] J. S. Hagelin, S. Kelley, and V. Ziegler, *Using gauge coupling unification and*
 2091 *proton decay to test minimal supersymmetric SU(5)*,
 2092 *Phys. Lett.* **B342** (1995) p. 145, arXiv: [hep-ph/9406366 \[hep-ph\]](#).
- 2093 [79] D. Choudhury et al.,
 2094 *Constraints on nonuniversal soft terms from flavor changing neutral currents*,
 2095 *Phys. Lett.* **B342** (1995) p. 180, arXiv: [hep-ph/9408275 \[hep-ph\]](#).
- 2096 [80] R. Barbieri and L. J. Hall, *Signals for supersymmetric unification*,
 2097 *Phys. Lett.* **B338** (1994) p. 212, arXiv: [hep-ph/9408406 \[hep-ph\]](#).
- 2098 [81] B. de Carlos, J. A. Casas, and J. M. Moreno,
 2099 *Constraints on supersymmetric theories from mu —> e gamma*,
 2100 *Phys. Rev.* **D53** (1996) p. 6398, arXiv: [hep-ph/9507377 \[hep-ph\]](#).
- 2101 [82] J. A. Casas and S. Dimopoulos,
 2102 *Stability bounds on flavor violating trilinear soft terms in the MSSM*,
 2103 *Phys. Lett.* **B387** (1996) p. 107, arXiv: [hep-ph/9606237 \[hep-ph\]](#).
- 2104 [83] C. Borschensky et al., *Squark and gluino production cross sections in pp*
 2105 *collisions at $\sqrt{s} = 13, 14, 33$ and 100 TeV*,
 2106 *Eur. Phys. J.* **C74** (2014) p. 3174, arXiv: [1407.5066 \[hep-ph\]](#).

- 2107 [84] M. Klasen, M. Pohl, and G. Sigl, *Indirect and direct search for dark matter*,
2108 Prog. Part. Nucl. Phys. **85** (2015) p. 1, arXiv: [1507.03800](https://arxiv.org/abs/1507.03800) [hep-ph].
- 2109 [85] L. Evans and P. Bryant, *LHC Machine*, JINST **3** (2008) S08001.
- 2110 [86] Vladimir Shiltsev, “Accelerator Physics and Technology,” Aug. 2016,
2111 URL: [https://indico.fnal.gov/sessionDisplay.py?sessionId=3&](https://indico.fnal.gov/sessionDisplay.py?sessionId=3&confId=11505#20160811)
2112 [confId=11505#20160811](https://indico.fnal.gov/sessionDisplay.py?sessionId=3&confId=11505#20160811).
- 2113 [87] *LEP design report*, Copies shelved as reports in LEP, PS and SPS libraries,
2114 Geneva: CERN, 1984, URL: <https://cds.cern.ch/record/102083>.
- 2115 [88] ATLAS Collaboration,
2116 *The ATLAS Experiment at the CERN Large Hadron Collider*,
2117 JINST **3** (2008) S08003.
- 2118 [89] ATLAS Collaboration, *2015 start-up trigger menu and initial performance
2119 assessment of the ATLAS trigger using Run-2 data*,
2120 ATL-DAQ-PUB-2016-001, 2016,
2121 URL: <https://cds.cern.ch/record/2136007/>.
- 2122 [90] ATLAS Collaboration, *Performance of the ATLAS Inner Detector Track and
2123 Vertex Reconstruction in High Pile-Up LHC Environment*,
2124 ATLAS-CONF-2012-042, 2012,
2125 URL: <https://cds.cern.ch/record/1435196>.
- 2126 [91] ATLAS Collaboration, *Early Inner Detector Tracking Performance in the
2127 2015 Data at $\sqrt{s} = 13$ TeV*, ATL-PHYS-PUB-2015-051, 2015,
2128 URL: <https://cds.cern.ch/record/2110140>.
- 2129 [92] K Hamano, A Morley, and A Salzburger,
2130 “Track Reconstruction Performance and Efficiency Estimation using different
2131 ID geometry samples,” tech. rep. ATL-COM-PHYS-2012-1541,
2132 plots for a poster at HCP: CERN, Oct. 2012,
2133 URL: <https://cds.cern.ch/record/1489674>.
- 2134 [93] ATLAS Collaboration,
2135 *Electron reconstruction and identification efficiency measurements with the
2136 ATLAS detector using the 2011 LHC proton–proton collision data*,
2137 Eur. Phys. J. C **74** (2014) p. 2941, arXiv: [1404.2240](https://arxiv.org/abs/1404.2240) [hep-ex].
- 2138 [94] ATLAS Collaboration, *Topological cell clustering in the ATLAS calorimeters
2139 and its performance in LHC Run 1* (2016), arXiv: [1603.02934](https://arxiv.org/abs/1603.02934) [hep-ex].

- 2140 [95] ATLAS Collaboration, *Jet energy resolution in proton–proton collisions at*
 2141 $\sqrt{s} = 7 \text{ TeV}$ *recorded in 2010 with the ATLAS detector,*
 2142 *Eur. Phys. J. C* **73** (2013) p. 2306, arXiv: [1210.6210](https://arxiv.org/abs/1210.6210) [hep-ex].
- 2143 [96] M. Aaboud et al., *Measurement of the photon identification efficiencies with*
 2144 *the ATLAS detector using LHC Run-1 data* (2016),
 2145 arXiv: [1606.01813](https://arxiv.org/abs/1606.01813) [hep-ex].
- 2146 [97] ATLAS Collaboration, *Electron and photon energy calibration with the*
 2147 *ATLAS detector using LHC Run 1 data*, *Eur. Phys. J. C* **74** (2014) p. 3071,
 2148 arXiv: [1407.5063](https://arxiv.org/abs/1407.5063) [hep-ex].
- 2149 [98] “Electron and photon energy calibration with the ATLAS detector using
 2150 data collected in 2015 at $\sqrt{s} = 13 \text{ TeV}$,”
 2151 tech. rep. ATL-PHYS-PUB-2016-015, CERN, Aug. 2016,
 2152 URL: <https://cds.cern.ch/record/2203514>.
- 2153 [99] ATLAS Collaboration, *Muon reconstruction performance of the ATLAS*
 2154 *detector in proton–proton collision data at $\sqrt{s} = 13 \text{ TeV}$,*
 2155 *Eur. Phys. J. C* **76** (2016) p. 292, arXiv: [1603.05598](https://arxiv.org/abs/1603.05598) [hep-ex].
- 2156 [100] ATLAS Collaboration, *Jet energy measurement with the ATLAS detector in*
 2157 *proton–proton collisions at $\sqrt{s} = 7 \text{ TeV}$* , *Eur. Phys. J. C* **73** (2013) p. 2304,
 2158 arXiv: [1112.6426](https://arxiv.org/abs/1112.6426) [hep-ex].
- 2159 [101] ATLAS Collaboration,
 2160 *Jet energy measurement and its systematic uncertainty in proton–proton*
 2161 *collisions at $\sqrt{s} = 7 \text{ TeV}$ with the ATLAS detector,*
 2162 *Eur. Phys. J. C* **75** (2015) p. 17, arXiv: [1406.0076](https://arxiv.org/abs/1406.0076) [hep-ex].
- 2163 [102] S. D. Ellis and D. E. Soper,
 2164 *Successive combination jet algorithm for hadron collisions*,
 2165 *Phys. Rev. D* **48** (1993) p. 3160, arXiv: [hep-ph/9305266](https://arxiv.org/abs/hep-ph/9305266) [hep-ph].
- 2166 [103] M. Cacciari and G. P. Salam, *Dispelling the N^3 myth for the k_t jet-finder*,
 2167 *Phys. Lett. B* **641** (2006) p. 57, arXiv: [hep-ph/0512210](https://arxiv.org/abs/hep-ph/0512210) [hep-ph].
- 2168 [104] M. Cacciari, G. P. Salam, and G. Soyez,
 2169 *The Anti- $k(t)$ jet clustering algorithm*, *JHEP* **04** (2008) p. 063,
 2170 arXiv: [0802.1189](https://arxiv.org/abs/0802.1189) [hep-ph].
- 2171 [105] *Particle-Flow Event Reconstruction in CMS and Performance for Jets, Taus,*
 2172 *and MET* (2009).

- 2173 [106] ATLAS Collaboration,
 2174 *Tagging and suppression of pileup jets with the ATLAS detector*,
 2175 ATLAS-CONF-2014-018, 2014,
 2176 URL: <https://cds.cern.ch/record/1700870>.
- 2177 [107] M. Cacciari, G. P. Salam, and G. Soyez, *The Catchment Area of Jets*,
 2178 JHEP **04** (2008) p. 005, arXiv: [0802.1188 \[hep-ph\]](https://arxiv.org/abs/0802.1188).
- 2179 [108] “Optimisation of the ATLAS b -tagging performance for the 2016 LHC Run,”
 2180 tech. rep. ATL-PHYS-PUB-2016-012, CERN, June 2016,
 2181 URL: <https://cds.cern.ch/record/2160731>.
- 2182 [109] G. Aad et al., *Performance of algorithms that reconstruct missing transverse*
 2183 *momentum in $\sqrt{s} = 8$ TeV proton-proton collisions in the ATLAS detector*
 2184 (2016), arXiv: [1609.09324 \[hep-ex\]](https://arxiv.org/abs/1609.09324).
- 2185 [110] ATLAS Collaboration,
 2186 *Prospects for Supersymmetry discovery based on inclusive searches at a*
 2187 *7 TeV centre-of-mass energy with the ATLAS detector*,
 2188 ATL-PHYS-PUB-2010-010, 2010,
 2189 URL: <https://cds.cern.ch/record/1278474>.
- 2190 [111] ATLAS Collaboration,
 2191 *Expected sensitivity studies for gluino and squark searches using the early*
 2192 *LHC 13 TeV Run-2 dataset with the ATLAS experiment*,
 2193 ATL-PHYS-PUB-2015-005, 2015, URL:
<https://atlas.web.cern.ch/Atlas/GROUPS/PHYSICS/PUBNOTES/ATL-PHYS-PUB-2015-005>.
- 2196 [112] ATLAS Collaboration, *Expected performance of missing transverse*
 2197 *momentum reconstruction for the ATLAS detector at $\sqrt{s} = 13$ TeV*,
 2198 ATL-PHYS-PUB-2015-023, 2015,
 2199 URL: <https://cds.cern.ch/record/2037700>.
- 2200 [113] ATLAS Collaboration,
 2201 *Performance of missing transverse momentum reconstruction with the*
 2202 *ATLAS detector in the first proton–proton collisions at $\sqrt{s} = 13$ TeV*,
 2203 ATL-PHYS-PUB-2015-027, 2015,
 2204 URL: <https://cds.cern.ch/record/2037904>.
- 2205 [114] P. Jackson, C. Rogan, and M. Santoni, *Sparticles in Motion - getting to the*
 2206 *line in compressed scenarios with the Recursive Jigsaw Reconstruction*
 2207 (2016), arXiv: [1607.08307 \[hep-ph\]](https://arxiv.org/abs/1607.08307).

- 2208 [115] ATLAS Collaboration,
2209 *Further searches for squarks and gluinos in final states with jets and missing*
2210 *transverse momentum at $\sqrt{s} = 13$ TeV with the ATLAS detector,*
2211 ATLAS-CONF-2016-078, 2016,
2212 URL: <https://cds.cern.ch/record/2206252>.
- 2213 [116] C. Rogan, *Kinematical variables towards new dynamics at the LHC* (2010),
2214 arXiv: [1006.2727 \[hep-ph\]](https://arxiv.org/abs/1006.2727).
- 2215 [117] M. R. Buckley et al.,
2216 *Super-Razor and Searches for Sleptons and Charginos at the LHC*,
2217 Phys. Rev. D **89** (2014) p. 055020, arXiv: [1310.4827 \[hep-ph\]](https://arxiv.org/abs/1310.4827).
- 2218 [118] CMS Collaboration, *Search for supersymmetry using razor variables in*
2219 *events with b-tagged jets in pp collisions at $\sqrt{s} = 8$ TeV,*
2220 Phys. Rev. D **91** (2015) p. 052018, arXiv: [1502.00300 \[hep-ex\]](https://arxiv.org/abs/1502.00300).
- 2221 [119] Chris Rogan, “RestFrames,” URL: [{http://restframes.com}](http://restframes.com).
- 2222 [120] M. Baak et al., *HistFitter software framework for statistical data analysis*,
2223 Eur. Phys. J. C **75** (2015) p. 153, arXiv: [1410.1280 \[hep-ex\]](https://arxiv.org/abs/1410.1280).
- 2224 [121] ATLAS Collaboration, *Monte Carlo Generators for the Production of a W*
2225 *or Z/ γ^* Boson in Association with Jets at ATLAS in Run 2*,
2226 ATL-PHYS-PUB-2016-003, 2016,
2227 URL: <https://cds.cern.ch/record/2120133>.
- 2228 [122] ATLAS Collaboration, *Simulation of top-quark production for the ATLAS*
2229 *experiment at $\sqrt{s} = 13$ TeV*, ATL-PHYS-PUB-2016-004, 2016,
2230 URL: <https://cds.cern.ch/record/2120417>.
- 2231 [123] ATLAS Collaboration, *Multi-boson simulation for 13 TeV ATLAS analyses*,
2232 ATL-PHYS-PUB-2016-002, 2016,
2233 URL: <https://cds.cern.ch/record/2119986>.
- 2234 [124] R. D. Cousins, J. T. Linnemann, and J. Tucker,
2235 *Evaluation of three methods for calculating statistical significance when*
2236 *incorporating a systematic uncertainty into a test of the background-only*
2237 *hypothesis for a Poisson process*, Nucl. Instrum. Meth. A **595** (2008) p. 480.

2238

The Standard Model

2239 In this appendix, we provide a brief overview of the basic ingredients involved in
2240 construction of the Standard Model Lagrangian : quantum field theory, symmetries,
2241 and symmetry breaking.

2242 Quantum Field Theory

2243

2244 In this section, we provide a brief overview of the necessary concepts from
2245 Quantum Field Theory (QFT).

2246 In modern physics, the laws of nature are described by the “action” S , with the
2247 imposition of the principle of minimum action. The action is the integral over the cite
2248 spacetime coordinates of the “Lagrangian density” \mathcal{L} , or Lagrangian for short. The
2249 Lagrangian is a function of “fields”; general fields will be called $\phi(x^\mu)$, where the
2250 indices μ run over the space-time coordinates. We can then write the action S as

$$S = \int d^4x \mathcal{L}[\phi_i(x^\mu), \partial_\mu \phi_i(x^\mu)] \quad (9.1)$$

2251 where we have an additional summation over i (of the different fields). Generally,
2252 we impose the following constraints on the Lagrangian :

- 2253 1. Translational invariance - The Lagrangian is only a function of the fields ϕ and
2254 their derivatives $\partial_\mu \phi$
- 2255 2. Locality - The Lagrangian is only a function of one point x_μ in spacetime.

cite Yuval's
lectures
and notes
somehow

cite

- 2256 3. Reality condition - The Lagrangian is real to conserve probability.
- 2257 4. Lorentz invariance - The Lagrangian is invariant under the Poincarégroup of
2258 spacetime.
- 2259 5. Analyticity - The Lagrangian is an analytical function of the fields; this is to
2260 allow the use of perturbation theory.
- 2261 6. Invariance and Naturalness - The Lagrangian is invariant under some internal
2262 symmetry groups; in fact, the Lagrangian will have *all* terms allowed by the
2263 imposed symmetry groups.
2264 7. Renormalizability - The Lagrangian will be renormalizable - in practice, this
2265 means there will not be terms with more than power 4 in the fields.

2266 The key item from the point of view of this thesis is that of “Invariance and
2267 Natural”. We impose a set of “symmetries” and then our Lagrangian is the most
2268 general which is allowed by those symmetries.

2269 **Symmetries**

2270 Symmetries can be seen as the fundamental guiding concept of modern physics.
2271 Symmetries are described by “groups”. To illustrate the importance of symmetries
2272 and their mathematical description, groups, we start here with two of the simplest
2273 and most useful examples : \mathbb{Z}_2 and $U(1)$.

2274 \mathbb{Z}_2 symmetry

2275 \mathbb{Z}_2 symmetry is the simplest example of a “discrete” symmetry. Consider the most
2276 general Lagrangian of a single real scalar field $\phi(x_\mu)$

$$\mathcal{L}_\phi = \frac{1}{2}\partial_\mu\phi\partial^\mu\phi - \frac{m^2}{2}\phi^2 - \frac{\mu}{2\sqrt{2}}\phi^3 - \lambda\phi^4 \quad (9.2)$$

Now we *impose* the symmetry

$$\mathcal{L}(\phi) = \mathcal{L}(-\phi) \quad (9.3)$$

2277 This has the effect of restricting the allowed terms of the Lagrangian. In particular,
 2278 we can see the term $\phi^3 \rightarrow -\phi^3$ under the symmetry transformation, and thus must
 2279 be disallowed by this symmetry. This means under the imposition of this particular
 2280 symmetry, our Lagrangian should be rewritten as

$$\mathcal{L}_\phi = \frac{1}{2}\partial_\mu\phi\partial^\mu\phi - \frac{m^2}{2}\phi^2 - \lambda\phi^4 \quad (9.4)$$

2281 The effect of this symmetry is that the total number of ϕ particles can only change
 2282 by even numbers, since the only interaction term $\lambda\phi^4$ is an even power of the field.
 2283 This symmetry is often imposed in supersymmetric theories, as we will see in Chapter
 2284 3.

2285 **$U(1)$ symmetry**

2286 $U(1)$ is the simplest example of a continuous (or *Lie*) group. Now consider a theory
 2287 with a single complex scalar field $\phi = \text{Re } \phi + i \text{Im } \phi$

$$\mathcal{L}_\phi = \delta_{i,j} \frac{1}{2}\partial_\mu\phi_i\partial^\mu\phi_j - \frac{m^2}{2}\phi_i\phi_j - \frac{\mu}{2\sqrt{2}}\phi_i\phi_j\phi_k\phi_l - \lambda\phi_i\phi_j\phi_k\phi_l \quad (9.5)$$

2288 where $i, j, k, l = \text{Re}, \text{Im}$. In this case, we impose the following $U(1)$ symmetry
 2289 : $\phi \rightarrow e^{i\theta}, \phi^* \rightarrow e^{-i\theta}$. We see immediately that this again disallows the third-order
 2290 terms, and we can write a theory of a complex scalar field with $U(1)$ symmetry as

$$\mathcal{L}_\phi = \partial_\mu\phi\partial^\mu\phi^* - \frac{m^2}{2}\phi\phi^* - \lambda(\phi\phi^*)^2 \quad (9.6)$$

2291 **Local symmetries**

2292 The two examples considered above are “global” symmetries in the sense that the
2293 symmetry transformation does not depend on the spacetime coordinate x_μ . We know
2294 look at local symmetries; in this case, for example with a local $U(1)$ symmetry, the
2295 transformation has the form $\phi(x_\mu) \rightarrow e^{i\theta(x_\mu)}\phi(x_\mu)$. These symmetries are also known
2296 as “gauge” symmetries; all symmetries of the Standard Model are gauge symmetries.

There are wide-ranging consequences to the imposition of local symmetries. To begin, we note that the derivative terms of the Lagrangian 9.2 are *not* invariant under a local symmetry transformation

$$\partial_\mu \phi(x_\mu) \rightarrow \partial_\mu(e^{i\theta(x_\mu)}\phi(x_\mu)) = (1 + i\theta(x_\mu))e^{i\theta(x_\mu)}\phi(x_\mu) \quad (9.7)$$

GET THIS
RIGHT

2297 This leads us to note that the kinetic terms of the Lagrangian are also not invariant
2298 under a gauge symmetry. This would lead to a model with no dynamics, which is
2300 clearly unsatisfactory.

2301 Let us take inspiration from the case of global symmetries. We need to define a
2302 so-called “covariant” derivative D^μ such that

$$D^\mu \phi \rightarrow e^{iq\theta(x^\mu)D^\mu}\phi \quad (9.8)$$

$$D^\mu \phi^* \rightarrow e^{-iq\theta(x^\mu)D^\mu}\phi^* \quad (9.9)$$

$$(9.10)$$

2303 Since ϕ and ϕ^* transforms with the opposite phase, this will lead the invariance
2304 of the Lagrangian under our local gauge transformation. This D^μ is of the following
2305 form

$$D^\mu = \partial_\mu - igqA^\mu \quad (9.11)$$

2306 where A^μ is a vector field we introduce with the transformation law

$$A^\mu \rightarrow A^\mu - \frac{1}{g} \partial_\mu \theta \quad (9.12)$$

2307 and g is the coupling constant associated to vector field. This vector field A^μ is
2308 also known as a “gauge” field.

2309 Since we need to add all allowed terms to the Lagrangian, we define

$$F^{\mu\nu} = A^\mu A^\nu - A^\nu A^\mu \quad (9.13)$$

2310 and then we must also add the kinetic term :

$$\mathcal{L}_{\text{gauge}} = -\frac{1}{4} F^{\mu\nu} F_{\mu\nu} \quad (9.14)$$

2311 The most general renormalizable Lagrangian with fermion and scalar fields can
2312 be written in the following form

$$\mathcal{L} = \mathcal{L}_{\text{kin}} + \mathcal{L}_\phi + \mathcal{L}_\psi + \mathcal{L}_{\text{Yukawa}} \quad (9.15)$$

2313 Symmetry breaking and the Higgs mechanism

2314 Here we view some examples of symmetry breaking. We investigate breaking of a
2315 global $U(1)$ symmetry and a local $U(1)$ symmetry. The SM will break the electroweak
2316 symmetry $SU(2)xU(1)$, and in Chapter 3 we will see how supersymmetry must also
2317 be broken.

2318 There are two ideas of symmetry breaking

2319 • Explicit symmetry breaking by a small parameter - in this case, we have a small
2320 parameter which breaks an “approximate” symmetry of our Lagrangian. An
2321 example would be the theory of the single scalar field 9.2, when $\mu \ll m^2$ and

$\mu \ll \lambda$. In this case, we can often ignore the small term when considering low-energy processes.

- Spontaneous symmetry breaking (SSB) - spontaneous symmetry breaking occurs when the Lagrangian is symmetric with respect to a given symmetry transformation, but the ground state of the theory is *not* symmetric with respect to that transformation. This can have some fascinating consequences, as we will see in the following examples

Symmetry breaking a

U(1) global symmetry breaking

Consider the theory of a complex scalar field under the $U(1)$ symmetry, or the transformation

$$\phi \rightarrow e^{i\theta} \phi \quad (9.16)$$

The Lagrangian for this theory is

$$\mathcal{L} = \partial^\mu \phi^\dagger \partial_\mu \phi + \frac{\mu^2}{2} \phi^\dagger \phi + \frac{\lambda}{4} (\phi^\dagger \phi)^2 \quad (9.17)$$

Let us write this theory in terms of two scalar fields, h and ξ : $\phi = (h + i\xi)/\sqrt{2}$.

The Lagrangian can then be written as

$$\mathcal{L} = \partial^\mu h \partial_\mu h + \partial^\mu \xi d\mu \xi - \frac{\mu^2}{2} (h^2 + \xi^2) - \frac{\lambda}{4} (h^2 + \xi^2)^2 \quad (9.18)$$

First, note that the theory is only stable when $\lambda > 0$. To understand the effect of SSB, we now enforce that $\mu^2 < 0$, and define $v^2 = -\mu^2/\lambda$. We can then write the scalar potential of this theory as :

$$V(\phi) = \lambda(\phi^\dagger \phi - v^2/2)^2 \quad (9.19)$$

Minimizing this equation with respect to ϕ , we can see that the “vacuum expectation value” of the theory is

$$2 < \phi^\dagger \phi > = < h^2 + \xi^2 > = v^2 \quad (9.20)$$

2331 We now reach the “breaking” point of this procedure. In the (h, ξ) plane, the
 2332 minima form a circle of radius v . We are free to choose any of these minima to expand
 2333 our Lagrangian around; the physics is not affected by this choice. For convenience,
 2334 choose $\langle h \rangle = v, \langle \xi^2 \rangle = 0$.

Now, let us define $h' = h - v, \xi' = \xi$ with VEVs $\langle h' \rangle = 0, \langle \xi' \rangle = 0$. We can
 then write our spontaneously broken Lagrangian in the form

$$\mathcal{L} = \frac{1}{2}\partial_\mu h'\partial^\mu h' + \frac{1}{2}\partial_\mu \xi'\partial^\mu \xi' - \lambda v^2 h'^2 - \lambda v h'(h'^2 + \xi'^2) - \lambda(h'^2 + \xi'^2)^2 \quad (9.21)$$